FRICTION STIR WELDING OF HIGH STRENGTH PRECIPITATION STRENGTHENED ALUMINUM ALLOYS

Harpreet Sidhar, B.Tech

Dissertation Prepared for the Degree of

DOCTOR OF PHILOSOPHY

UNIVERSITY OF NORTH TEXAS

August 2016

APPROVED:

Rajiv S. Mishra, Major Professor
Rajarshi Banerjee, Committee Member
Zhenhai Xia, Committee Member
Marcus Young, Committee Member
Sundeep Mukherjee, Committee Member
Andrey Vevodin, Chair of the Department of Materials Science and Engineering
Costas Tsatsoulis, Dean of the College of Engineering
Victor Prybutok, Vice Provost of the Toulouse Graduate School

Sidhar, Harpreet. *Friction Stir Welding of High Strength Precipitation Strengthened Aluminum Alloys*. Doctor of Philosophy (Materials Science and Engineering), August 2016, 140 pp., chapter references.

Precipitation strengthened 2XXX and 7XXX aluminum alloys are the key aluminum alloys used extensively in aerospace industry. Welding and joining is the critical step in manufacturing of integrated structures. Joining of precipitation strengthened aluminum alloys using conventional fusion welding techniques is difficult and rather undesirable in as it produces dendritic microstructure and porosities which can undermine the structural integrity of weldments. Friction stir welding, invented in 1991, is a solid state joining technique inherently benefitted to reduces the possibility of common defects associated with fusion based welding techniques.

Weldability of various 2XXX and 7XXX aluminum alloys via friction stir welding was investigated. Microstructural and mechanical property evolution during welding and after post weld heat treatment was studied using experimental techniques such as transmission electron microscopy, differential scanning calorimetry, hardness testing, and tensile testing. Various factors such as peak welding temperature, cooling rate, external cooling methods (thermal management) which affects the strength of the weldment were studied. Post weld heat treatment of AL-Mg-Li alloy produced joint as strong as the parent material. Modified post weld heat treatment in case of welding of Al-Zn-Mg alloy also resulted in near 100% joint efficiency whereas the maximum weld strength achieved in case of welds of Al-Cu-Li alloys was around 80-85% of parent material strength. Low dislocation density and high nucleation barrier for the precipitates was observed to be responsible for relatively low strength recovery in Al-Cu-Li alloys as compared to Al-Mg-Li and Al-Zn-Mg alloys.

ACKNOWLEDGMENTS

First of all, I would like to express my gratitude to my advisor, Dr. Rajiv Mishra, for his continuous supervision, encouragement, and support during the duration of my doctoral degree at UNT. My PhD work is the result of many exciting and inspiring discussions with him. I also want to thank Dr. Mishra for providing me with many opportunities to work on various other projects apart from my PhD research, which helped me in development of my scientific and interpersonal skills. I also gratefully acknowledge the financial support of the Center for Friction Stir Processing at UNT, which is a National Science Foundation I/UCRC site.

I also acknowledge Professors: R Banerjee, M Young, Z Xia, and S Mukherjee for their advice and suggestions while going through my PhD research proposal and dissertation.

This dissertation could not have been completed without the support from my friends and colleagues. My friends, in and around the USA, and back home in India, supported and made me breeze through many hurdles. I thank you: Pooja, Adi, Ankit, Pankush, Gurpartap, Amit, Shami, Garima, Phalgun, Maggie, Shravan, Parul, Aniket, Ved, Tian, Nelson, Nilesh and those who I've missed! A special word of thank to Pooja, for her love, encouragement, and selfless support throughout my grad studies.

Most of all, I am deeply grateful to my family: papa, mummy, sisters Kavita and Jyoti for their unequivocal support throughout my studies. They have made many sacrifices for me and I can't overstate my gratitude to them.

TABLE OF CONTENTS

CHAPTER 1

INTRODUCTION

Rising demand for fuel economy, reduction in carbon footprint, and improved structural efficiency are pushing factors for light weighting in automotive and aerospace industries. Aluminum is the most abundant metal on earth [1], and is the second lightest metal after magnesium, commercially used in alloy form. Combination of various mechanical, physical, thermal, corrosion properties and economics makes aluminum alloys a key candidate in aerospace applications [2]. Since the early days of commercial aircraft manufacturing, aluminum has been the main material for primary aircraft structures [3]. Although, recently, polymer matrix composite materials are showing promising results and are being used significantly in some cases (the Boeing 787 Dreamliner) [4], aluminum alloys are still considered as primary material for airframe construction and contributes 60% of structural weight in case of Airbus A380 passenger aircraft [4].

Aluminum alloys are produced in both cast and wrought forms. Wrought aluminum alloys are classified based on the main alloying element. Table 1.1 shows the standard four-digit designation developed by the Aluminum Association for wrought aluminum alloys [5]. This designation is followed by majority of the countries around the world and is referred as International Alloy Designation System (IADS). Wrought aluminum alloys can be further classified into heat treatable and non-heat treatable alloys. The 1XXX, 3XXX, and 5XXX alloys are non-heat treatable and strengthened by work hardening [2]. The 2XXX, 6XXX, 7XXX and some of 8XXX belong to the heat treatable (age hardenable or precipitation strengthened) aluminum alloys category [2]. These alloys possess highest specific strength in aluminum alloys. Most of the heat treatable alloys are highly alloyed with other elements to achieve high strength.

9XXX alloy series is still unused for new type of aluminum alloys in future.

Table 1.1. Standard designation for wrought aluminum alloys.

Standard designation	Main alloying element
1XXX	None (> 99% Aluminum)
2XXX	Copper
3XXX	Manganese
4XXX	Silicon
5XXX	Magnesium
6XXX	Magnesium and Silicon
7XXX	Zinc
8XXX	Others
9XXX	Unused

1.1 Precipitation Strengthened Aluminum Alloys

The 2XXX, 6XXX, 7XXX and some of 8XXX alloys form the class of precipitation strengthened aluminum alloys. 2XXX and 7XXX based aluminum alloys have high yield strength in the range of 400-700 MPa in peak aged condition and thus are extensively used in aerospace industry. Precipitation strengthened alloys derives their strength by the formation of dispersion of fine particles which act as obstacles to moving dislocations during deformation [6,7]. It is the most widely used method to improve strength in aluminum alloys. The basic criteria for an alloy to be classified as precipitation strengthened alloy is a decrease in solid solubility of alloying elements with decrease in temperature. It can be explained with the classical example of precipitation in Al-Cu system as shown in Figure 1.1. The thermal treatment

required in this process starts with solution heat treatment by soaking the alloy at sufficiently high temperature for long enough to form solid solution (step 1 in Figure 1.1). It is followed by rapid quenching to room temperature to form supersaturated solid solution (step 2 in Figure 1.1). Precipitation of secondary phases occurs at room temperature (natural aging) or elevated temperature (artificial aging, step 3 in Figure 1.1) due the decrease in solid solubility of alloying elements at lower temperatures. Artificial aging can be a single or multi step thermal treatment depending upon alloy chemistry and targeted property.

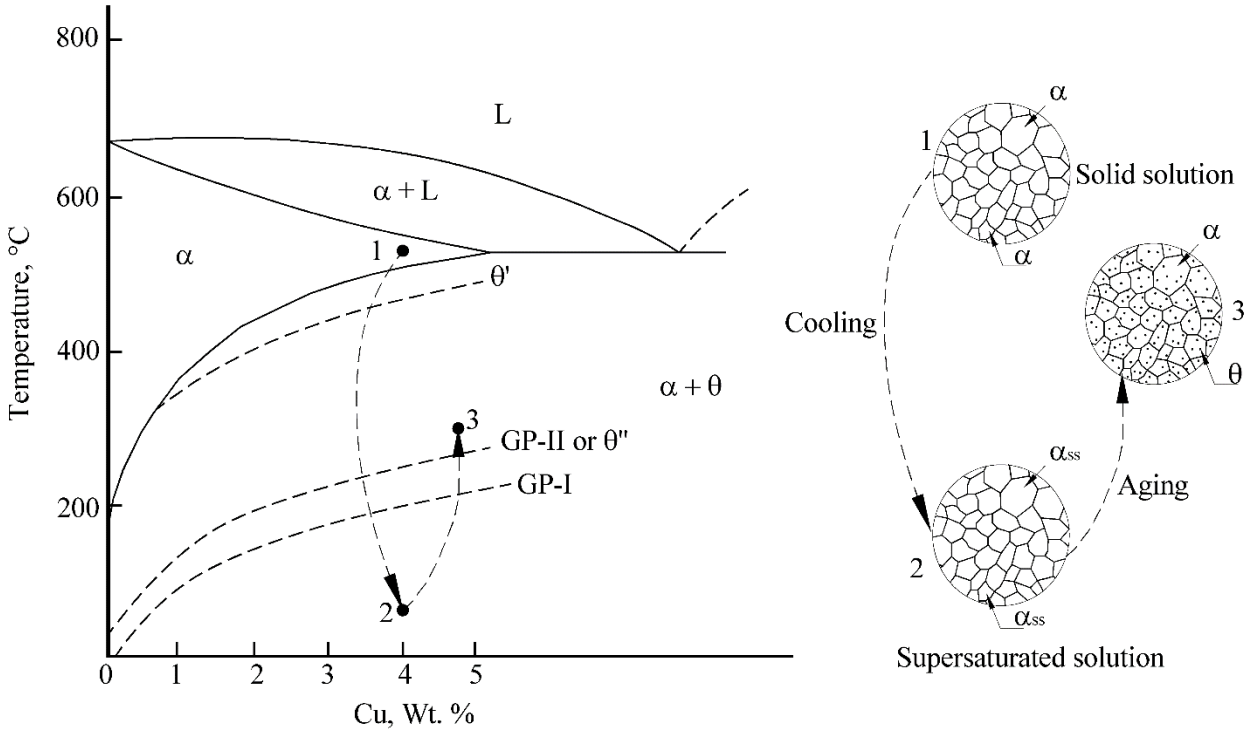

Figure 1.1 Aluminum rich binary phase diagram of Al-Cu system with a schematic to illustrate the steps involved in aging treatment of precipitation strengthened aluminum alloys [8].

Industrially, precipitation strengthened aluminum alloys are subjected to various thermo-mechanical processes to achieve application specific properties. For example, after quenching to room temperature, alloy is cold worked to introduce dislocation structures to enhance the

precipitation of second phases to improve the maximum strength. These processes result in different microstructural states of the alloy and are known as tempers. The standard temper designation for precipitation strengthened aluminum alloys are listed in Table 1.2.

Table 1.2. Standard temper designation applicable to precipitation strengthened aluminum alloys [9].

F	As fabricated
O	Annealed: lowest strength, highest ductility temper
W	Solution heat treated: Unstable, usually followed by natural aging
T1	Cooled from an elevated temperature processing and naturally aged to a substantially stable condition
T2	Cooled from an elevated temperature processing, cold worked, and naturally aged to a substantially stable condition
T3	Solution heat treated, cold worked, and naturally aged to a substantially stable condition
T4	Solution heat treated and naturally aged to a substantially stable condition
T5	Cooled from an elevated temperature processing and artificially aged
T6	Solution heat treated and artificially aged usually to the maximum strength
T7	Solution heat treated and overaged or stabilized
T8	Solution heat treated, cold worked, and artificially aged
T9	Solution heat treated, artificially aged, and cold worked
T10	Cooled from an elevated temperature processing, cold worked, and artificially aged

The 2XXX and 7XXX alloys have been dominating aluminum alloys in aerospace since the inception of commercial, space, and military aviation industries. Figure 1.2 shows the chronological evolution of major aluminum alloys developed in different product form for applications spanning through various platforms in aerospace industry. It is clear from Figure 1.2 that there is an increased use of lithium bearing aluminum alloys (Al-Li alloys) within 2XXX alloys apart from 7XXX alloys. 7XXX alloys are used for their ultra-high strength and excellent corrosion resistance behavior. Whereas, Al-Li alloys have gained interest due to the lower density and high strength combination.

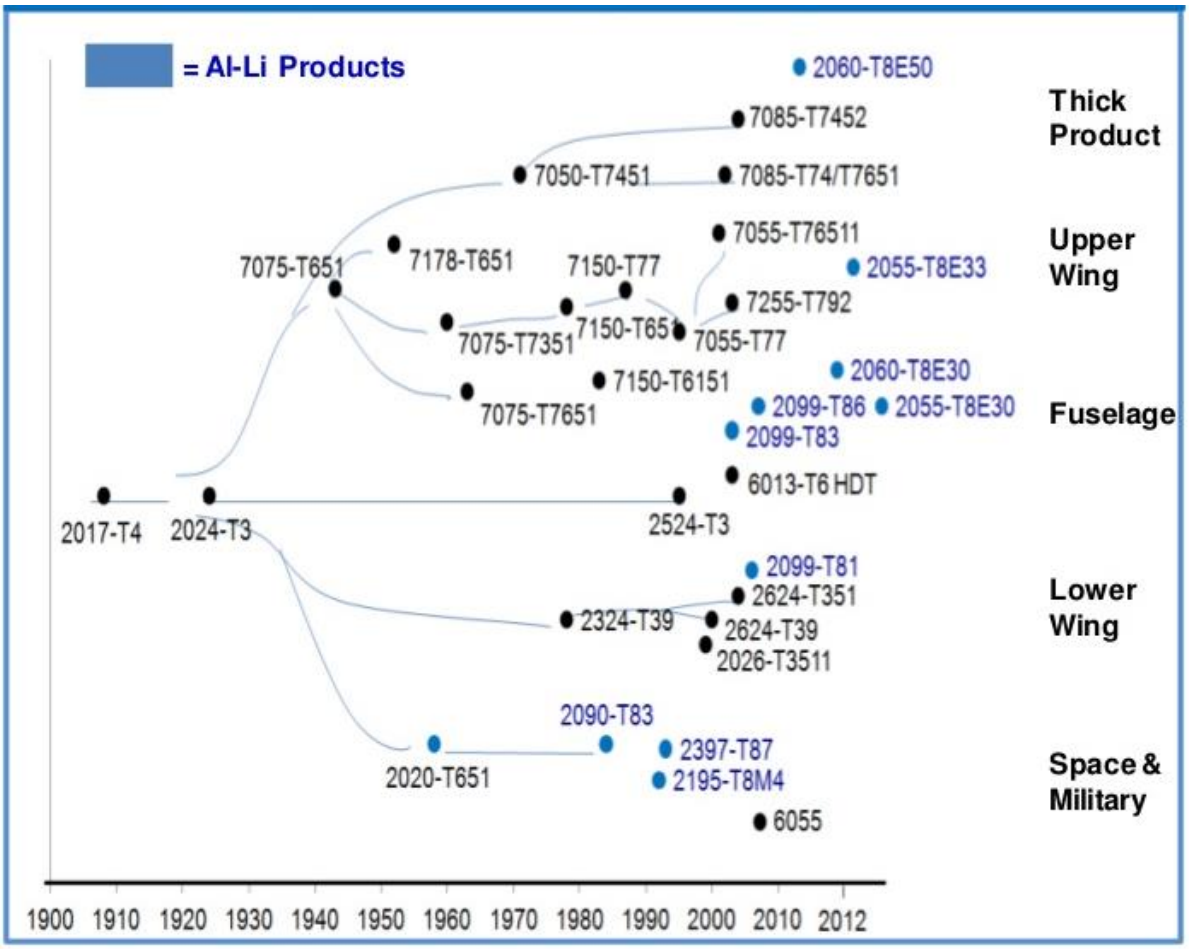

Figure 1.2. Chronology of development of various aerospace aluminum alloys at ALCOA for application in various sectors of aerospace industry [10].

1.2 Aluminum-Lithium Alloys

Al-Li alloys have gained popularity from the fact that addition of each 1weight % lithium, the lightest metallic element, enhances the elastic modulus by 6% and reduces the density of resultant binary aluminum alloy by 3% [11,12]. Except beryllium, which is toxic, lithium is the only metal that decreases the density and improves the elastic modulus of aluminum [12] (Figure 1.3). Lower density and higher modulus provides high stiffness (elastic modulus/density) and high specific strength (strength/density) which enables large weight savings in airplane structures and improves the fuel efficiency. Also, modern (third generation) Al-Li alloys possess excellent mechanical properties (high tensile strength, improved high cycle fatigue, and fatigue crack growth resistance) comparable to incumbent aerospace 7XXX and 2XXX alloys [13]. First Al-Li alloy X2020 was developed and used in 1957 in wing and tail structure of the US Navy RA5C aircraft but was later retracted due to toughness, ductility, and production issues [13]. It began the era and development of Al-Li alloys around the globe. It was followed by development and use of much lighter and moderate strength 1420 Al-Mg-Li based alloys in USSR in 1960s [14]. Fridlyander pioneered the development of Al-Li alloys in Soviet Union and used in Soviet aircraft structures [13-17]. In recent times, Al-Li have regained the interest and are being developed rapidly [4,13]. Replacement of 2219 (Al-Cu alloy) with 2195 (Al-Cu-Li alloy), which is 30% stronger and 5% less dense than 2219, in manufacturing of external fuel tank of space shuttle by NASA [18,19] shows the potential of the Al-Cu-Li-X family of alloys in aerospace and aviation sector. There are numerous other industrial applications of Al-Cu-Li-X alloys which includes Airbus A380 (2196 alloy), F16 aircraft (2297), Boeing 787 dreamliner (2099 and 2199), and Agusta Westland helicopter [4,13].

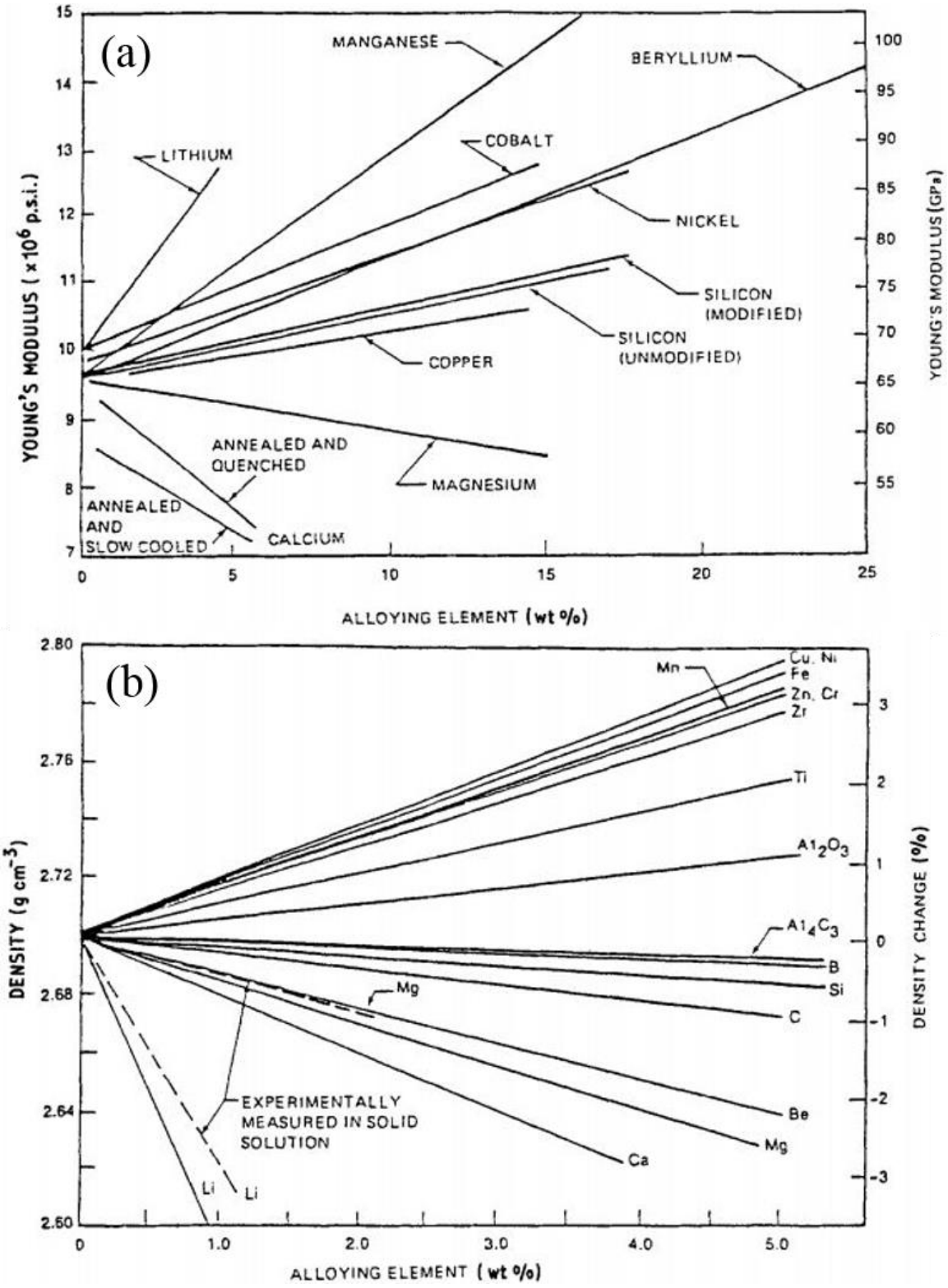

Figure 1.3(a) Change in Young's modulus and (b) change in density of aluminum with addition of various elements and compounds [12].

Al-Li alloys are precipitation strengthened alloys and hence a detailed insight into the precipitates involved in this system is of utmost importance. Precipitation sequence and the nature of the precipitates is governed by the alloying elements present, their absolute, and relative (ratios) concentrations. Other than lithium, copper and magnesium are most common alloying elements in Al-Li alloys. Other minor alloying elements such as Zr, Ag, Mn, Sc are also added to enhance certain targeted mechanical properties. Therefore, it is important to study the various alloy system under Al-Li family. The effect of various alloying elements and their relative (ratio) concentrations on the precipitation will also be discussed in later sections of this chapter.

1.2.1 Al-Li Binary System

Aluminum-lithium alloys are precipitation strengthened alloys, i.e. strength can be increased by solution heat treatment and then aging. Strength of these alloys is dependent on the type, size, volume fraction, and distribution of precipitation in the matrix and at grain boundaries. Lithium has high solubility in aluminum with a maximum of 16 at. % (4 wt.%) at 600°C as shown in Figure 1.4. Binary Al-Li alloys are strengthened by precipitation of metastable, coherent, and spheroidal Al_3Li (δ') precipitate [20-22]. δ' is a $L1_2$ ordered phase and has very small misfit strain and interfacial energy of ≈ 10 mJ/m^2 [20,23]. At equilibrium δ' transforms into stable δ (AlLi) and solid solution matrix of aluminum [12,20]. Hardening phase δ' may also be sheared by a moving dislocation which gives rise to slip planarity leading to poor ductility and hence considered as detrimental in Al-Li-X alloys [13].

On aging (below solvus of δ') after a solution treatment, δ' precipitates in spheroidal form and the sequence of precipitation for a binary Al-Li can be described as [20]:

$\alpha_{\text{supersaturated solid solution}} \rightarrow \alpha + \delta' \rightarrow \alpha + \delta$ (equilibrium)

δ is the equilibrium phase (AlLi) which precipitate out after dissolution of metastable δ' on overaging. Binary Al-Li based alloy has no practical application.

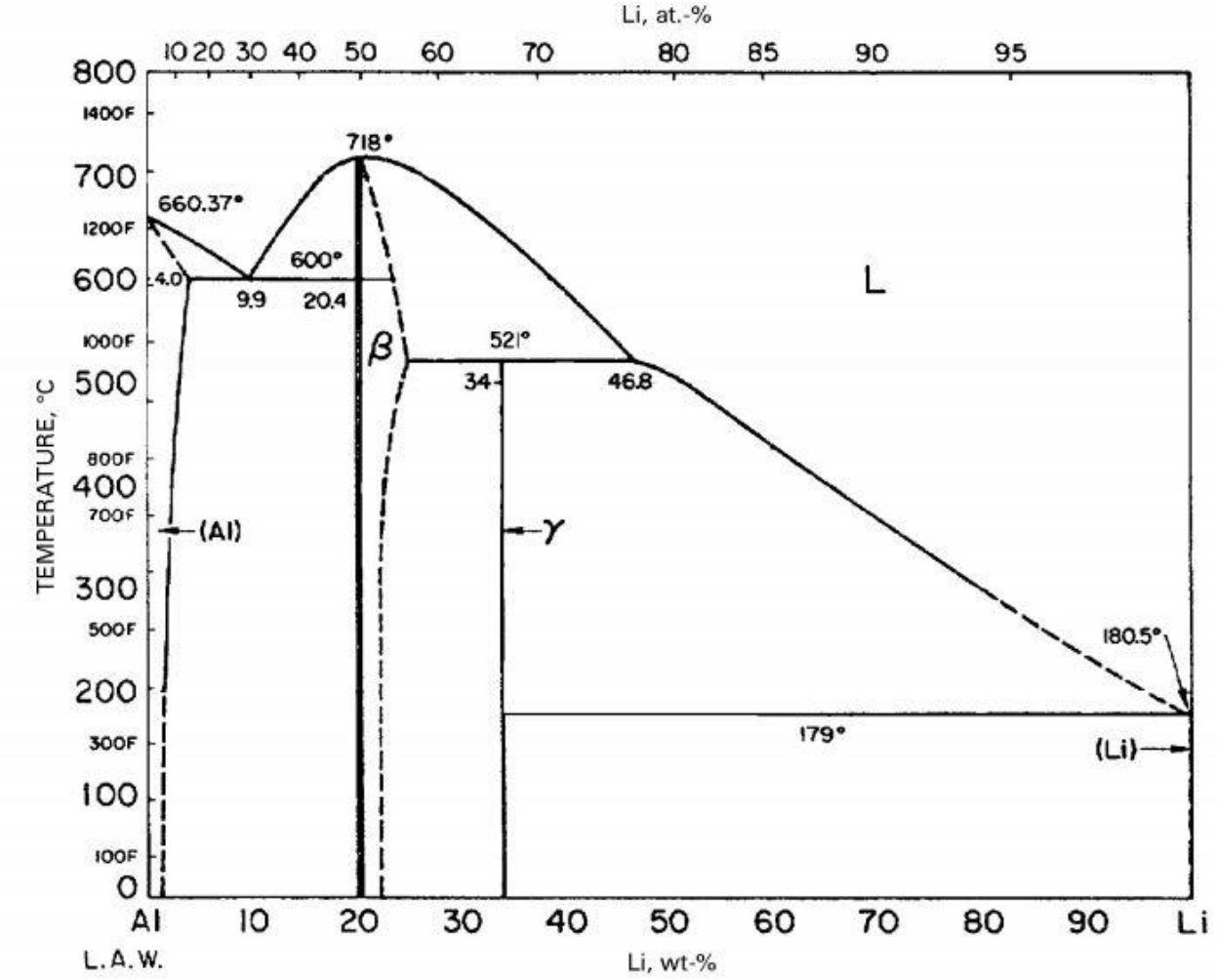

Figure 1.4. Binary phase diagram of Al-Li system [24].

1.2.2 Al-Mg-Li System

A number of Al-Mg-Li alloys were developed and studied in great detail by Russian researchers at Institute of Aviation Materials (VIAM), Moscow [14-17]. Variants of high Mg and Li content were developed such as 1420, 1421, and 1423. δ' is the main strengthening precipitate and T also sometimes referred as S_1 (cubic, Al_2LiMg) phase forms on overaging (stabilized) [13,14,17].

Noble and Thompson [20] suggested the precipitation sequence in Al-Mg-Li system and is as follows:

$\alpha_{\text{supersaturated solid solution}} \rightarrow \delta'\,(Al_3Li) \rightarrow \delta\,(AlLi)$ [for high Li/Mg ratio]

or

$\alpha_{\text{supersaturated solid solution}} \rightarrow \delta'\,(Al_3Li) \rightarrow T\,(Al_2MgLi)$ [for low Li/Mg ratio]

Mg has shown to reduce the solubility of Li in aluminum and therefore increases the Al_3Li precipitation [12].

1.2.3 Al-Cu-Li System

Al-Cu-Li alloys contains all the phase present in Al-Cu and Al-Li system i.e., θ', θ (Al_2Cu), and δ' (Al_3Li). T_1 (hexagonal, Al_2CuLi) is also observed and is the main strengthening precipitate along with θ and δ' in Al-Cu-Li system. T_1 forms as thin and long plate type structures on the {111} of matrix planes [25-28].

Cu:Li ratio has a huge impact on the type and volume fraction of precipitates in Al-Cu-Li alloys. Jo and Hirano [29] studied the effect of Cu:Li ratio on the precipitation in Al-Cu-Li alloy and their findings are as follows:

- For high Cu:Li (>4), $\alpha_{SS} \rightarrow$ GP zones $\rightarrow \theta'' \rightarrow \theta'$
- For Cu:Li = 2.5-4.0, $\alpha_{SS} \rightarrow$ GP zones $\rightarrow$ GP zones + $\delta' \rightarrow \delta' + \theta'' + \theta' \rightarrow \delta' + T_1$
- For Cu:Li = 1-2.5, $\alpha_{SS} \rightarrow$ GP zones + $\delta' \rightarrow \delta' + \theta' \rightarrow \delta' + T_1 \rightarrow T_1$
- For Cu:Li <1, $\alpha_{SS} \rightarrow \delta' + T_1 \rightarrow T_1$

Decreus et al. [30] also carried out similar study on 2198 (Cu:Li= 3.36) and 2196 (Cu:Li=1.65), though both the alloys are modern Al-Li alloys, and found results in accordance with Jo and Hirano [29]. 2198 was observed to show Cu clusters during natural aging whereas 2196 shows δ' precipitation. Cu also lowers the solubility of Li in aluminum and hence promotes

greater precipitation of Li containing precipitates.

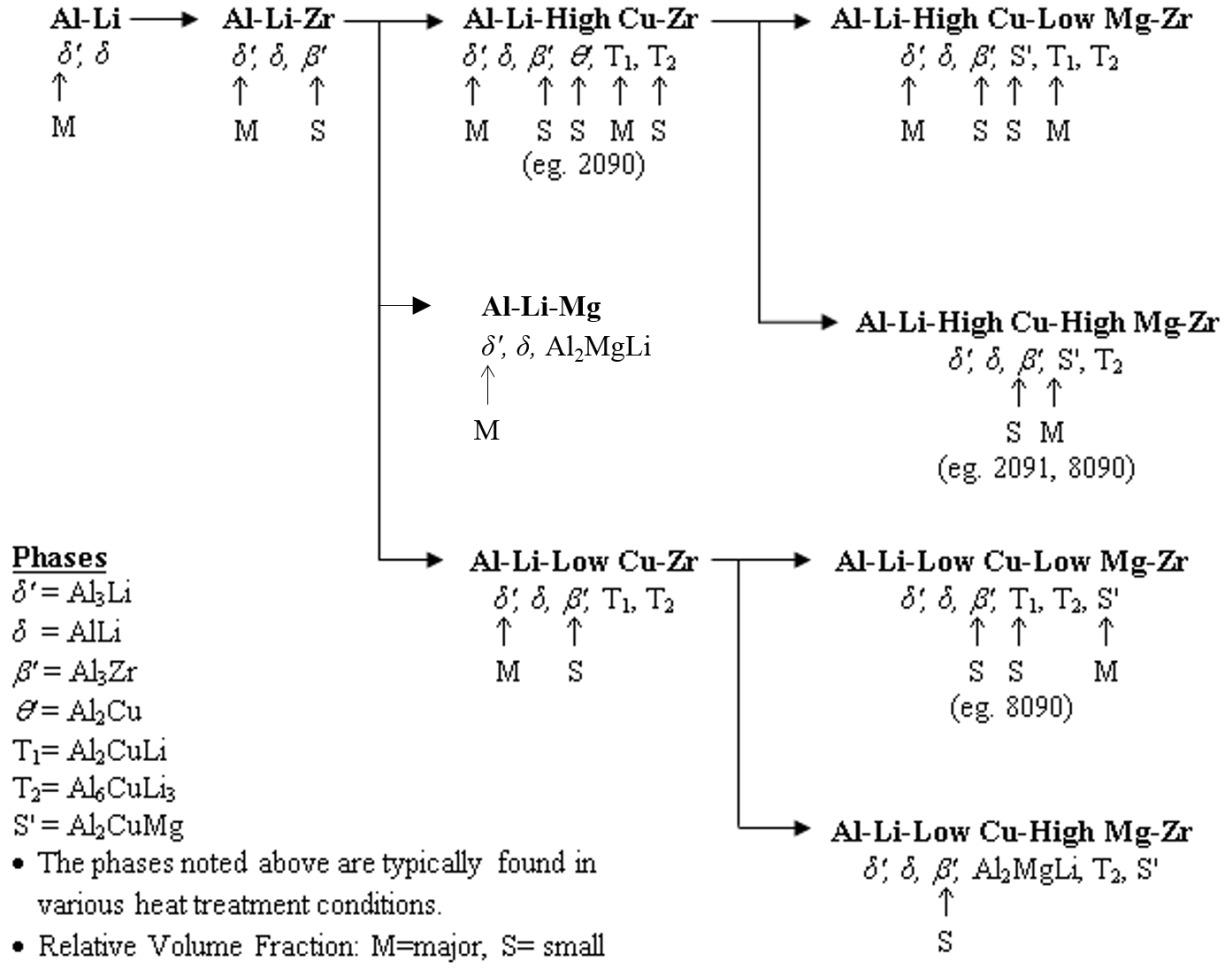

Figure 1.5. Flowchart showing possible phase in various binary, ternary, and quaternary Al-Li alloys [31].

1.2.4 Al-Cu-Mg-Li-X System

Most of the industrially utilized and latest third generation Al-Li alloys around the globe belongs to this category. In many of these alloys, small amount of Ag (usually 0.25 wt.%) is added to improve strength. Alloy composition of some of the third generation Al-Li alloys are listed in Table 1.4. Addition of minor alloying elements along with Li and Mg introduces improved strengthening in these alloys as compared to Al-Cu-Li alloys. Ag is known to stimulate

the precipitation of T_1 phase [32]. Ag accommodates the misfit energy between precipitate and aluminum matrix by segregating on matrix-precipitate interface [32]. Mg added alone to the ternary Al-Cu-Li alloy promotes GP zone formation and precipitation of early θ' and T_1 in later stages of aging treatment [32]. Effect of individual element will be discussed in greater detail in the next sub-section.

Table 1.3. Structural and compositional details of phases observed in Al-Li alloys [12,13].

Phase	Composition	Structure	Lattice parameters (nm)
δ'	Al_3Li	Cubic ($L1_2$)	a = 0.401
δ	AlLi	Cubic (NaCl)	a = 0.638
θ'	Al_2Cu	Tetragonal	a = 0.404, c = 0.58
θ	Al_2Cu	Tetragonal	a = 0.607, c = 0.487
T_1	Al_2CuLi	Hexagonal	a = 0.497, c = 0.935
T_2	Al_6CuLi_3	Cubic	a = 1.3914
T_B	$Al_{15}Cu_8Li_2$	Cubic (CaF_2)	a = 0.583
β	Al_3Zr	Cubic ($L1_2$)	a = 0.405
S'	Al_2CuMg	Orthorhombic	a = 0.401, b = 0.925, c = 0.715
Ω	Al_2Cu	Orthorhombic	a = 0.496, b = 0.859, c = 0.848
T or S	Al_2MgLi	Cubic	-

1.2.5 Role of Various Alloying Elements

As the Al-Li alloys gained attention and were developed for various aerospace applications, addition of various alloying elements were studied to establish the effect on mechanical properties. Different alloying element can serve different purposes such as

dispersoids, precipitates, nucleation agent for precipitates, etc. In this section, role of various major and minor alloying elements is discussed.

1.2.5.1 Role of Mg Addition

Huang and Zheng [32] studied the independent and combined roles of traces of Mg and Ag addition to Al-Cu-Li-Zr-Ti alloy. Independently Mg reduces the solubility of Li in aluminum. It also promotes GP zone formation. Mg also promotes the highly dense distribution of T_1 phase. Mg is believed to reduce the misfit energy between the precipitate and matrix thus promoting nucleation.

1.2.5.2 Role of Ag Addition

Contrastingly, Ag when added without Mg retards GP zone formation. Ag is also observed to stimulate the T_1 precipitation and increases the growth rates of T_1 and θ'. Ag also accommodates the lattice strain energy between precipitate and matrix by occupying sites at matrix-precipitate interface. Combined role of Ag and Mg promotes nucleation and precipitation of T_1 and thus increases the strength of the alloy (Figure 1.6). Precipitation of θ' is weakened due to the strong interaction of Mg with silver.

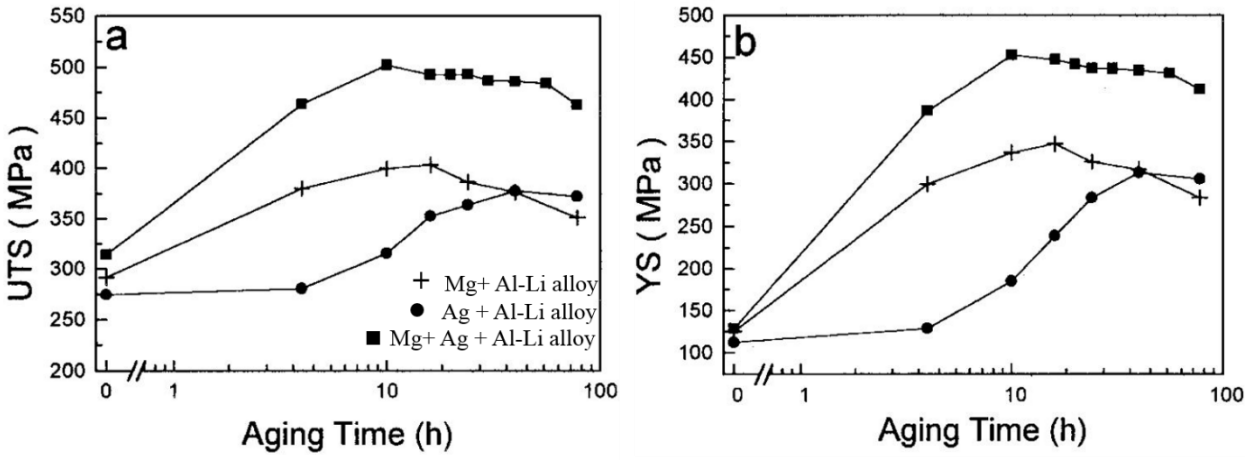

Figure 1.6. Effect of Ag and Mg addition on strength of an Al-Li alloy [32].

1.2.5.3 Role of Zr and Cr Addition

Zr or Cr or Mn addition to Al-Li alloys leads to the formation of dispersoids which restricts the grain growth by inhibiting the grain boundary movement during recrystallization [33]. Zr based dispersoids are very effective in pinning grain boundaries during high temperature processing of Al-Li alloys [34]. Dispersoids like Al_3Zr also acts as the heterogeneous nucleation sites for precipitation of Al_3Li phase during aging by reducing surface energy associated with Al_3Li formation [35-37]. Al_3Zr dispersoid has a cubic ($L1_2$) structure [34,36,37]. Ordered Al_3Zr is known to be stable up to 600°C due to low solubility of zirconium in aluminum [38].

1.2.6 Effect of Pre-Deformation

The density (distribution) and size of strengthening precipitates can significantly affect the strength of alloy. Aging practices such as soaking time and temperature controls the size and density of precipitates. However, in some case, plastic deformation prior to aging can also influence the precipitation kinetics. Almost all the 2XXX alloys are known to benefit from pre-deformation as shown in Figure 1.7 for an Al-Li alloy. Dislocations reduce the coherency strain between precipitate and matrix and acts as favorable nucleation sites.

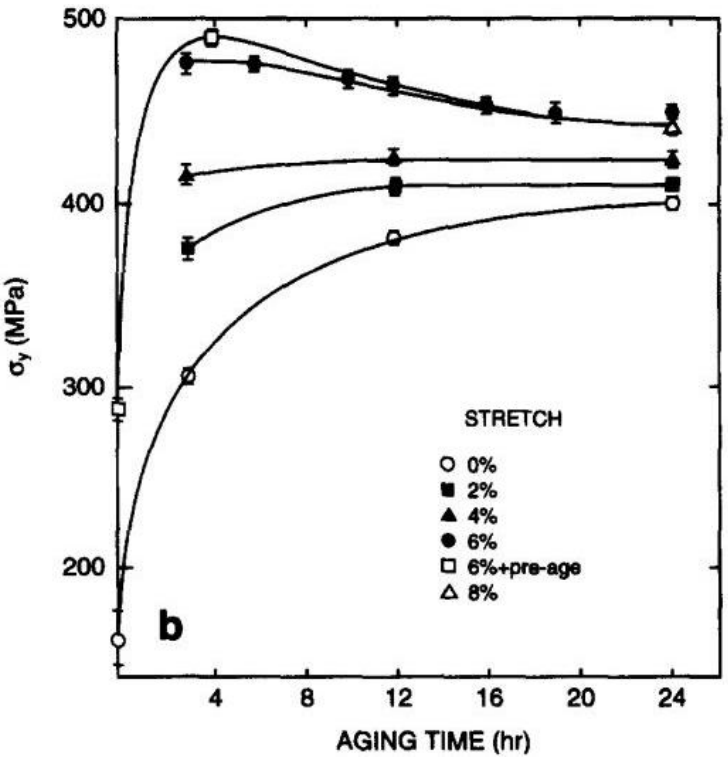

Figure 1.7. Effect of plastic deformation on an Al-Cu-Li alloy [39].

Table 1.4. Chemical composition limits of a few third generation Al-Li alloys.

Alloy	Li	Cu	Mg	Zr	Ag	Zn	Mn
2195	0.8-1.2	3.7-4.3	0.25-0.8	0.08-0.16	0.25-0.6	0.25	0.25
2196	1.4-2.1	2.5-3.3	0.25-0.8	0.04-0.18	0.25-0.6	0.35	0.35
2050	0.7-1.3	3.2-3.9	0.20-0.6	0.06-0.14	0.2-0.7	0.25	0.2-0.5
2060	0.6-0.9	3.4-4.5	0.6-1.1	0.05-0.15	0.05-0.5	0.3-0.5	0.1-0.5
2199	1.4-1.8	2.3-2.9	0.05-0.4	0.05-0.12	--	0.2-0.9	0.1-0.5
2099	1.6-2.0	2.4-3.0	0.10-0.5	0.05-0.12	--	0.4-1.0	0.1-0.5
2198	0.8-1.1	2.9-3.5	0.25-0.8	0.04-0.18	0.1-0.5	0.35	0.50

1.3 7XXX Aluminum Alloys

7XXX alloys are Al-Zn-Mg system based aluminum alloys. This category of aluminum alloys is known to have ultra-high strength with maximum yield strength of ≈ 700 MPa [2]. 7XXX alloys have been dominating aerospace aluminum alloys for decades until recently when Al-Li alloys have been seen as strong competitors (Figure 1.2). Both Mg and Zn, main alloying elements of 7XXX, have high solubility in aluminum at higher temperatures. Alloy chemistry of some 7XXX alloys is listed in Table 1.5. Addition of Mg reduces the solubility of Zn in aluminum at lower temperature [40]. After quenching from high temperature, Mg and Zn clusters form the GP zones [41]. 7XXX alloys gain the strength from precipitation of metastable coherent η′ ($MgZn_2$) phase. GP zones act as the precursor to η′ phase. η′ phase transforms into stable but incoherent η phase. The precipitation sequence observed in 7XXX alloys is [41]:

$$\alpha_{\text{supersaturated solid solution}} \rightarrow \text{GP zones} \rightarrow \eta' \rightarrow \eta$$

The structure of η′ is hexagonal with a = 0.496 nm and c = 1.402 nm [42]. 7XXX alloys are considered highly alloyed and thus, quench sensitivity of these alloys is also high. η phase can directly nucleate and grow at sub-grain and grain boundaries during quenching from high temperature process [2]. Commercial Al-Zn-Mg alloys are often alloyed with small to moderate amount of Cu [2]. Although Cu is added to improve the stress corrosion cracking of Al-Zn-Mg alloys as shown in Figure 1.8, it also enhances the strength quotient [2,43,44]. η′ is believed to be a more potent strengthening phase compared to η in Al-Zn-Mg alloys [45]. Presence of heterogeneous nucleation sites such as dislocations favors the formation of η as compared to η′ [46]. Thus, unlike 2XXX alloys, 7XXX are not subjected to deformation prior to aging. For this reason, 7XXX alloys are peak aged in T6 condition compared to T8 in 2XXX alloys. 7XXX alloys are also used in overaged T7 condition to provide improved corrosion properties at the

expense of reduced strength. Al-Cu-Mg based S (Al_2CuMg) phase is also sometimes observed after quenching from high temperature.

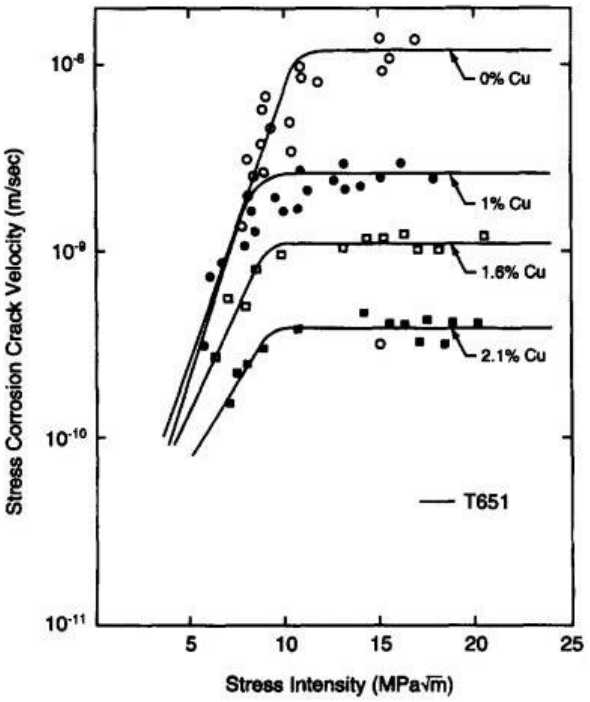

Figure 1.8. Effect of Cu content on stress corrosion cracking for modified 7050 alloys [3].

Table 1.5. Chemical composition limits of a few 7XXX alloys.

Alloy	Zn	Mg	Cu	Zr	Mn	Cr	Ti
7040	5.7-6.7	1.7-2.4	1.5-2.3	0.05-0.12	0.04	0.04	0.06
7050	5.7-6.7	1.9-2.6	2.0-2.6	0.08-0.15	0.10	0.04	0.06
7075	5.1-6.1	2.1-2.9	1.2-2.0	-	0.30	0.18-0.28	0.20
7449	7.5-8.7	1.8-2.7	1.4-2.1	-	0.20	-	-
7475	5.2-6.2	1.9-2.6	1.2-1.9	-	0.06	0.18-0.25	0.06
7095	8.6-9.8	1.4-2.0	2.0-2.8	0.08-0.15	0.05	-	0.06

1.4 Weldability of Precipitation Strengthened Aluminum Alloys

Generally, Al-Li and 7XXX aluminum alloys are considered unweldable using conventional fusion based welding techniques [3,4,24,47-50]. Volatile nature of Mg, Zn, and Li makes joining of these alloys difficult using laser based welding [24,47]. Hydrogen porosity, hot cracking, stress corrosion cracking are the main issues associated with fusion welding of precipitation strengthened aluminum alloys [24,47,48,50]. Figure 1.9 shows two examples of hydrogen porosity and keyhole porosity formed in laser beam welded Al-Li alloy.

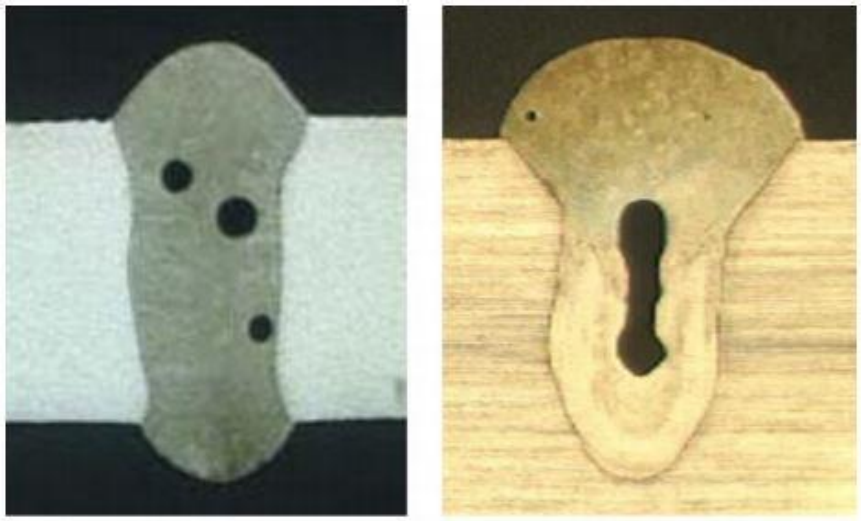

Figure 1.9. Examples of porosity formation in laser beam welding of Al-Li alloys [47].

The main cause of porosity formation during fusion welding of Al-Li and 7XXX alloys is hydrogen contamination. Solubility of hydrogen in molten aluminum is considerably high and reduces by a great extent at room temperature. Therefore, when weld metal solidifies, hydrogen gets trapped into weld pool and forms hydrogen bubbles. Bubbles ends up forming porosity if they cannot escape the molten weld pool before solidification leading to the formation of porosities as shown in Figure 1.9. Although shielding gases are used in most of the fusion welding techniques, but it is extremely difficult to completely eliminate the hydrogen from moisture around the weld pool due to its high diffusivity.

Hot cracking is another persistent issue in fusion welding of Al-Li and 7XXX alloys [24,47]. It usually occurs in weld nugget during solidification. It occurs due to the chemical segregation of low melting eutectic along the grain boundaries during final stages of solidification [24,47,48]. Cracking occurs when the stresses developed due to thermal shrinkage across the neighboring grains exceed the strength of solidifying metal. Depending upon thermal cycle and alloy chemistry, sometimes solidification cracking is also observed in parent material (HAZ) away from weld pool as shown in Figure 1.10. In 7XXX alloys, susceptibility to hot cracking is severely affected by the Cu content of the alloy [2]. As shown in Table 1.5, Cu content in 7XXX alloys is usually below 3 wt.%. Crack susceptibility increases with increase in Cu content in 7XXX alloys.

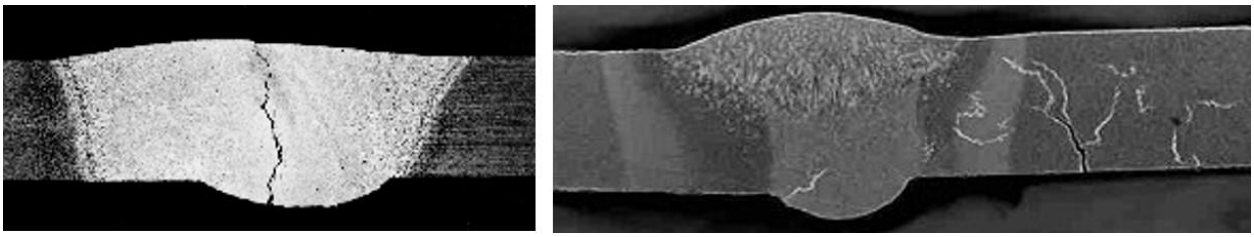

Figure 1.10. Examples of hot cracking in weld zone and HAZ during fusion welding of aluminum alloys [51].

Apart from above mentioned issues, fusion based welding techniques consumes huge power, generates toxic gases and requires highest safety standards [48,50]. Strength and fatigue life of fusion welded structural component can be compromised due to the presence of micro-porosities which may go undetected during non-destructive testing. Solid state joining techniques may solve most of the issues associated with fusion welding of precipitation strengthened aluminum alloys.

1.5 Friction Stir Welding

Friction Stir Welding, a solid state joining process invented at The Welding Institute (TWI,

U.K.) by Thomas et al. [52] in 1991. In this process a non-consumable rotating tool, made of material stronger than workpiece, with a larger diameter shoulder and a pin, plunges into the workpiece to a pre-programmed depth. Plunging of rotating tool into the workpiece produces frictional heat due to the interaction of tool shoulder and workpiece. Another contribution to the temperature input comes from adiabatic heat produced during plastic deformation of workpiece material around the rotating tool pin. Plastic deformation at high temperature leads to the softening of material around the pin. The softened material moves around with the rotation of tool pin which then traverses along a joint line and completes the weld. The larger diameter of tool shoulder helps in containing the hot material which can otherwise flow out easily to form flash and may lead to loss of material and defective weld. Schematic shown in Figure 1.11 illustrates the process for welding of a workpiece in the butt configuration. During FSW, a solid state joining process, melting doesn't take place. Thus, this process is inherently benefitted and diminishes the possibility of common defects like segregation, dendritic structure, and hot cracking, porosity formation associated with fusion based welding techniques [48-50,53,54]. Dissimilar material can also be efficiently joined by using this process [48,50]. Recently, FSW has been used in some applications in aerospace and automobile industries for structural application [48]. FSW is also a green process as the energy consumption during this process usually between 2-5% of energy consumption in laser based welding [48,50]. Another benefit of this process is that the tool is non-consumable and thus the requirement of filler material is completely avoided.

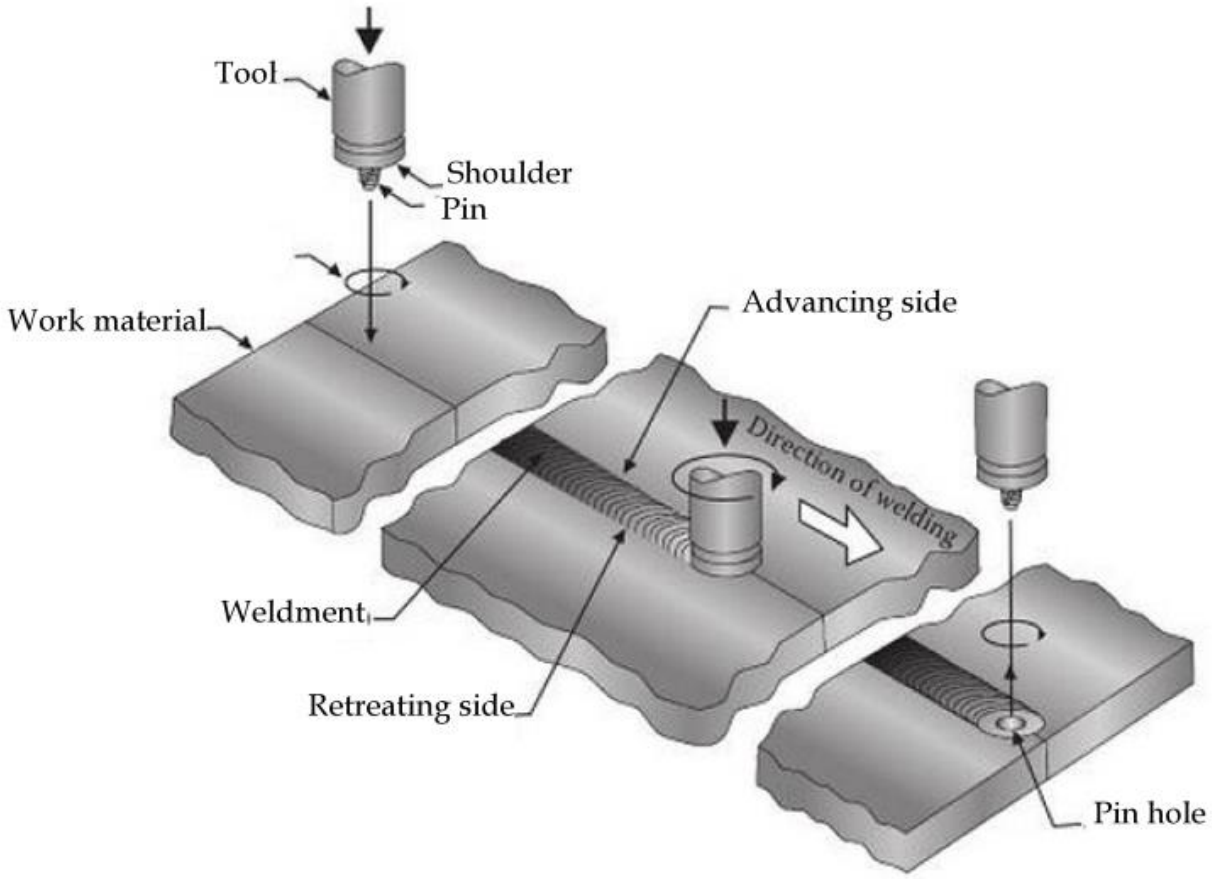

Figure 1.11. Schematic showing operational details of FSW process [55].

1.5.1 Friction Stir Welding of Aluminum Alloys

Friction stir welding of aluminum alloys has been conducted for the past twenty years. A non-consumable tool with a pin is made to run through the joint line of the material to be joined. Heat is produced due to friction between tool shoulder and work piece which softens the material around pin and produces a few microstructural changes in and around weld zone. Resultant microstructure of the weld cross section, the size and distribution of the precipitates in the case of precipitation strengthened alloys, mechanical properties of the weldment and other microstructural features are dependent on the welding parameters, tool dimensions, initial microstructure of workpiece material, and temperature distribution during welding [48,50,54].

1.5.2 Microstructural evolution in FSW of Precipitation Strengthened Aluminum Alloys

Typically, FSW of an aluminum alloy results in three different microstructural zones (also shown in Figure 1.12):

1.5.2.1 Weld Nugget (WN)

Plastic deformation and frictional heat generated during FSW results in transformation of parent material into equiaxed fine grained recrystallized microstructure in the weld nugget. Dislocation density in this zone in case of aluminum alloys is usually low [50]. Grain size in nugget usually ranges in 2-15 μm depending on FSW parameters, tool geometry, composition of material and external cooling used [50]. In aluminum alloys, weld nugget experiences a peak temperature in the range of 400-550ºC during FSW [48,50]. In precipitation strengthened aluminum alloys, such high temperature can lead to coarsening, dissolution and re-precipitation of precipitates depending on thermal stability of precipitate, alloy chemistry, external cooling and peak temperature in weld nugget [54].

1.5.2.2 Thermo-Mechanical Affected Zone (TMAZ)

Zone between parent material and nugget having experienced both temperature and plastic deformation during FSW is the thermo-mechanically affected zone (TMAZ) [49,50]. Partial recrystallization is generally observed in TMAZ [49,50]. Dislocation density is very high in TMAZ due to high plastic deformation which leads to formation of sub-grain boundaries [50]. Dissolution of strengthening precipitates might occur in this zone during welding. Extent of dissolution varies depending on the thermal cycle experienced by TMAZ and the type of alloy.

1.5.2.3 Heat Affected Zone (HAZ)

The zone separating TMAZ and base material is the heat affected zone (HAZ). This zone does not undergo any plastic deformation and experiences thermal cycle. For a given welding

parameter, formation of HAZ depends upon the alloy being welded. Generally, an area away from WN which experiences a temperature cycle in the range of 250-350°C during welding is observed as HAZ [50]. HAZ is characterized by the coarsening of strengthening precipitates and the precipitate free zone formation due to high temperature exposure [50]. Use of external cooling medium can reduce the extent of formation of HAZ.

Usually FSW results in asymmetric weld cross section. The side where tangential velocity of the tool is along the welding direction, is called the advancing side (AS). The other side, where tangential velocity of the tool is opposite to the welding direction is called retreating side (RS).

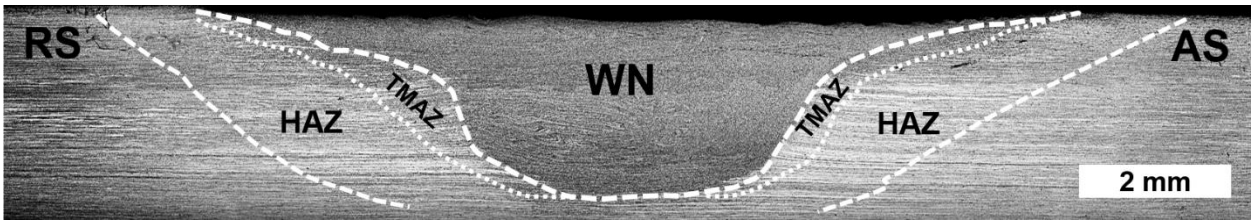

Figure 1.12. Weld cross section showing various metallurgical zones developed during FSW of an aluminum alloy.

FSW of various precipitation strengthened aluminum alloys results in a variety of microstructure. Of course, initial microstructure and alloy chemistry plays the most important role in determining the final microstructure. Factors like tool geometry, choice of welding parameters, workpiece thickness, thermal cycle during welding, and auxiliary cooling also greatly influence the resultant microstructure and strength of the weldment.

1.6 References

[1] J.D. Minford, Handbook of Aluminum Bonding Technology and Data, CRC Press, 1993.

[2] G.E. Totten, D.S. MacKenzie, Handbook of Aluminum: Vol. 1: Physical Metallurgy and Processes, CRC Press, 2003.

[3] E. Starke, J. Staley, Application of modern aluminum alloys to aircraft, Prog. Aerospace Sci. 32 (1996) 131-172.

[4] T. Dursun, C. Soutis, Recent developments in advanced aircraft aluminium alloys, Mater Des. 56 (2014) 862-871.

[5] Aluminum Association, Aluminum Standards and Data, Aluminum Association., 2000.

[6] R. Abbaschian, R. Reed-Hill, Physical Metallurgy Principles, Cengage Learning, 2008.

[7] J.W. Martin, Precipitation Hardening: Theory and Applications, Butterworth-Heinemann, 2012.

[8] T. Gladman, Precipitation hardening in metals, Materials science and technology. 15 (1999) 30-36.

[9] J.C. Benedyk, International Temper Designation Systems for Wrought Aluminum Alloys, Light Met. Age. (2009).

[10] Alcoa Inc., http://www.alcoa.com/.

[11] K. Sankaran, N. Grant, The structure and properties of splat-quenched aluminum alloy 2024 containing lithium additions, Materials Science and Engineering. 44 (1980) 213-227.

[12] E.J. Lavernia, N.J. Grant, Aluminium-lithium alloys, J. Mater. Sci. 22 (1987) 1521-1529.

[13] N.E. Prasad, A. Gokhale, R. Wanhill, Aluminum-Lithium Alloys: Processing, Properties, and Applications, Butterworth-Heinemann, 2013.

[14] I. Fridlyander, Aluminum alloys with lithium and magnesium, Metal science and heat treatment. 45 (2003) 344-347.

[15] I. Fridlyander, A. Dobromyslov, E. Tkachenko, O. Senatorova, Advanced high-strength aluminum-base materials, Metal science and heat treatment. 47 (2005) 269-275.

[16] I. Fridlyander, V. Sister, O. Grushko, V. Berstenev, L. Sheveleva, L. Ivanova, Aluminum

alloys: Promising materials in the automotive industry, Metal science and heat treatment. 44 (2002) 365-370.

[17] I. Fridlyander, L. Khokhlatova, N. Kolobnev, K. Rendiks, G. Tempus, Thermally stable aluminum-lithium alloy 1424 for application in welded fuselage, Metal science and heat treatment. 44 (2002) 3-8.

[18] N. Facts, Super Lightweight External Tank, National Aeronautics and Space Administration, Marshall Space Flight Center Huntsville, Alabama. 35812 (2005).

[19] J.C. Williams, E.A. Starke, Progress in structural materials for aerospace systems, Acta Materialia. 51 (2003) 5775-5799.

[20] B. Noble, G. Thompson, Precipitation characteristics of aluminium-lithium alloys, Metal Science Journal. 5 (1971) 114-120.

[21] B. Noble, G. Thompson, T 1 (Al2CuLi) Precipitation in Aluminium–Copper–Lithium Alloys, Metal Science Journal. 6 (1972) 167-174.

[22] D. Williams, J. Edington, The Precipitation of δ′(Al3Li) in Dilute Aluminium–Lithium Alloys, Metal Science. 9 (1975) 529-532.

[23] A. Deschamps, C. Sigli, T. Mourey, F. De Geuser, W. Lefebvre, B. Davo, Experimental and modelling assessment of precipitation kinetics in an Al–Li–Mg alloy, Acta Materialia. 60 (2012) 1917-1928.

[24] A. Kostrivas, J. Lippold, Weldability of Li-bearing aluminium alloys, International materials reviews. 44 (1999) 217-237.

[25] W. Cassada, G. Shiflet, E. Starke, The effect of plastic deformation on Al2CuLi (T 1) precipitation, Metallurgical Transactions A. 22 (1991) 299-306.

[26] A.K. Shukla, W.A. Baeslack III, Study of microstructural evolution in friction-stir welded

thin-sheet Al–Cu–Li alloy using transmission-electron microscopy, Scr. Mater. 56 (2007) 513-516.

[27] A.K. Shukla, Friction stir welding of thin-sheet, age-hardenable aluminum alloys: A study of process/structure/property relationships, ProQuest Dissertations and Theses. (2007).

[28] A. Shukla, W. Baeslack III, Study of process/structure/property relationships in friction stir welded thin sheet Al–Cu–Li alloy, Science and Technology of Welding & Joining. 14 (2009) 376-387.

[29] H.H. Jo, K. Hirano, Precipitation Processes in Al-Cu-Li Alloy Studied by DSC, 13 (1987) 377-382.

[30] B. Decreus, A. Deschamps, F. De Geuser, P. Donnadieu, C. Sigli, M. Weyland, The influence of Cu/Li ratio on precipitation in Al–Cu–Li–x alloys, Acta Materialia. 61 (2013) 2207-2218.

[31] G.H. Narayanan, W. Quist, B. Wilson, A. Wingert, Low density aluminum alloy development, AFWAL Contract F33615-81-c-5053. (1982).

[32] B.-. Huang, Z.-. Zheng, Independent and combined roles of trace Mg and Ag additions in properties precipitation process and precipitation kinetics of Al–Cu–Li–(Mg)–(Ag)–Zr–Ti alloys, Acta Materialia. 46 (1998) 4381-4393.

[33] R.J. Rioja, J. Liu, The evolution of Al-Li base products for aerospace and space applications, Metallurgical and Materials Transactions A. 43 (2012) 3325-3337.

[34] F.W. Gayle, J.B. Vander Sande, "Composite" precipitates in an Al-Li-Zr alloy, Scripta metallurgica. 18 (1984) 473-478.

[35] Y. Miura, K. Horikawa, K. Yamada, M. Nakayama, Precipitation hardening in an Al–2.4 Li–0.19 Sc alloy, Aluminum alloys: their physical and mechanical properties. 2 (1994) 161-

168.

[36] F.W. Gayle, J.B. Vander Sande, A. McAlister, The Al-Li (Aluminum-Lithium) system, Journal of Phase Equilibria. 5 (1984) 19-20.

[37] P. Gregson, H. Flower, δ′ precipitation in Al-Li-Mg-Cu-Zr alloys, J. Mater. Sci. Lett. 3 (1984) 829-834.

[38] J. Wadsworth, A. Pelton, Superplastic behavior of a powder-source aluminum-lithium based alloy, Scripta metallurgica. 18 (1984) 387-392.

[39] W. Cassada, G. Shiflet, E. Starke, The effect of plastic deformation on Al2CuLi (T 1) precipitation, Metallurgical Transactions A. 22 (1991) 299-306.

[40] I. Polmear, The Upper Temperature Limit of Stability of Gp Zones in Ternary Aluminium Zinc Magnesium Alloys, Journal of the Institute of Metals. 87 (1958) 24-25.

[41] J. Lendvai, Precipitation and strengthening in aluminium alloys, 217 (1996) 43-56.

[42] X. Li, V. Hansen, J. Gjønnes, L. Wallenberg, HREM study and structure modeling of the η′ phase, the hardening precipitates in commercial Al–Zn–Mg alloys, Acta materialia. 47 (1999) 2651-2659.

[43] E.A. Starke Jr, Heat-treatable aluminum alloys, Aluminum Alloys--Contemporary Research and Applications: Contemporary Research and Applications. (2012) 31.

[44] I. Polmear, Recent developments in light alloys, Mater. Trans. JIM. 37 (1996) 12-31.

[45] J. Staley, Metallurgical aspects affecting strength of heat-treatable alloy products used in the aerospace industry, (1992) 22-26.

[46] A. Deschamps, F. Livet, Y. Brechet, Influence of predeformation on ageing in an Al–Zn–Mg alloy—I. Microstructure evolution and mechanical properties, Acta Materialia. 47 (1998) 281-292.

[47] R. Xiao, X. Zhang, Problems and issues in laser beam welding of aluminum–lithium alloys, Journal of Manufacturing Processes. 16 (2014) 166-175.

[48] R.S. Mishra, P.S. De, N. Kumar, Friction Stir Welding and Processing: Science and Engineering, Springer, 2014.

[49] R.S. Mishra, M.W. Mahoney, Friction Stir Welding and Processing, ASM International, 2007.

[50] R.S. Mishra, Z. Ma, Friction stir welding and processing, Materials Science and Engineering: R: Reports. 50 (2005) 1-78.

[51] The Welding Institute, http://www.twi-global.com/technical-knowledge/job-knowledge/weldability-of-materials-aluminium-alloys-021/.

[52] W. Thomas, E. Nicholas, J. Needham, M. Murch, P. Templesmith, C. Dawes, International patent application no. (1991).

[53] R.S. Mishra, P.S. De, N. Kumar, Fundamentals of the Friction Stir Process, Springer, 2014.

[54] P.S. De, R.S. Mishra, Friction stir welding of precipitation strengthened aluminium alloys: scope and challenges Science and Technology of Welding and Joining. 16 (2011) 343-347.

[55] J.T. Khairuddin, I.P. Almanar, J. Abdullah, Z. Hussain, Principles and Thermo-Mechanical Model of Friction Stir Welding, INTECH Open Access Publisher, 2012.

CHAPTER 2

PAPER I: EFFECT OF WELDING TEMPERATURE ON HARDNESS EVOLUTION IN WELD NUGGET DURING POST WELD HEAT TREATMENT OF FRICTION STIR WELDED Al-Cu, Al-Cu-Li, AND Al-Zn-Mg ALLOYS

2.1 Abstract

Friction stir welding of three different precipitation strengthened aluminum alloys (2219, 2195, and 7050) based on Al-Cu, Al-Cu-Li, and Al-Zn-Mg system was conducted. Several welds were produced in which peak temperatures ranged from 332°C to 535°C. Maximum peak temperature possible during welding was found to be related to solidus temperature of the alloy. After post weld heat treatment, hardness in weld nugget was observed to higher for the welds experienced higher temperature during welding. Differential scanning calorimetry study was used to establish that the hardness recovery after aging was directly related to the extent of formation of supersaturated solid solution during welding. Welds of 2219 and 7050 alloy with peak temperature reaching close to solution temperature of the alloy showed hardness close to peak aged parent material.

Keywords: Friction stir welding, precipitation strengthening, aluminum alloys, differential scanning calorimetry

2.2 Introduction

Precipitation strengthened 2XXX (Al-Cu, Al-Cu-Mg, and Al-Cu-Li) and 7XXX (Al-Zn-Mg) aluminum alloys are widely used in aerospace industries [1]. Al-Cu alloys are known to be strengthened by precipitation of metastable θ′ (Al_2Cu) and stable θ (Al_2Cu) phases, whereas δ′ (Al_3Li), θ′ (Al_2Cu) and T1 (Al_2CuLi) phases for Al-Cu-Li system. Al-Zn-Mg system is strengthened by metastable η′ ($MgZn_2$) and stable η phase [2-4]. Welding is a critical step in

manufacturing of integrated systems. 2XXX and 7XXX are considered non-weldable using conventional fusion welding techniques [5,6]. Friction stir welding (FSW) has evolved as a preferred method for welding and joining of aluminum alloys in aerospace industries [5,6]. FSW inherently eliminates the flaws associated with fusion welding of aluminum alloys [5,6]. During FSW, weld nugget (WN), thermo-mechanically affected zone (TMAZ), and heat affected zone (HAZ) are the metallurgical zones formed and one of them is observed to be the weakest link depending upon alloy chemistry, welding parameters and initial microstructure [5-7]. HAZ is characterized by the loss of strength due to coarsening of precipitates during thermal cycle of welding. Whereas WN experience large deformation and thermal cycles and parent material grain structure is completely replaced by recrystallized grains [5,6,8]. TMAZ is the transition zone between WN and HAZ. The strength of the weldment mainly depends on the strength evolution in HAZ and WN. Strength in HAZ can be manipulated by using auxiliary cooling methods. WN strength after FSW can be improved by artificial aging of weldment. WN goes through formation of solid solution during welding. Extent of supersaturation of solutes in solid solution after welding affects the strength recovery during artificial aging. Temperature in WN during welding dictates the formation of solid solution.

A number of experimental studies exist on FSW of 2XXX and 7XXX [9-21]. Most of the studies have focused on microstructural and strength evolution for a single welding parameter. Since workpiece in FSW doesn't undergo melting and welding can take place over a wide range of temperature depending on welding parameters and tool dimensions. Thus, there exist a need to study the effect of temperature evolved during FSW on the strength evolution in WN precipitation strengthened aluminum alloys after artificial aging.

2.3 Materials and Methods

The chemical compositions of precipitation strengthened aluminum alloys 2219-T8, 2195-T8, and 7050-T7 used in this study are listed in Table 2.1. The welding tool consisted of 3.1 mm long step-spiral pin of diameter 6.2 mm tapering down to 4.5 mm. Three tools with shoulder diameter of 12 mm, 16 mm, and 22 mm with same pin dimensions were used to obtain welds with different temperature. To minimize the effect of strain history during welding on hardness evolution, majority of the welds were made with same welding parameters of tool rotation rate of 600 revolutions per minute (RPM) and traverse speed of 500 millimeters per minute (mmPM). Parameters of welds made with different parameters to achieve higher welding temperature are shown in Figure 2.1. The temperature during welding was recorded for all the welds using a thermocouple inserted in the tool pin. Figure 2.1 also shows the peak tool temperature for all the welds. In some cases, underwater welding (UWFSW) was conducted with workpiece and tool submerged in water to produce welds with low welding temperature.

Table 2.1 Chemical composition of key alloying elements in 2219, 2195, and 7050 alloy.

Alloy	Cu	Mg	Zn	Li	Mn	Zr	Ag
2219	5.8-6.8	0.02	0.10	-	0.2-0.4	0.10-0.25	-
2195	3.7-4.3	0.25-0.80	0.25	0.8-1.2	0.25	0.08-0.16	0.25-0.60
7050	2.0-2.6	1.9-2.6	5.7-6.7	-	0.10	0.08-0.15	-

Vickers microhardness measurements were taken along the depth of the WN for all the welds in as-welded (AW) and post weld heat treated (PWHT) condition. For PWHT, welds of alloy 2219 and 2195 were held at 160°C for 17 hours, and welds of alloy 7050 were held at 121°C for 25 hours. Differential scanning calorimetry (DSC) was carried out for selected samples on a Netzsch 204 F1 Phoenix® system operating at a heating rate of 10°C per minute.

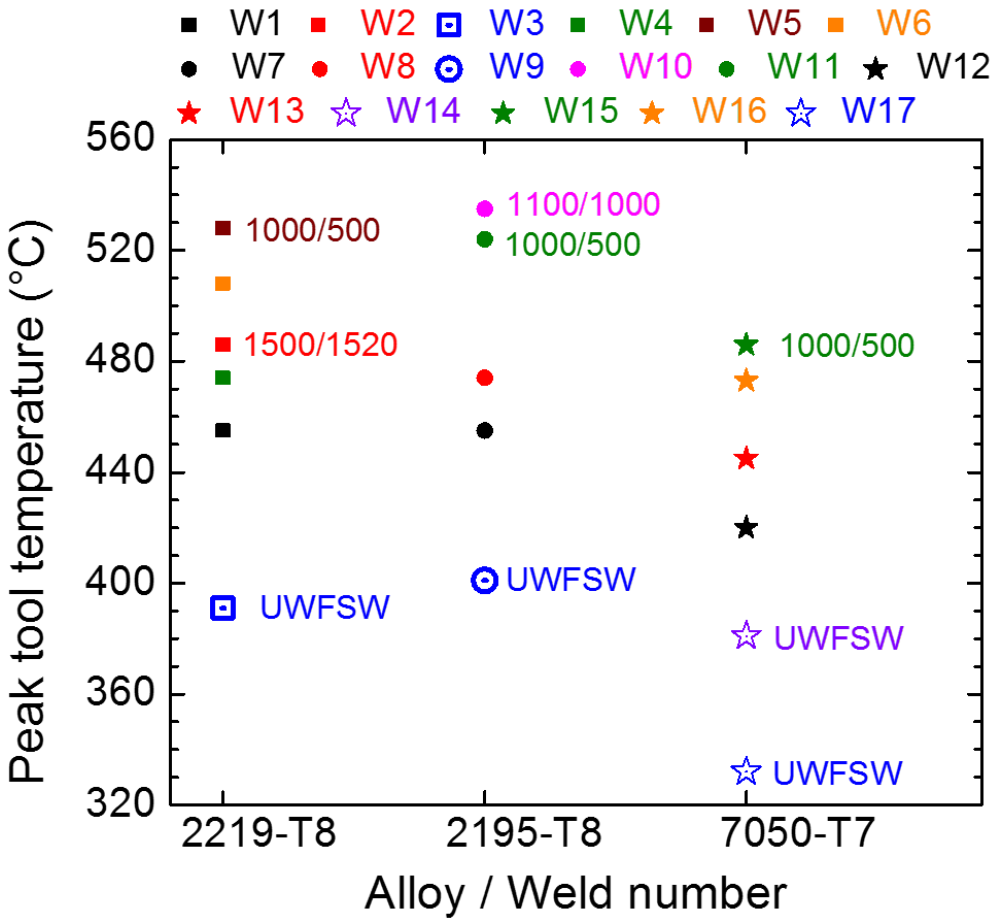

Figure 2.1 Plot of peak weld temperature for all the welds. Note that welding parameters (RPM/mmPM) are also shown for welds in which it was different from 600 RPM and 500 mmPM. Welds made underwater are shown as UWFSW.

2.4 Results and Discussion

It is clear from Figure 2.1 that maximum peak temperature achieved during FSW greatly depends on the alloy being welded. W11 (2195 alloy) and W15 (7050 alloy) were made using same tool and parameters showed a difference of 40°C in peak temperature. Similar trends were observed in case of UWFSW of all three alloys. UWFSW of 7050 (W17) resulted in much lower peak temperature compared to the case of UWFSW of 2195 (W9) and 2219 (W3). It can be seen that maximum peak temperature during FSW for an alloy corresponds to solidus temperature of

the alloy. Solidus temperature for 2219, 2195, and 7050 are 543°C, 543°C, and 485°C respectively. During FSW, temperature rises due to the generation of frictional heat between tool and workpiece. Efforts to increase the temperature close to solidus temperature by changing welding parameters results in incipient melting of alloy as the friction between tool and partially molten workpiece will reduce. Thus, maximum peak temperature possible during FSW of aluminum alloy is the solidus temperature of the alloy.

Vickers microhardness results of all the welds of alloy 2219 in AW and PWHT condition are shown in Figure 2.2a. In AW condition, hardness in the WN was observed to be in the range of 88-104 HV. Generally, hardness for welds with higher peak temperature were higher. After PWHT, hardness improved for all the welds except W3. Welds with higher peak temperature showed higher hardness recovery after PWHT. W5, which experienced peak temperature of 526°C, showed hardness of 140 HV at the top of WN. Hardness in W4 (peak temperature 474°C) improved to 130 HV at the top of WN. W1, in which peak temperature was around 455°C, the hardness increased from 97 HV to 118 HV. UWFSW to produce W3 resulted in low peak temperature of 391°C. After PWHT, W3 showed negligible improvement in hardness. Figure 2.2b show the hardness results of all the welds of alloy 2195 in AW and PWHT condition. Trends in hardness results were similar to welds of 2219 alloy. In AW condition, hardness for all the welds (W7-W11) fluctuated between 118-124 HV. After PWHT, W10 which experienced highest peak temperature of 535°C showed the highest improvement in hardness (151 HV). Welds with lower peak temperature showed low recovery in hardness. W9 in which peak temperature was around 401°C showed lowest hardness recovery as shown in Figure 2.2b. Similarly, in case of welds of alloy 7050 (W12-W17), hardness improvement was highest for welds made with higher peak temperature as shown in Figure 2.2c. W17 (UWFSW), in which

peak temperature was 332°C, showed very low hardness in both AW and PWHT condition.

FSW is a solid state joining process. Thermal cycle and deformation during welding can result in varying degree of solutionization of alloy in WN. Note, effect of cooling after welding is excluded here as high traverse speed of 500 mmPM and above are high enough to generates high cooling rates to avoid this factor. As shown in Figure 2.2d, the extent of soltionization of alloy depends upon the peak temperature achieved during welding. Welds experiencing higher temperature (W5) contains higher solute content in solid solution as compared to low temperature welds (W3). Higher solute content facilitates higher volume fraction of strengthening precipitates after PWHT. DSC experiment were carried out to further investigate the characteristics of WN of various welds which underwent contrasting temperatures.

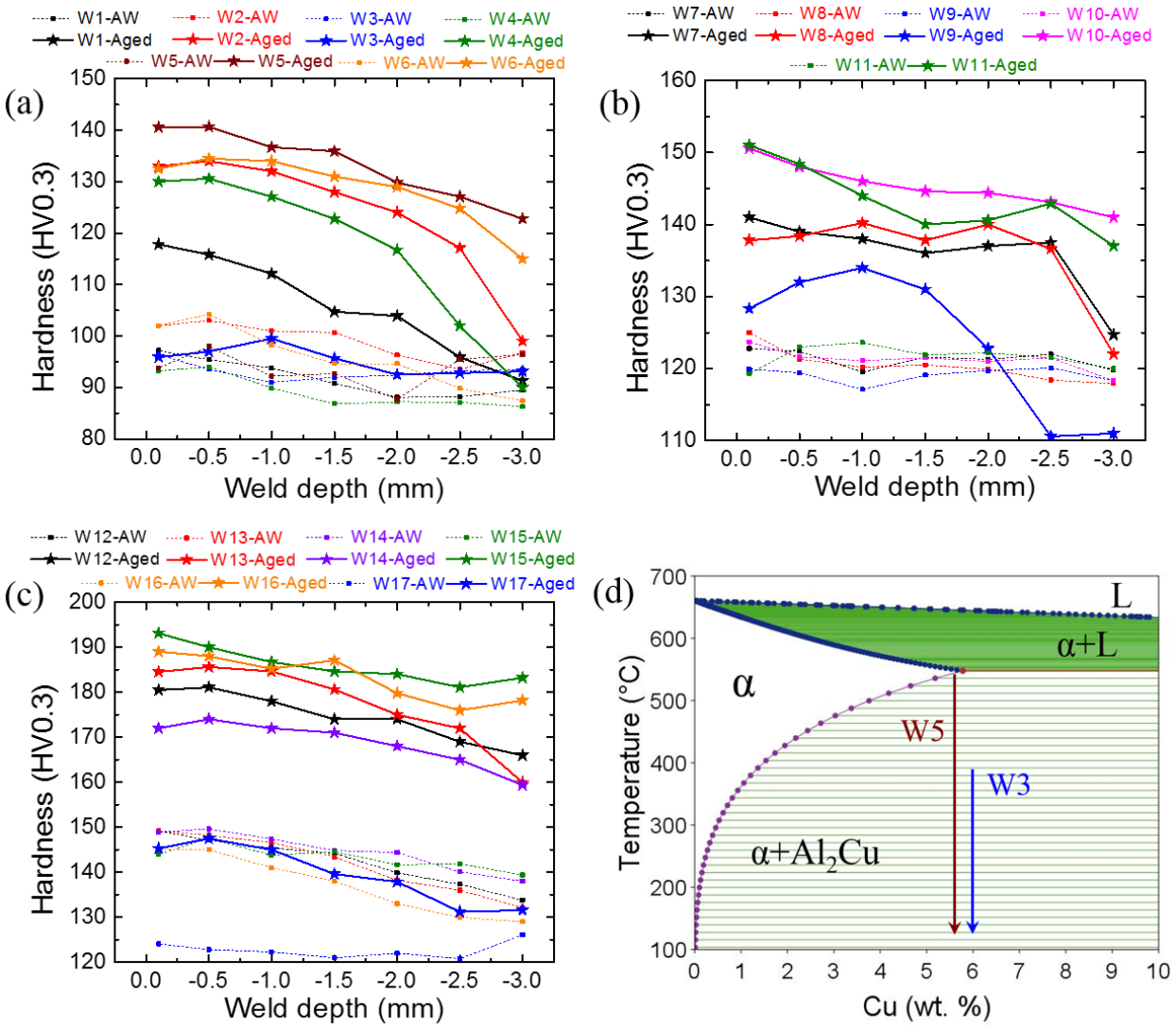

Figure 2.2 Vickers microhardness results of (a) W1-W6, (b) W7-W11, and (c) W12-W17 in AW and PWHT condition, and (d) equilibrium phase diagram of Al-Cu system.

DSC has been previously demonstrated as a powerful tool to study the precipitation in aluminum alloys [22]. Exothermic and endothermic peaks in DSC plots corresponds to precipitation and dissolution of various phases respectively [22]. The amplitude of a peak corresponds to the volume fraction of phase precipitating or dissolving. Figure 2.3 shows DSC results of samples from WN of welds of 2219 and 7050 alloy which experienced highest (W5 and W15) and lowest (W3 and W17) temperature during welding. For this study, only peaks

associated with key strengthening precipitates will be discussed as labeled in Figure 2.3a and b. The exothermic peak shown in Figure 2.3a, for welds of Al-Cu based alloy (2219), is due to the precipitation of Al_2Cu phase. Larger amplitude of the precipitation peak for sample from W5 as compared to that of W3, shows that the solute content in solid solution of W5 was substantially higher which resulted in high volume fraction of precipitates during PWHT. Figure 2.3b show peaks of GP zone dissolution and precipitation of $MgZn_2$ phase commonly observed in 7XXX alloys [23]. GP zones are the clusters of solute atoms formed due to natural aging and acts as precursors to strengthening precipitates. It is clearly evident from the DSC results that higher volume fraction of GP zones were formed in W15 as compared to W17. Also, after dissolution of GP zones, larger precipitation event signifies towards higher supersaturation of solutes in solid solution in W15.

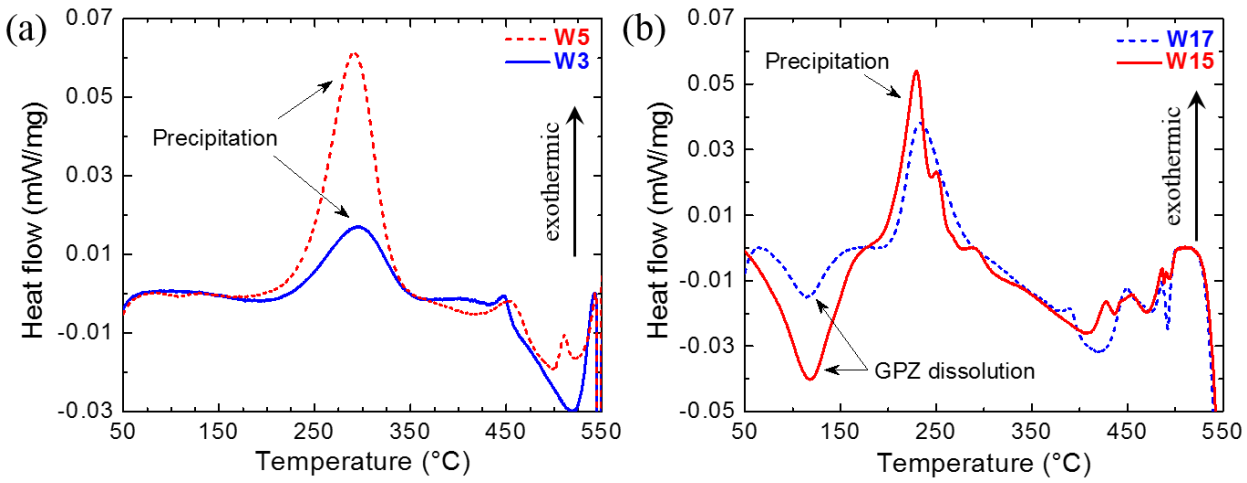

Figure 2.3 DSC results of sample taken from WN of (a) W3 and W5, and (b) W15 and W17 in AW condition.

2.5 Conclusion

Temperature measurements from the core of tool pin during welding suggests that maximum peak temperature achievable during FSW of aluminum alloys is limited to the solidus

of the alloy beyond which incipient melting of the alloy reduces the frictional heat content. Higher temperature during FSW of precipitation strengthened aluminum alloys result in formation of higher supersaturation of solutes in solid solution as compared to lower temperature welds. Improvement in hardness in WN after PWHT is higher for welds with higher welding temperature. Hardness in WN can improved close to parent material hardness by optimizing the parameters and tool construction to obtain weld with peak temperature close to the range of solution temperature of the alloy.

Acknowledgments

This work was supported under the NSF-IUCRC grant for Friction Stir Processing (NSF-IIP 1157754) for Center for Friction Stir Processing (CFSP) at University of North Texas, United States.

2.6 References

[1] Dursun T, Soutis C. Recent developments in advanced aircraft aluminium alloys. Mater Des 2014;56:862-71.

[2] Buha J, Lumley RN, Crosky AG. Secondary ageing in an aluminium alloy 7050. Materials Science and Engineering: A 2008;492:1-10.

[3] Cassada W, Shiflet G, Starke E. The effect of plastic deformation on Al2CuLi (T 1) precipitation. Metallurgical Transactions A 1991;22:299-306.

[4] Xu W, Liu J, Luan G, Dong C. Temperature evolution, microstructure and mechanical properties of friction stir welded thick 2219-O aluminum alloy joints. Mater Des 2009;30:1886-93.

[5] Mishra RS, Ma Z. Friction stir welding and processing. Materials Science and Engineering: R: Reports 2005;50:1-78.

[6] Mishra RS, De PS, Kumar N. Friction Stir Welding and Processing: Science and Engineering. : Springer, 2014.

[7] De PS, Mishra RS. Friction stir welding of precipitation strengthened aluminium alloys: scope and challenges Science and Technology of Welding and Joining 2011;16:343-347.

[8] Threadgill P, Leonard A, Shercliff H, Withers P. Friction stir welding of aluminium alloys. International Materials Reviews 2009;54:49-93.

[9] Avettand-Fenoel M, Taillard R. Heterogeneity of the Nugget Microstructure in a Thick 2050 Al Friction-Stirred Weld. Metallurgical and Materials Transactions A 2015;46:300-14.

[10] Cavaliere P, Cabibbo M, Panella F, Squillace A. 2198 Al–Li plates joined by Friction Stir Welding: Mechanical and microstructural behavior. Mater Des 2009;30:3622-31.

[11] Chen PS, Kuruvilla AK, Malone TW, Stanton WP. The Effects of Artificial Aging on the Microstructure and Fracture Toughness of Al-Cu-Li Alloy 2195 Journal of Materials Engineering and Performance 1998;7:682-690.

[12] De Geuser F, Malard B, Deschamps A. Microstructure mapping of a friction stir welded AA2050 Al–Li–Cu in the T8 state Philosophical Magazine 2014;94:1451-1462.

[13] Dhondt M, Aubert I, Saintier N, Olive J. Mechanical behavior of periodical microstructure induced by friction stir welding on Al–Cu–Li 2050 alloy. Materials Science and Engineering: A 2015;644:69-75.

[14] Dumont M, Steuwer A, Deschamps A, Peel M, Withers P. Microstructure mapping in friction stir welds of 7449 aluminium alloy using SAXS. Acta materialia 2006;54:4793-801.

[15] Fuller CB, Mahoney MW, Calabrese M, Micona L. Evolution of microstructure and mechanical properties in naturally aged 7050 and 7075 Al friction stir welds. Materials Science and Engineering: A 2010;527:2233-40.

[16] Mahoney M, Rhodes C, Flintoff J, Bingel W, Spurling R. Properties of friction-stir-welded 7075 T651 aluminum. Metallurgical and materials transactions A 1998;29:1955-64.

[17] Rhodes C, Mahoney M, Bingel W, Calabrese M. Fine-grain evolution in friction-stir processed 7050 aluminum. Scr Mater 2003;48:1451-5.

[18] Sutton MA, Yang B, Reynolds AP, Yan J. Banded microstructure in 2024-T351 and 2524-T351 aluminum friction stir welds: Part II. Mechanical characterization. Materials Science and Engineering: A 2004;364:66-74.

[19] Sullivan A, Robson J. Microstructural properties of friction stir welded and post-weld heat-treated 7449 aluminium alloy thick plate. Materials Science and Engineering: A 2008;478:351-60.

[20] Su J, Nelson T, Mishra R, Mahoney M. Microstructural investigation of friction stir welded 7050-T651 aluminium. Acta materialia 2003;51:713-29.

[21] Su J, Nelson TW, Sterling CJ. Microstructure evolution during FSW/FSP of high strength aluminum alloys. Materials Science and Engineering: A 2005;405:277-86.

[22] Starink M. Analysis of aluminium based alloys by calorimetry: quantitative analysis of reactions and reaction kinetics. International Materials Reviews 2004;49:191-226.

[23] Li X, Starink M. DSC study on phase transitions and their correlation with properties of overaged Al-Zn-Mg-Cu alloys. Journal of materials engineering and performance 2012;21:977-84.

CHAPTER 3

PAPER II: FRICTION STIR WELDING OF Al-Mg-Li 1424 ALLOY[1]

3.1 Abstract

Friction stir welding of 1424 Al-Mg-Li alloy was conducted using tool rotation rate of 800 revolutions per minute and traverse speed of 305 millimeters per minute. Two welds with different thermal conditions were made by using external cooling mediums. The temperature at the tool center was recorded for each weld. After post weld heat treatment, full recovery of strength was observed in the heat affect zone and the weld nugget. High joint efficiency of 97% of the base material was achieved. Transmission electron microscopy and differential scanning calorimetry studies were performed for microstructural evaluation. Homogenous and high density of Al_3Li precipitation was reasoned for high strength joints.

Keywords: Friction stir welding, Al-Mg-Li alloy, Al_3Li precipitate

3.2 Introduction

Al-Li alloys are regaining significant attention from the aerospace industry, as these offer higher specific strength compared to conventional aerospace aluminum alloys [1,2]. Al-Cu-Li and Al-Mg-Li are the two industrially used categories of Al-Li alloys [1,3]. Al-Cu-Li alloys possess high strength comparable to 7XXX aluminum alloys and hence are targeted at high strength applications [4,5]. Al-Mg-Li alloys are ultra-light (density = 2.54 g/cm^3) and have moderate strength levels comparable to those of Al 2XXX alloys (except Al-Cu-Li alloys) [1,2,6-8].

Alloy 1424 is a heat treatable Al-Mg-Li-Zr alloy that was developed out of 1420 and 1421

[1] This chapter is presented in its entirety from Sidhar, H., Martinez, N. Y., Mishra, R. S., & Silvanus, J. (2016). Friction stir welding of Al–Mg–Li 1424 alloy. Materials & Design, 106, 146-152 with permission from Elsevier.

alloys [6,7]. It achieves strength primarily from precipitation of metastable phase δ' (Al_3Li) and solid solution strengthening offered by Mg [1,9]. The δ' precipitate has $L1_2$ ordered structure and is coherent with aluminum matrix [10].The δ' particles are spherical and have very small interfacial energy of $\approx 10 mJ/m^2$ [11]. It is well known that the δ' phase precipitates are stable in the 100-180°C range and dissolves on exposure to temperature higher than 200°C [1,10,12]. Other phases such as β' (Al_3Zr) dispersoid and S_1 (Al_2MgLi) precipitate could also form in this alloy [1,9].The β' phase is known to suppress recrystallization and grain growth in aluminum alloys [1,4,9]. Low volume fraction of S_1 precipitates heterogeneously on grain boundaries and increases after longer aging time [12].

Thermally stable 1424 was developed in Russia with an aim to replace heavier 2024 aluminum alloy (density = 2.78 g/cm^3) from fuselage application in airplanes [7]. In the recent past, Al-Mg-Li alloys have had applications in the aerospace industry [1,2,6,8]. Since welding of aluminum alloys has always been difficult, mechanical fasteners are still used in joining the primary structure of an airplane. Friction stir welding (FSW), invented in 1991 [13], intrinsically eliminates most of the problems encountered in fusion welding of aluminum alloys [14,15]. In the last two decades, FSW has evolved as a viable joining process for many applications in the aerospace and automotive industries [14-19].Robustness of FSW has a potential to overcome the huge cost driven non-destructive testing which is mandatory for fusion welding process.

Mechanical properties, multi-step aging, thermal stability, and precipitation behavior of alloy 1424 have been studied and reported [6-8,12]. Information on the study of FSW of precipitation strengthened Al-Mg-Li alloys is much less. Wei et al. [20] studied the effect of FSW parameters on mechanical properties of heat treatable Al-Mg-Li alloy 01420, but the precipitation behavior of the alloy was not addressed. A few studies on welding of precipitation

strengthened Al-Mg-Li alloys using laser based welding techniques have been reported [8,21-23]. Due to porosity and hot cracking issues, laser and fusion based welding of aluminum alloys are rare in structural applications in the aerospace industry [24]. FSW is being used for many applications in the aerospace sector [1,14]. Therefore, the welding characteristics of alloy 1424 using FSW is of interest.

In this paper, we evaluate and discuss the joining of 1424 alloy using FSW. The aim was to study how external cooling during welding affected the properties of welded joints. The effect of post weld heat treatment (PWHT) on microstructural and mechanical property evolution was also studied. In addition to mechanical testing, differential scanning calorimetry (DSC) and transmission electron microscopy (TEM) were used for property and microstructural analysis.

3.3 Materials and Methods

3.3.1 Friction Stir Welding

The material used in this study was a 3.3 mm thick sheet of 1424 aluminum alloy in peak aged condition. Alloy composition is listed in Table 3.1. Friction stir welding was carried out on a MTI RM-1 friction stir welding system with a tool rotation rate of 800 revolutions per minute (RPM) and welding speed of 305 millimeters per minute (mmPM). The tool used for welding consisted of 2.3 mm long step-spiral conical pin of 6.2 mm diameter tapering down to 3.5 mm and a shoulder diameter of 12 mm. 1424 is a precipitation strengthened alloy; thus, external cooling mediums were used to produce two welds with different thermal experience during welding. Weld 1 (W1) was made on a regular welding bed (steel backing) and ambient cooling as the heat sink. In weld 2 (W2), a water-drenched paint roller traversing behind the welding tool and a copper backing plate were used to facilitate higher cooling rate and lower peak temperature as compared to weld 1. Figure 3.1a shows the schematic of external cooling medium used during

weld 2. Tool temperature was measured with a thermocouple inserted at the tool center as shown in the schematic in Figure 3.1b.

Table 3.1 Chemical composition of alloy 1424 used in this study.

Element	Li	Mg	Zr	Zn	Sc
Weight (%)	1.61	5.4	0.09	0.7	0.07

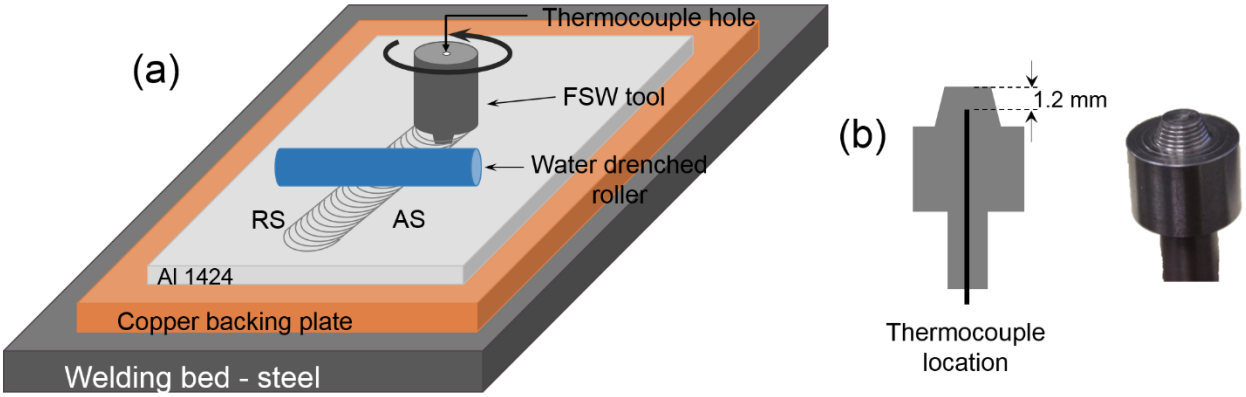

Figure 3.1(a) Schematic of the welding setup used in weld 2, and (b) schematic showing thermocouple location for temperature measurement and image of actual tool used.

Mechanical property and microstructural evaluation was conducted for both welds in as-welded and post weld heat treated (PWHT) conditions. PWHT was carried out in a forced air oven at 160°C for 16 hours. Vickers microhardness mapping across the weld cross section was conducted using 300 g load (HV0.3) on Wilson Tukon 1202 hardness tester. A grid spacing of 500 µm between subsequent indentations was used for hardness measurements. Transverse tensile testing samples with thickness of 2.3 mm and gauge length of 32 mm were prepared according to ASTM-E8 (sub-size) standard.

3.3.2 Microstructural Evaluation

Transmission electron microscopy (TEM) was conducted on selected samples using FEI Technai^{TM} operating at 200 kV. After mechanical grinding and polishing, electron transparent 3

mm diameter discs from weld nugget and base material were prepared using a Gatan ion polishing system. Differential scanning calorimetry (DSC) was also performed to analyze precipitation sequence and behavior in various samples. Netzsch 204 F1 Phoenix® was used to perform DSC with a heating rate of 10°C per minute.

3.4 Results and Discussion

3.4.1 FSW and Temperature Measurement

Macroscopically, both welds were defect-free. Investigation using optical microscope was conducted to verify the integrity of welds. Figure 3.2 shows an optical micrograph of cross section of W2. Typically, FSW of aluminum alloys results in the formation of distinct microstructural zones such as weld nugget (WN), thermo-mechanically affected zone (TMAZ), and heat affected zone (HAZ) as shown in Figure 3.2.

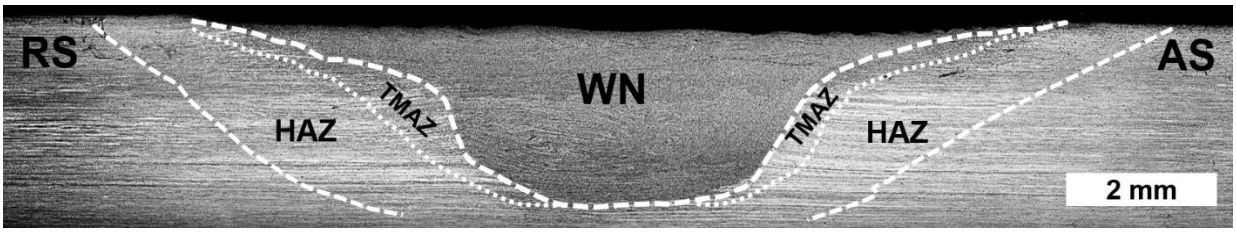

Figure 3.2 Optical macrograph of cross section of weld 2 showing various metallurgical zones evolved during FSW.

FSW is a thermo-mechanical process in which evolved temperatures are high enough to solutionize aluminum alloys [15,18]. During cooling, depending on cooling rates, solutes can be locked into solid solution or precipitate out as high temperature precipitates (or intermetallics) or may migrate to grain boundaries. Thus, the cooling rate after welding is critical to produce supersaturated solid solution with higher solute content. With this aim, external cooling mediums were used in W2. The temperature at the tool center during the entire welding process was measured and is shown in Figure 3.3. The time-temperature plot shows clearly that using copper

backing and water cooling behind the tool in W2 produced lower temperature throughout the welding process. Inset of Figure 3.3 focuses on the difference in temperature evolution in W1 and W2 during tool traverse. The temperature for W1 plateaued after quickly reaching a peak value of 470°C, which is a typical temperature produced in FSW of aluminum alloys [14,18]. The peak temperature in W2 increased from 447°C at the beginning of the weld to 455°C towards the end of the weld. The small increase in temperature could have been due to the reduced cooling effect of the roller as water evaporated. The use of copper backing and water cooling behind the tool resulted in lowering the peak temperature by 20°C; likely continued use of copper backing would have facilitated a higher cooling rate after welding in the case of W2.

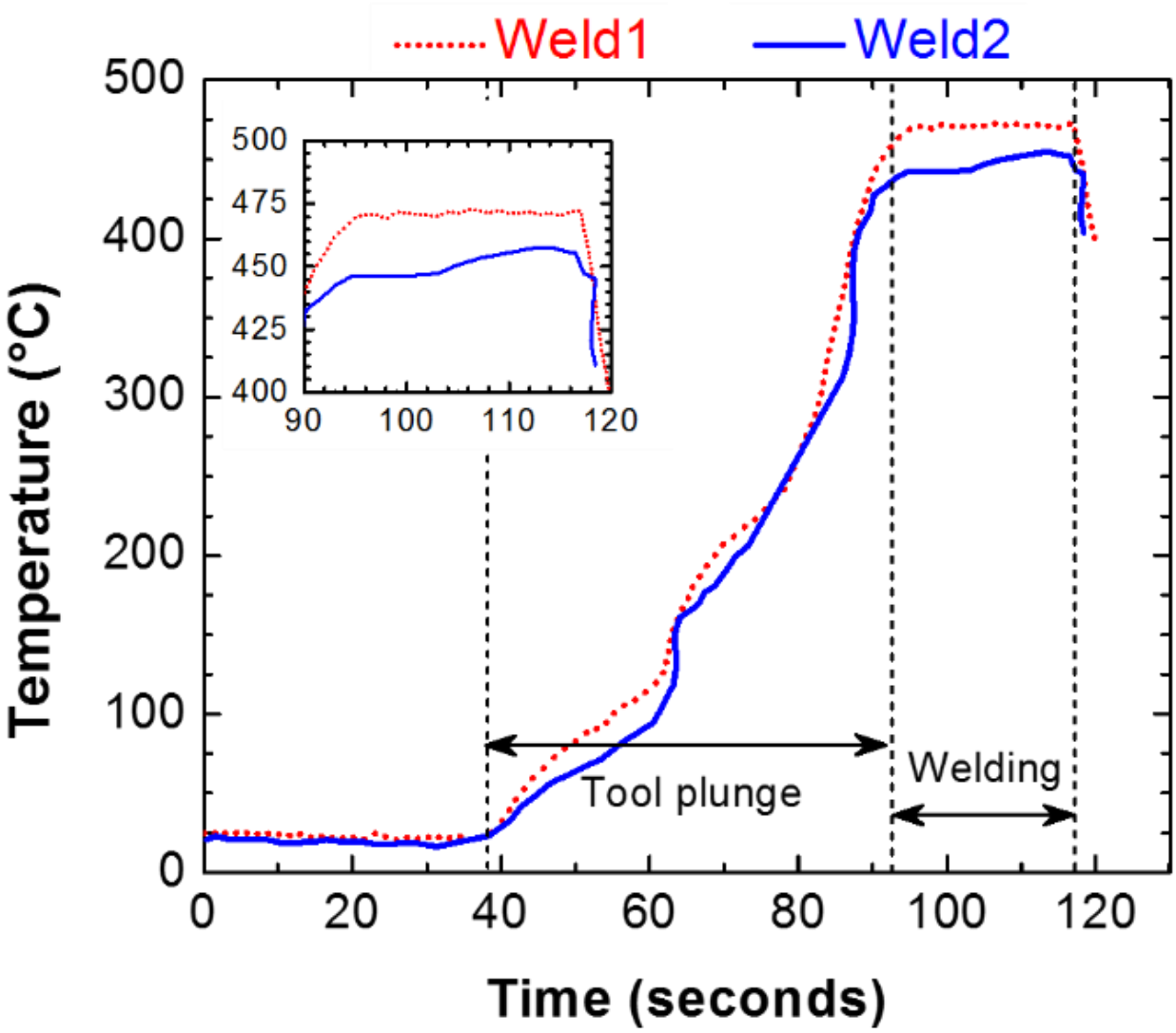

Figure 3.3 Temperature profile for both welds during plunging of tool and welding. Inset of the replotted temperature curves shows the temperature during tool traverse.

Vickers Microhardness Mapping

Figure 3.4 shows the maps of Vickers microhardness measurements taken across the weld cross section for both welds in as-welded and PWHT conditions. Hardness measurements of both welds in as-welded condition showed the presence of HAZ in which hardness dropped to 90-100 HV from a base material hardness of 130 HV. The hardness knockdown in HAZ is believed to be due to dissolution and/or coarsening of precipitates as a result of heat generated

during welding, which is a typical observation in FSW of precipitation-strengthened aluminum alloys [19]. The effect of external cooling used in W2 is clearly evident from hardness maps of W1 and W2 in as-welded condition. The width of HAZ in W2 was narrower compared to W1. This narrowing can be attributed to the reduced extent of dissolution and/or coarsening of precipitates due to enhanced cooling provided by the external cooling mediums. Generally, HAZ of FSW of peak aged precipitation-strengthened aluminum alloys shows a negative response to PWHT [14,19]. A further drop in hardness of HAZ occurs due to coarsening of precipitates already present in the matrix [14,19]. HAZ of both W1 and W2 showed a positive response to PWHT. Hardness in HAZ improved almost to the level of the base material for both welds. Knockdown of hardness in HAZ in as-welded condition and full recovery of hardness in HAZ after PWHT indicates that the majority of HAZ region did not experience any significant coarsening, and dissolution of precipitates might have occurred. This attribute would be further discussed in conjunction with results from other characterization techniques. Hardness in the weld nugget in as-welded condition for both welds was around 95-105 HV. FSW of precipitation strengthened aluminum alloys produces solutionized and recrystallized WN [14,19] and results in decreased hardness as compared to the base material. After PWHT, hardness in WN of both the welds recovered and was higher than the base material by 7-11 HV. Hardness in the WN of W2 after PWHT was a little higher than W1. This is due to higher solute retention in solid solution as external cooling provided higher cooling rate in WN of W2.

3.4.2 Tensile Testing

Uniaxial tensile testing with a minimum of 3 samples for every condition was carried out according to ASTM E8 standard. Average yield strength (YS), ultimate tensile strength (UTS), and total elongation of base material were 354 MPa, 522 MPa, and 9.9 %, respectively. Results

of tensile tests are shown in Table 3.2. Figure 3.5 shows engineering stress-strain curves for selected samples from BM, W1, and W2. Figure 3.5 and Table 3.2 show that tensile testing results displayed trends similar to hardness measurements. After PWHT, W2 showed higher strength recovery compared to W1. Higher cooling used in W2 would have resulted in higher solute content in solid solution during cooling of WN. Higher solute content in solution enhances precipitation during PWHT and resulted in higher strength recovery. Joint efficiency (JE) of all the samples was calculated to evaluate joint strength compared with the base material. W2 after PWHT showed high JE of 97% based on YS. W1 after PWHT achieved a JE of 89%, which clearly indicates the effect of different thermal experience of both welds.

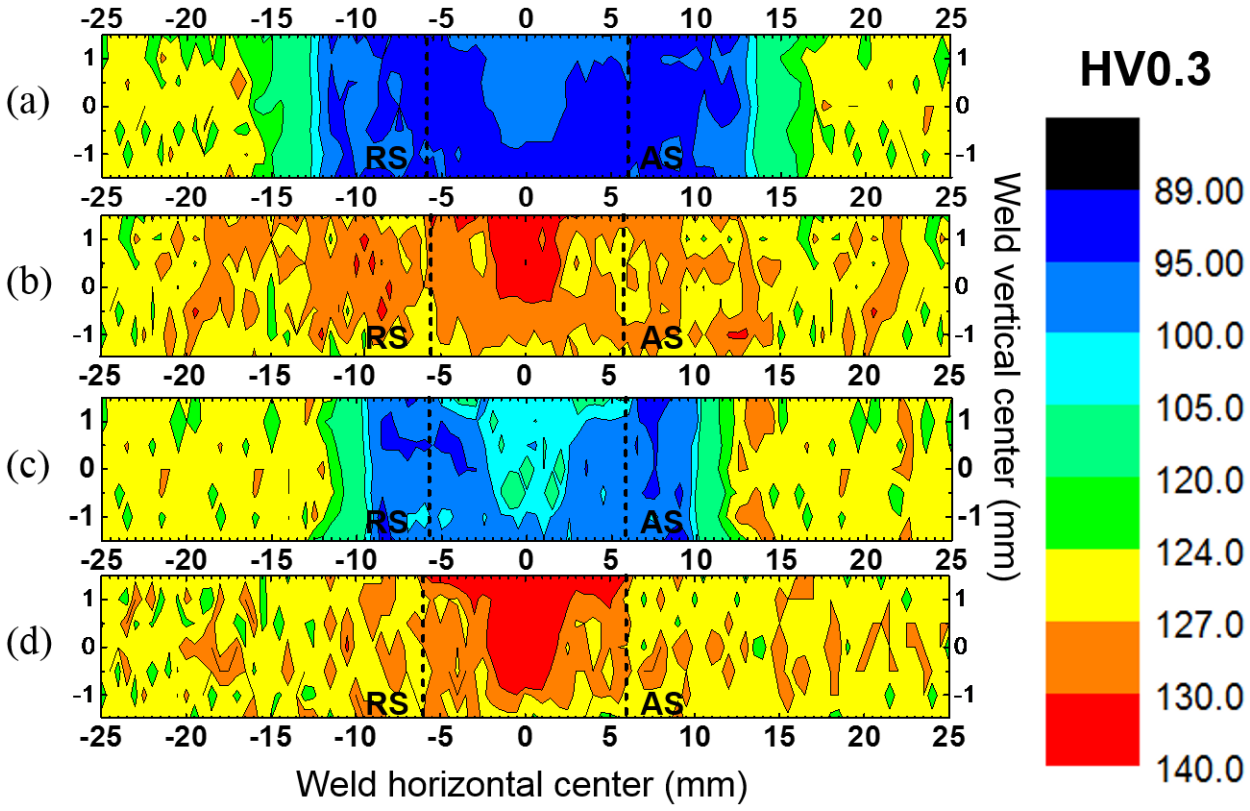

Figure 3.4 Microhardness map of weld cross section of (a) weld 1 in as-welded condition, (b) weld 1 in PWHT condition, (c) weld 2 in as-welded condition, and (d) weld 2 in PWHT condition.

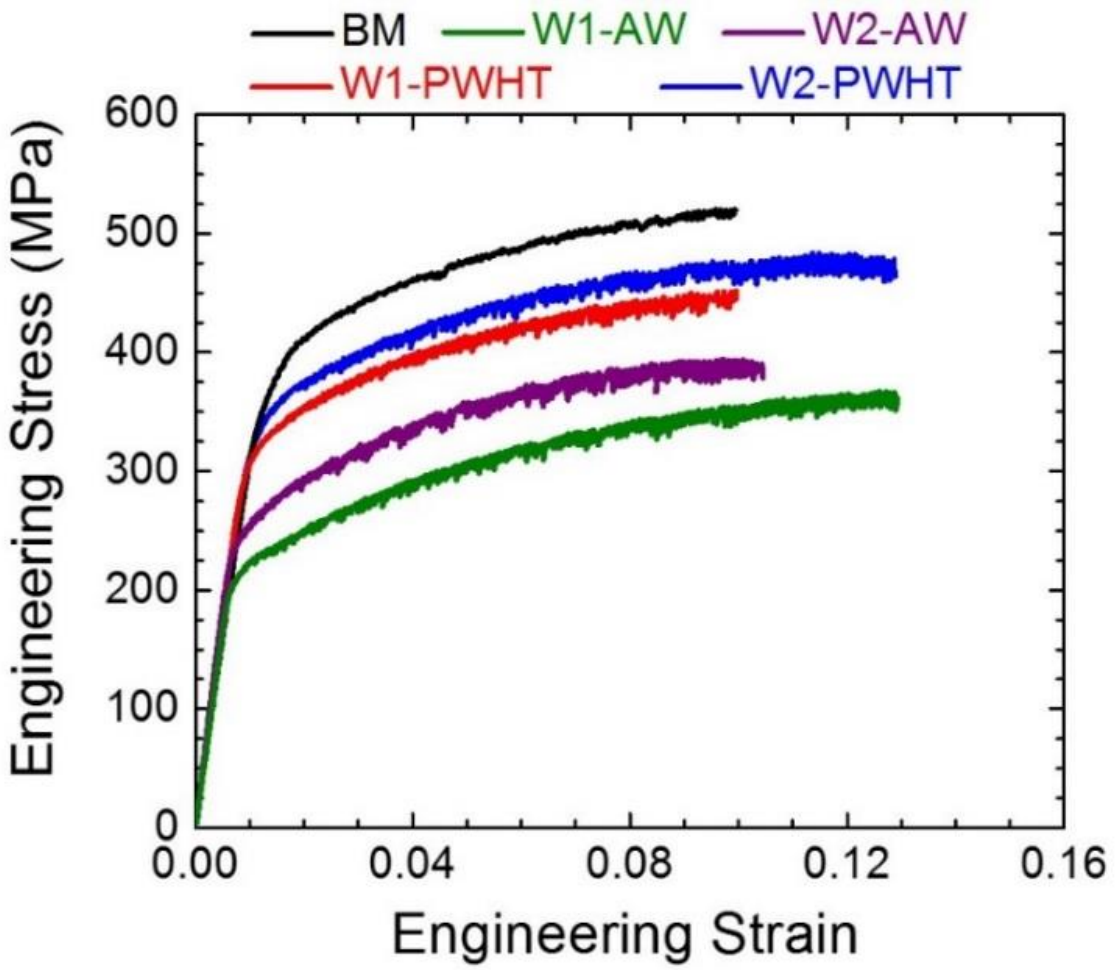

Figure 3.5 Engineering stress strain curves of BM and samples from welds in AW and PWHT condition.

Table 3.2 ASTM standard tensile test results of samples fromW1, W2, and BM. Three specimens were tested for each condition.

Specimen	YS (MPa)	UTS (MPa)	Total elongation (%)	Joint Efficiency	
				YS	UTS
BM	354.8±7.9	522.7±2.1	9.9±0.1	--	--
W1-AW	215.9±2.0	374.9±2.9	14.4±1.1	61%	72 %
W1-PWHT	315.5±2.3	449.3±4.9	9.4±0.5	89 %	86 %
W2-AW	241.3±4.1	395.1±0.5	10.8±0.5	68 %	76 %
W2-PWHT	344.4±12.1	480.1±2.1	11.7±1.6	97 %	92 %

3.4.3 Thermal and Microstructural Analyses

DSC of samples from WN of W1 and W2 in as-welded condition and BM in peak aged condition were carried out. The results of DSC are shown in Figure 3.6. Peak A in all three samples is likely to be due to dissolution of domains of ordered solid solution formed during natural aging [12]. Peak B represents dissolution of δ′ precipitate and it was observed at 180°C only in the base material sample. δ′ precipitate is the main strengthening phase in Al-Mg-Li alloys [9]. The absence of peak B in W1 and W2 samples shows that δ′ precipitates were not formed during cooling of the weld. Peak D is the ultimate endothermic peak which shows dissolution of high temperature precipitates (S_1). Peak C is the only precipitation peak observed in the DSC results of all samples. The precipitation peak area for W1 and W2 sample was significantly larger as compared to that of the BM sample. Peak C was slightly larger for W2 compared to W1. Also, a shift in the precipitation peak among all three samples was noticed. The precipitation peak of W2 formed at 255°C, which was lower than that of W1 (280°C). A shift of the precipitation peak in aluminum alloys towards lower temperature indicates faster aging kinetics [12,25]. The amount of solute available in solid solution can dictate the aging kinetics as well as the area associated with the peak. An additional effect can be the presence of larger retained dislocation density, which would also enhance precipitation kinetics. A higher solute level in solid solution would result in enhanced precipitation. Therefore, based on the FSW temperature, hardness, and DSC results, use of external cooling medium in W2 can be deduced to result in a higher solute content in solid solution in WN compared to W1. As a response, W2 showed higher strength recovery after PWHT.

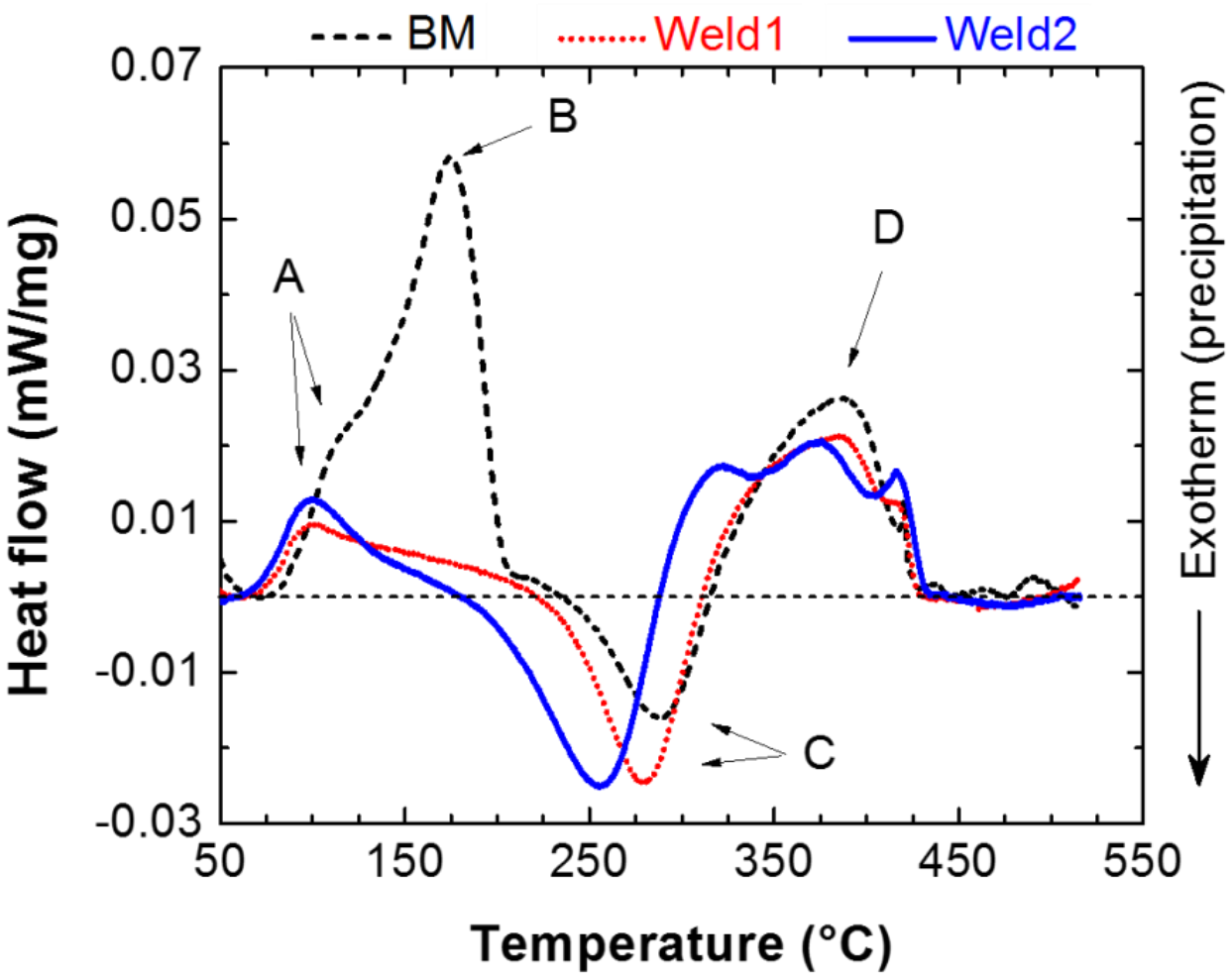

Figure 3.6 DSC heat flow results for samples from BM in peak aged condition and WN of both welds in as-welded condition.

TEM investigation of selected samples was also carried out for microstructural characterization. Figure 3.7a shows high density of δ' precipitates in the BM sample. δ' has very low interfacial energy and thus homogenously precipitates in a spherical form in the matrix [11]. Core-shell type $Al_3(Li,Zr)$ dispersoid in which δ' is believed to precipitate around Al_3Zr was also observed in BM [11]. Few grain boundary and quenched-in precipitates were also observed in BM. TEM images of samples from WN of W1 and W2 are shown in Figure 3.8. A high density of δ' precipitates was observed in both W1 and W2 samples. Determining the size distribution of precipitates was difficult because of very high volume fraction and overlapping of precipitates in

TEM images. However, the size of precipitates was manually calculated by analyzing TEM images. The size of δ' precipitate was in the range of 10-30 nm for all samples. Although accurate calculation of the size distribution was difficult, generally, precipitate size in W1 sample was larger compared to W2 and BM. A high degree of grain boundary precipitation was observed in W1 sample, as shown in Figure 3.8a-b; whereas the extent of grain boundary precipitation was much less in W2. W2 exhibited microstructure similar to that of BM with high density of very fine δ' precipitates. Interestingly, coarsened Al_3(Li,Zr) dispersoid (>50 nm) was also seen in W1 (Figure 3.8b),which was not observed in W2 or BM.

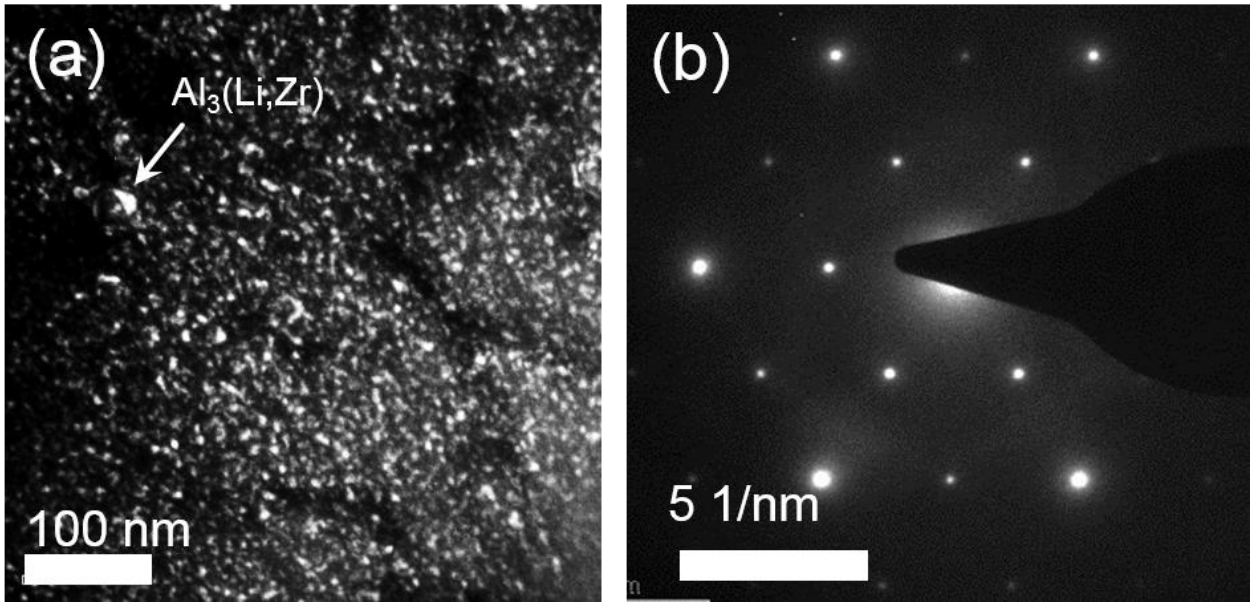

Figure 3.7(a) Dark field TEM image along [111] of BM 1424 and (b) corresponding SADP of area in (a).

TEM results indicate that extensive formation of grain boundary precipitates in W1 compared to W2 is due to low cooling rates associated with W1. Low undercooling or larger residence time at higher temperature associated with W1 led to solute migration to grain boundaries, which favored grain boundary precipitation; whereas external cooling provided in W2 led to higher solute availability for solid solution strengthening and dense precipitation of

fine δ'. Extensive grain boundary precipitation in W1 resulted in lower joint strength as compared to W2.

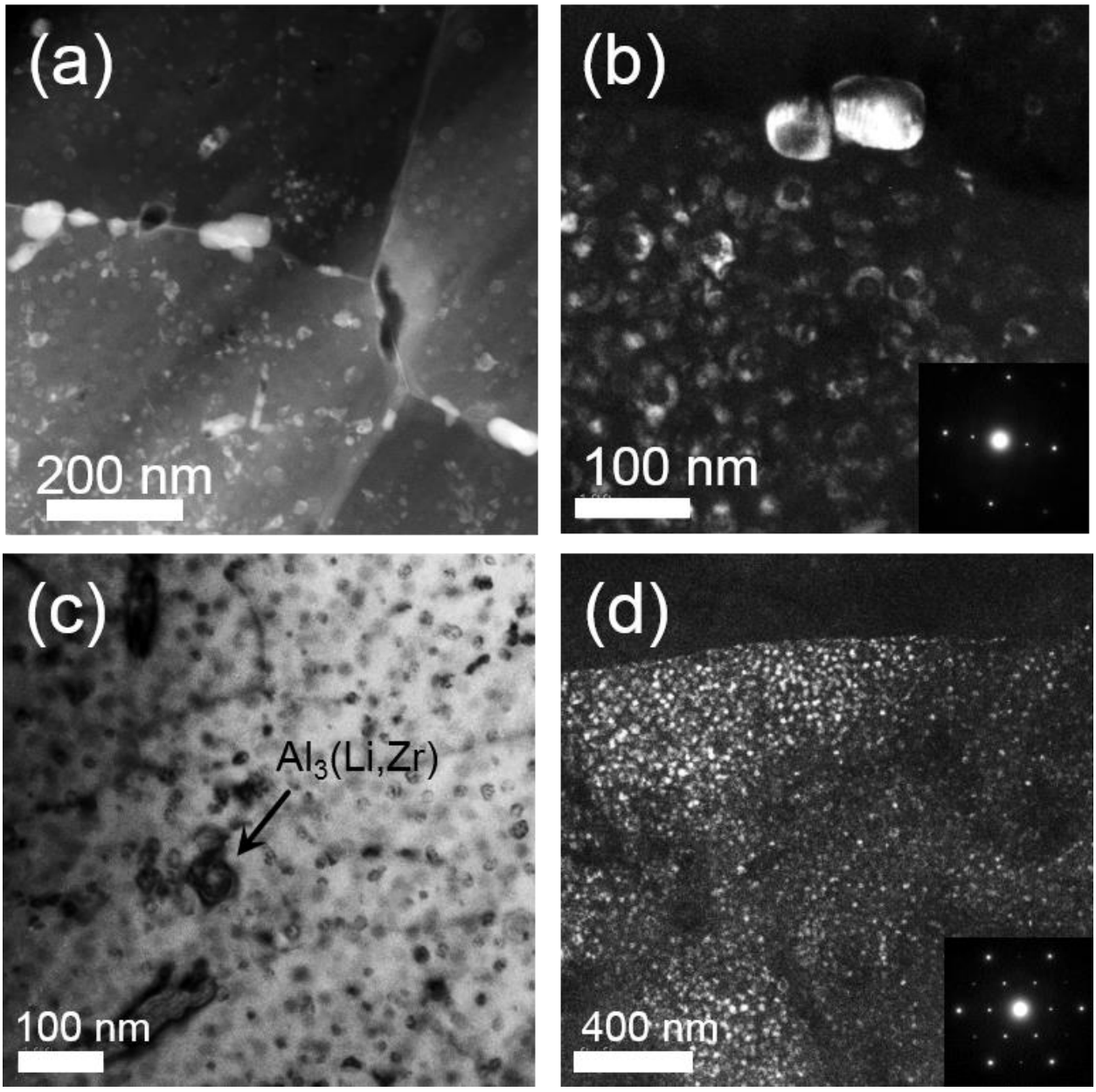

Figure 3.8(a) TEM image of WN of W1 taken in scanning mode, (b) dark field TEM image of WN of W1 with corresponding SADP in inset, (c) bright field TEM image of WN of W2, and (d) dark field TEM image of WN of W2 with SADP of same area shown in inset.

In this study, critical results such as the positive response of HAZ to PWHT and high

strength recovery in WN are contrary to typical cases of FSW of precipitation strengthened aluminum alloys [19,20]. Typically, FSW of precipitation strengthened aluminum alloys (2XXX and 7XXX series) results in knockdown of hardness in HAZ and WN. Temperature evolved in HAZ during FSW lies in 200-350°C [26]. In FSW of 2XXX and 7XXX alloys, loss of strength in HAZ occurs due to coarsening of precipitates occurring at high temperatures [14,18,26]. Also, 2XXX and 7XXX alloys possess complex multi-precipitate microstructure, and coarsening occurs very rapidly in HAZ. Even welds made at high speeds experience some level of property degradation in HAZ which, subsequently, shows a negative response to PWHT [26]. However, in the present study temperatures reached in HAZ were enough to dissolve δ′ precipitates. Alloy 1424 consists mainly of δ′ precipitate, whereas other phases such as S_1 have sluggish kinetics and precipitates after long aging hours [11,12]. Also, δ′ precipitate has very low interfacial energy and precipitates easily and homogenously throughout the matrix [11]. Thus, δ′ re-precipitates readily in HAZ upon exposure to PWHT. This explains the positive response of as-welded samples to PWHT.

FSW of aluminum results in recrystallized microstructure in WN [14]. Dislocation density decreases in WN. Precipitation of strengthening precipitates in 2XXX and 7XXX alloys are generally favored by the presence of dislocations [27]. Low dislocation density in WN results in sluggish precipitation kinetics in WN of FSWed 2XXX and 7XXX aluminum alloys [28]. Therefore, strength recovery in WN of FSWed 2XXX and 7XXX alloys is generally low. In the present study, full recovery of strength was observed in WN. As discussed before, δ′ precipitate has very low coherency strains and precipitates homogenously. This explains the high density of δ′ precipitation observed in WN after PWHT, which led to near base material strength.

3.5 Conclusion

In the present study, FSW was used to evaluate and understand the weldability of an Al-Mg-Li alloy, 1424. External cooling mediums were used to understand the effect of thermal history on final weld properties. The key outcomes are:

1. FSW resulted in dissolution of precipitates in WN and HAZ. Use of external cooling mediums led to narrower HAZ.
2. After PWHT, a high level of strength recovery was observed in both WN and HAZ. Hardness in WN was higher than base material.
3. Based on yield strength, high joint efficiency of 97% of base material was achieved for the weld with external cooling and high conductivity backing plate.
4. No knockdown in strength in HAZ after PWHT was observed, which is contrary to the case of FSW of other precipitation strengthened aluminum alloys. This was attributed to the nature of δ′ precipitate in 1424 alloy. Homogeneous re-precipitation of δ′ due to its low interfacial energy was ascertained to account for full recovery in HAZ.
5. Similarly, fine and dense precipitation of δ′ precipitate led to full recovery of strength in WN.

Acknowledgments

This work was supported under the NSF-IUCRC grant for Friction Stir Processing (NSF-IIP 1157754). The additional support of Boeing, General Motors, Pacific Northwest National Laboratory, Army Research Laboratory and Rolls-Royce Corporation for the UNT site is acknowledged. This report was prepared as an account of work sponsored by an agency of the US Government. The views and opinions of the authors expressed herein do not necessarily state or reflect those of the US Government or any agency thereof. We also acknowledge the UNT Center for Advanced Research and Technology (CART).

3.6 References

[1] Prasad NE, Gokhale A, Wanhill R. Aluminum-Lithium Alloys: Processing, Properties, and Applications. : Butterworth-Heinemann, 2013.

[2] Williams JC, Starke EA. Progress in structural materials for aerospace systems. Acta Materialia 2003;51:5775-99.

[3] Prasad NE, Gokhale A, Rao PR. Mechanical behaviour of aluminium-lithium alloys. Sadhana 2003;28:209-46.

[4] Rioja RJ, Liu J. The evolution of Al-Li base products for aerospace and space applications. Metallurgical and Materials Transactions A 2012;43:3325-37.

[5] Lequeu P, Smith KP, Daniélou A. Aluminum-Copper-Lithium Alloy 2050 Developed for Medium to Thick Plate Journal of Materials Engineering and Performance 2009; 2010;19:841-847.

[6] Khokhlatova L, Kolobnev N, Oglodkov M, Mikhaylov E. Aluminum-lithium alloys for aircraft building. Metallurgist 2012;56:336-41.

[7] Fridlyander I, Khokhlatova L, Kolobnev N, Rendiks K, Tempus G. Thermally stable aluminum-lithium alloy 1424 for application in welded fuselage. Metal science and heat treatment 2002;44:3-8.

[8] Lenczowski B. New lightweight alloys for welded aircraft structure. 2002:4101.1,4101.4.

[9] Martin JW. Aluminum-lithium alloys. Annual Review of Materials Science 1988;18:101-19.

[10] Noble B, Thompson G. Precipitation characteristics of aluminium-lithium alloys. Metal Science Journal 1971;5:114-20.

[11] Deschamps A, Sigli C, Mourey T, De Geuser F, Lefebvre W, Davo B. Experimental and modelling assessment of precipitation kinetics in an Al–Li–Mg alloy. Acta Materialia 2012;60:1917-28.

[12] Davydov V, Ber L, Kaputkin EY, Komov V, Ukolova O, Lukina E. TTP and TTT diagrams for quench sensitivity and ageing of 1424 alloy. Materials Science and Engineering: A 2000;280:76-82.

[13] Thomas W, Nicholas E, Needham J, Murch M, Templesmith P, Dawes C. International patent application no 1991.

[14] Mishra RS, Ma Z. Friction stir welding and processing. Materials Science and Engineering: R: Reports 2005;50:1-78.

[15] Mishra RS, Mahoney MW. Friction Stir Welding and Processing. : ASM International, 2007.

[16] Threadgill P, Leonard A, Shercliff H, Withers P. Friction stir welding of aluminium alloys. International Materials Reviews 2009;54:49-93.

[17] Mishra RS, De PS, Kumar N. Fundamentals of the Friction Stir Process.: Springer, 2014.

[18] Çam G, Mistikoglu S. Recent developments in friction stir welding of Al-alloys. Journal of Materials Engineering and Performance 2014;23:1936-53.

[19] De PS, Mishra RS. Friction stir welding of precipitation strengthened aluminium alloys: scope and challenges Science and Technology of Welding and Joining 2011;16:343-347.

[20] Wei S, Hao C, Chen J. Study of friction stir welding of 01420 aluminum–lithium alloy. Materials Science and Engineering: A 2007;452:170-7.

[21] Cui L, Li X, He D, Chen L, Gong S. Effect of Nd: YAG laser welding on microstructure and hardness of an Al–Li based alloy. Mater Charact 2012;71:95-102.

[22] Peng Y, Fu Z, Wang W, Zhang J, Wang Y, Wang H et al. Phase transformation at the interface during joining of an Al–Mg–Li alloy by pulsed current heating. Scr Mater 2008;58:49-52.

[23] Shi Y, Zhong F, Li X, Gong S, Chen L. Effect of laser beam welding on tear toughness of a 1420 aluminum alloy thin sheet. Materials Science and Engineering: A 2007;465:153-9.

[24] Kostrivas A, Lippold J. Weldability of Li-bearing aluminium alloys. International materials reviews 1999;44:217-37.

[25] Starink M. Analysis of aluminium based alloys by calorimetry: quantitative analysis of reactions and reaction kinetics. International Materials Reviews 2004;49:191-226.

[26] Reynolds AP, Tang W, Khandkar Z, Khan JA, Lindner K. Relationships between weld parameters, hardness distribution and temperature history in alloy 7050 friction stir welds. Science and Technology of Welding and Joining 2005;10:190-9.

[27] Cassada W, Shiflet G, Starke E. The effect of plastic deformation on Al2CuLi (T 1) precipitation. Metallurgical Transactions A 1991;22:299-306.

[28] Malard B, De Geuser F, Deschamps A. Microstructure distribution in an AA2050 T34 friction stir weld and its evolution during post-welding heat treatment. Acta Materialia 2015;101:90-100.

CHAPTER 4

PAPER III: AGING KINETICS OF FRICTION STIR WELDED Al-Cu-Li-Mg-Ag AND Al-Cu-Li-Mg ALLOYS[2]

4.1 Abstract

Friction stir welding using tool rotation rate of 800 revolutions per minute and welding speed of 200 millimeters per minute was carried out on 2195,2098, and 2199 Al-Li alloys of third generation. Post weld heat treatment for various number of hours was conducted to study the effect of alloy chemistry on aging kinetics in various metallurgical zones developed during welding. Vickers microhardness, differential scanning calorimetry, and transmission electron microscopy results showed that low dislocation density after recrystallization in weld nugget results in delayed aging kinetics. Ag containing alloy showed faster aging response compared to Ag-free alloy. Coarse precipitates at grain boundary and in the grain interior were found responsible for loss of non-recoverable strength in heat affected zone for all the alloys.
Keywords: Friction stir welding; Al-Li alloys; differential scanning calorimetry; aging kinetics.

4.2 Introduction

There is a high demand of light weight structural alloys, especially in aerospace industry. Lithium, the lightest metallic element, addition offers weight saving advantages in aluminum based alloys. Addition of each 1% lithium in aluminum based alloy, reduces the density by 3% and increases the elastic modulus by 6% [1-3]. Al-Li alloys offers high strength levels which are comparable to that of 7XXX high strength aluminum alloys [4-6]. Third generation Al-Li alloys are alloyed with other elements such as Cu, Mg, and Ag. T1 (Al_2CuLi) precpitate is the main

[2] Parts of this chapter have been previously published, either in part or full, from Harpreet Sidhar, Rajiv S. Mishra, Aging kinetics of friction stir welded Al-Cu-Li-Mg-Ag and Al-Cu-Li-Mg alloys, Materials & Design, Volume 110, 15 November 2016, Pages 60-71. Reproduced with permission from Elsevier.

strengthening phase in Al-Cu-Li alloys [1,3,7-10]. θ' (Al_2Cu) and δ' (Al_3Li) precipitates of Al-Li and Al-Cu binary system also forms in Al-Cu-Li alloys [11,12]. Ag is added to enhance the precipitation of T1 phase [11-13]. There are numerous industrial applications of Al-Cu-Li-X alloys such as Airbus A380 (2196 alloy), F16 aircraft (2297), Boeing 787 dreamliner (2099/2199) [12].

Invented in 1991 [14], friction stir welding (FSW) is an innovative, environment-friendly and energy-efficient process which has evolved as favorable joining process for welding Al-Li alloys [5,15-17]. It eliminates the welding defects caused by melting and solidification in conventional welding techniques [15-18]. However, similar to other precipitation strengthened (2XXX or 7XXX) aluminum alloys, welding of Al-Li results in loss of strength in different locations in weld zone [15,16,19]. Relative proportion of alloying elements can impact the microstructural evolution in these zones during FSW and post weld heat treatment (PWHT).

Thus, effect of alloy chemistry on aging kinetics of various zones developed during FSW in three different Al-Li alloys have been studied using various experimental techniques such as hardness measurements, differential scanning calorimetry (DSC), and transmission electron microscopy (TEM).

4.3 Materials and Methods

4.3.1 Friction Stir Welding and Temperature Measurements

Commercially available Al-Cu-Li alloys 2195, 2098, and 2199 in peak aged condition (T8 temper) were used in this study. Alloy chemistry of each alloy used is presented in Table 4.1. FSW was conducted for all three alloys. Tool rotation rate of 800 revolutions per minute and welding speed of 200 millimeters per minute were used as the welding parameters. For each alloy, two types of welds were made. First, using regular welding bed as backing and ambience

as the cooling medium. For second type of weld, under-water welding was carried out. A pool of water was created on the top of plate being welded. Schematic of welding setup used in second type of weld (will be called UWFSW hereafter) is shown in Figure 4.1a. Tool used in FSW was made of hardened H13 tool steel. It consisted of 3.5 mm long step-spiral conical pin of diameter 7.8 mm at the root, tapering down to 5.4 mm and a shoulder of diameter 16 mm. Temperature evolving at the center of the tool pin was also recorded for all the welds. Schematic of location of thermocouple inserted in tool and image of actual tool used is shown in Figure 4.1b.

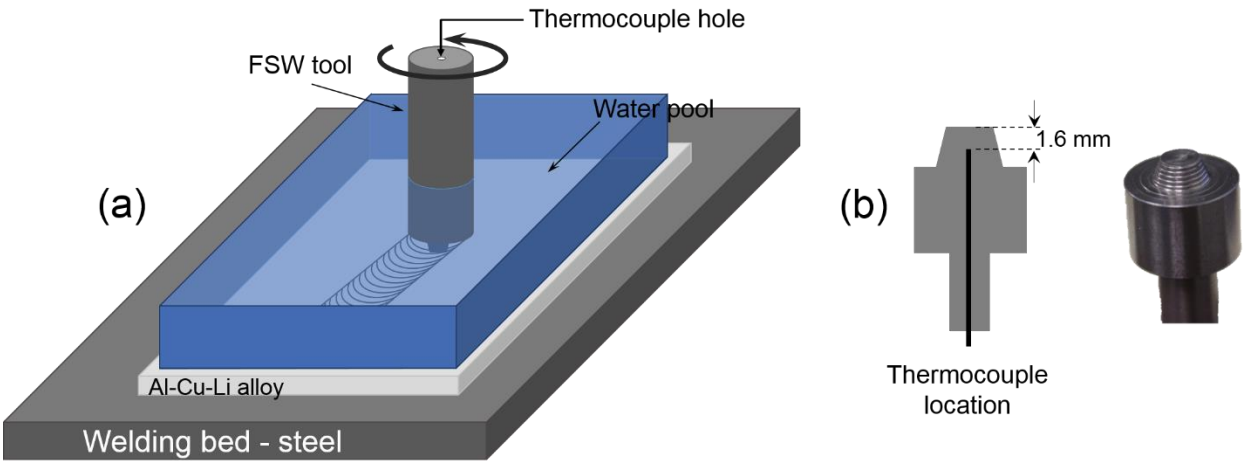

Figure 4.1 Schematic of welding setup used in UWFSW and (b) schematic of thermocouple location inside the tool with an image of actual tool used in all the welds.

Table 4.1 Nominal compositional limits of alloying elements in alloy 2195, 2098, and 2199.

Alloy	Li	Cu	Mg	Ag	Mn	Zr	Zn
2195	0.8-1.2	3.7-4.3	0.25-0.8	0.25-0.6	0.25	0.08-0.16	0.25
2098	0.8-1.3	3.2-3.8	0.25-0.8	0.25-0.6	0.35	0.04-0.18	0.35
2199	1.4-1.8	2.3-2.9	0.05-0.4	-	0.10-0.50	0.05-0.12	0.20-0.9

4.3.2 Micro-hardness Measurements and Microstructural Evaluation

Micro-hardness measurements and microstructural evaluation was conducted for both welds in as welded and different post weld heat treated (PWHT) conditions. PWHT was carried out in a forced air oven at 160°C for various number of hours. Vickers micro-hardness measurements were taken across the weld cross-section at the mid plane of the weld using 300g load (HV0.3) on Wilson Tukon 1202 hardness tester.

Differential scanning calorimetry (DSC) was performed on location specific samples from different welds. Netzsch 204 F1 Phoenix® was used to perform DSC with a heating rate of 10°C per minute. Transmission electron microscopy (TEM) was conducted using FEI Technai™ operating at 200kV. Electron transparent 3 mm diameter discs from region of interest were prepared using Gatan ion polishing system.

4.4 Results and Discussion

4.4.1 Temperature Evolution During FSW and UWFSW

Understandably, FSW of all the three alloys resulted in higher peak temperature as compared to UWFSW. Temperature evolved during welding for all the six welds made is shown in Figure 4.2. Temperature during the tool traverse (welding temperature) is also shown as inset in Figure 4.2 for each case. Peak temperature during FSW of 2098 varied around 520°C. In UWFSW of 2098, due to the external cooling provided, the peak temperature reduced to around 455°C (Figure 4.2a). FSW of alloy 2195, which probably has similar mechanical and thermo-physical properties as that of alloy 2098 due to similar alloy chemistry, the peak welding temperature varied around 505-515°C. Similarly, peak temperature during UWFSW of 2195 was around 455°C which was quite similar to that of 2098 (Figure 4.2b). Alloy 2199 has slightly different alloy chemistry compared to 2195 and 2098 with relatively lower Cu content and higher Li content in 2199. Peak temperature during FSW of 2199 was around 530°C and it reduced and

varied around 480°C in case of UWFSW of 2199. It should be noted that higher peak temperature during UWFSW of 2199 as compared to UWFSW of 2098 and 2195 is only an experimental variation due to the loss of water from pool during welding of 2199.

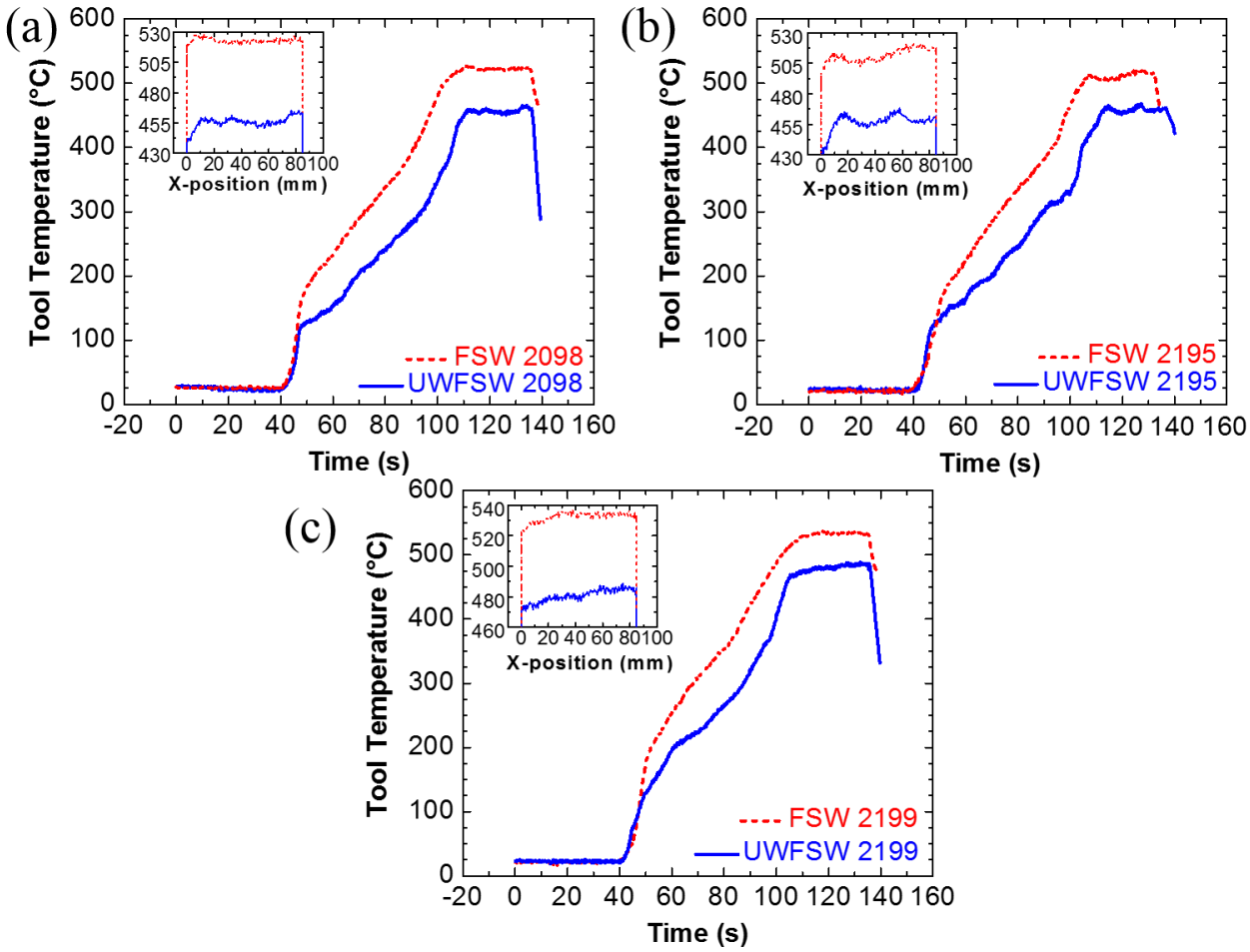

Figure 4.2 Temperature evolved at the center of tool during FSW and UFSW of (a) alloy 2098, (b) alloy 2195, and (c) alloy 2199. Temperature during tool traverse is also shown as inset for each case.

4.4.2 Macroscopic Microstructural Investigation

Macroscopic investigation of polished cross section, etched with Keller's reagent, of samples from FSW and UWFSW of all the welds was conducted. Figure 4.3 show the optical macrographs of weld cross section of both the welds of alloy 2199. The effect of use of water

pool cooling was evident as can be seen in Figure 4.3. In case of UWFSW, the width of TMAZ was observed to be significantly reduced whereas the WN was noted to be slightly wider as compared to FSW sample as shown in Figure 4.3. Similar attributes were also observed in all other welds. Also, it is apprehensible that width of HAZ will also be strict in UWFSW as compared to that in FSW.

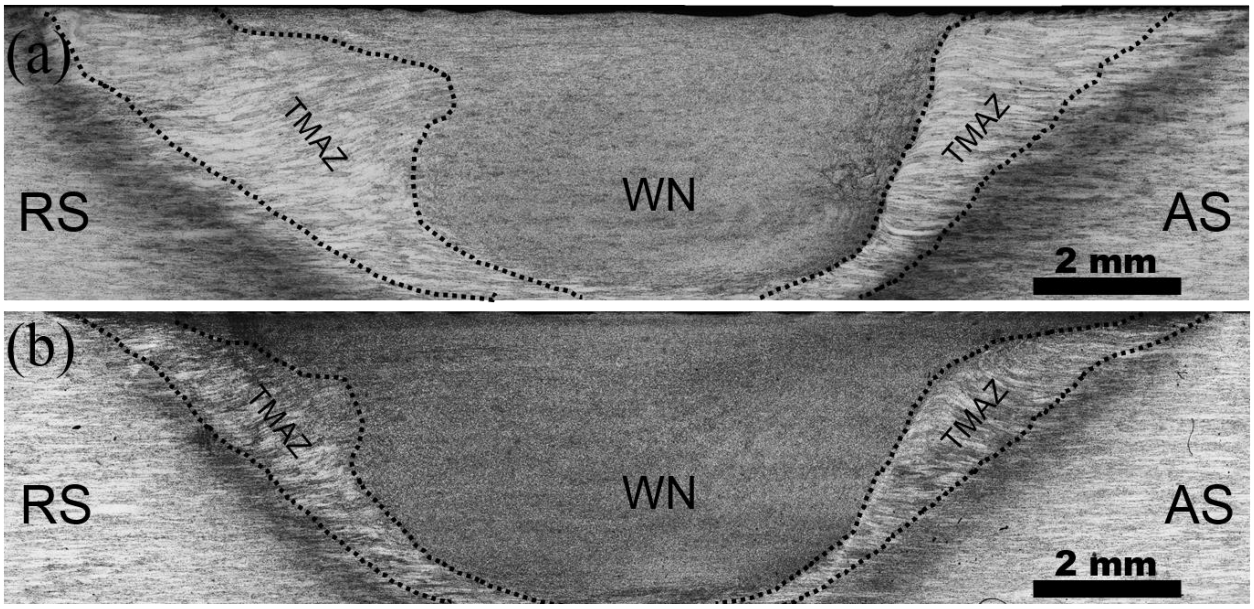

Figure 4.3 Macrograph of weld cross section of (a) FSW of 2199 and (b) UWFSW of 2199.

4.4.3 Vickers Microhardness Measurements

FSW of aluminum alloys results in significant changes in microstructure. Precipitate density and distribution is also affected by the thermal and deformation effects of FSW. Samples from all the welds were subjected to PWHT of 160°C for various number of hours to study the aging kinetics of various precipitates in three different alloys subjected to FSW. Vickers microhardness results of samples from all the welds in AW condition and aged condition are shown in Figure 4.4.

4.4.3.1 FSW and UWFSW of Alloy 2098 and 2195

In AW condition, both FSW and UWFSW of alloy 2098 resulted in nearly flat hardness

profile in WN with a hardness varying around 115 HV (Figure 4.4a and b). The hardness in TMAZ (in both FSW and UWFSW) was also observed to be similar to WN hardness. HAZ hardness was 4-5 HV less than that of WN in case of UWFSW, whereas it was similar to WN in case of FSW of 2098. The hardness profile of sample from FSW and UWFSW of alloy 2195 in AW condition (Figure 4.4c and d) was similar to the case of alloy 2098. This could be due to very similar alloy chemistry of alloy 2098 and 2195 except slightly lower Cu content in 2098. The width of the low hardness region in AW condition was slightly lesser in UWFSW as compared to FSW of both 2098 and 2195. After being subjected to PWHT at 160°C for 16 hours, FSW and UWFSW of 2098 showed similar improvement in hardness in WN. Whereas, TMAZ and HAZ showed different levels of hardness recovery. UWFSW showed harness recovery of around 20 HV in TMAZ and HAZ whereas it was around 10 HV increase in the case of FSW of 2098. Based on the DSC results, PWHT were conducted for longer hours. Overall, improvement in hardness was observed throughout the weld cross-section after 30 hours and 65 hours of aging for FSW and UWFSW of 2195 and 2098. PWHT for 100 hours did not show any improvement after 65 hours aging results in hardness in any case. It was probably due to the fact that 100 hours of aging at 160°C falls under over-aging regime of alloy 2098 and 2195.

4.4.3.2 FSW and UWFSW of Alloy 2199

FSW and UWFSW hardness results of alloy 2199 (Figure 4.4e and f) were quite different from results of 2098 and 2195. In AW condition, hardness profile in WN, TMAZ, and HAZ of UWFSW sample was nearly flat and varied around 90 HV. In case of FSW, hardness in WN and HAZ was observed to be around 90 HV but TMAZ showed higher hardness of around 105 HV. The higher hardness in TMAZ could be due to re-precipitation during cooling of weld. Although trends in hardness recovery in both FSW and UWFSW of 2199 were observed, but response to

aging treatment was observed to be sluggish as compared to alloy 2195 and 2098. Hardness in WN of sample from FSW and UWFSW showed no or very low recovery after 16 hours and 30 hours of aging. After 65 hours of aging at 160°C an improvement of around 20 HV was observed in both FSW and UWFSW. Unlike the case of 2098 and 2195, aging for 100 hours also showed improvement in hardness. It was evident that aging kinetics in alloy 2199 were sluggish as compared to other alloys which had shown signs of over-aging after 100 hours of aging. A wider TMAZ observed in FSW as compared to UWFSW (Figure 4.3) was also evident in hardness after aging for various number of hours. Overall, HAZ showed higher recovery in case of UWFSW as compared to FSW in all the cases which is due to the cooling provided by the water pool.

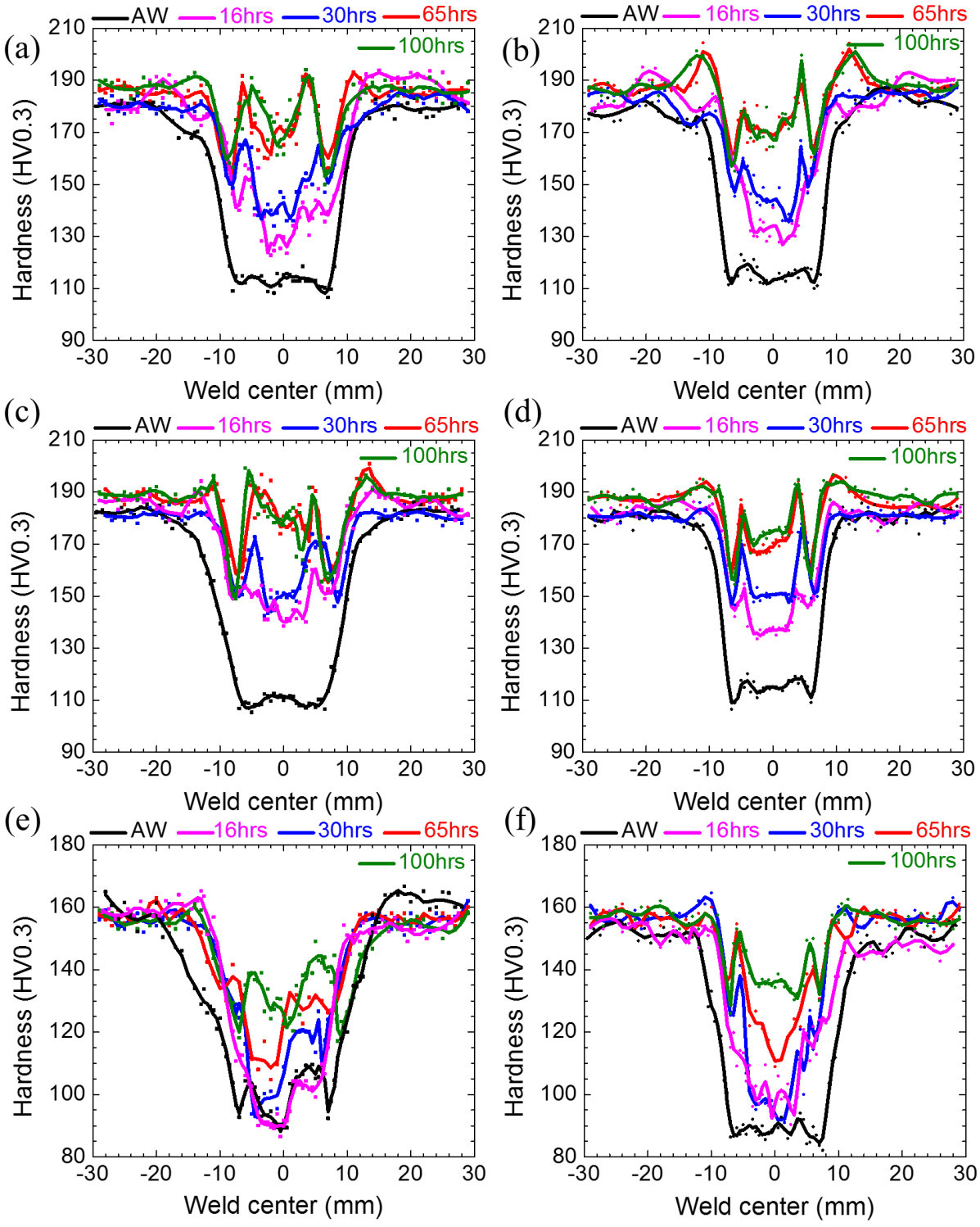

Figure 4.4 Results of Vickers microhardness measurements of samples of (a) FSW of 2098 ,(b) UWFSW of 2098 ,(c) FSW of 2195 ,(d) UWFSW of 2195 ,(e) FSW of 2199 , and (f) UWFSW of 2199 aged at 160°C for various number of hours.

4.4.4 DSC and TEM

DSC is a powerful technique to study the precipitation sequence and kinetics in aluminum alloys and it has been used quite extensively in the past [8,20-24]. Generally, in DSC results precipitation of second phases is identified by exothermic heat flow and endothermic reactions are due to dissolution of phases [20,25]. Area under the peak or amplitude of the peak dictates the intensity of the precipitation or dissolution event. To compare the effect of water cooling, DSC results of samples from WN of FSW and UWFSW of 2098 in AW condition and 16 hours aged condition compared with 2098 BM are shown Figure 4.5a. Several endothermic and exothermic events which are common to Al-Cu-Li system were identified. Endothermic peak labelled as A is due to dissolution of GP zones formed due to natural aging in samples in AW condition. Peak B is due to dissolution of metastable δ′ (Al_3Li) precipitate. Major exothermic peak C is due to precipitation of T1 (Al_2CuLi) phase. Whereas peak D is a large endothermic peak is the dissolution event of T1 and other high temperature phase formed. Less than 1% Li content in third generation Al-Cu-Li alloys suppresses the formation of δ′ precipitate and thus, very small amount of δ′ dissolution was observed in 16 hours aged and 2098 BM samples. T1 precipitation peak was observed to be larger for UWFSW sample as compared to FSW in AW condition which is due to higher solute retention in solid solution due to large undercooling in case of UWFSW. Though samples aged for 16 hours showed quite similar precipitation and dissolution behavior in DSC results. Hardness results also showed similar trends after 16 hours of aging. Thus, it can be assumed that due to slow welding speed (8 IPM) there were insignificant differences between WN of UWFSW and FSW. Figure 4.5b shows the DSC results samples from WN of FSW of 2195 in various conditions. The reduction in intensity of peak B with increase in aging time shows that quantity of Al_3Li precipitate also reduced

during longer aging hours. After 16 hours of aging at 160°C, which leads to peak strength in Al-Cu-Li alloys, the amplitude of peak C showed that at the end of aging treatment there is significant amount of solute available in solid solution to precipitate out as T1 phase. This result lead to aging treatment for longer hours. Understandably, T1 precipitation reduces with longer aging hours. Another peak labelled as C1, convoluted with peak C, evolved in results of aged samples. This peak signifies the thickening (coarsening) of T1 plates during aging. Peak C1 evolves with longer aging time and completely replaces the peak C in case of sample aged for 100 hours (Figure 4.5b). Also, peak B for sample aged for 100 hours was observed to be shifted to higher temperature which indicates that average size of Al_3Li precipitate was significantly larger as a result of coarsening. It is in complete accordance with the hardness results that 100 hours of aging for FSW of 2195 is in over-aging regime. Similarly, peak C1 was observed in samples from HAZ of FSW of 2195 in various conditions as shown in Figure 4.5c. Interestingly, peak C1 was also observed in AW condition of HAZ which indicates that significant coarsening events takes place in HAZ during FSW.

DSC results of samples of WN of FSW of 2199 compared to 2199 BM sample are shown in Figure 4.5d. It clearly evident that peak A and B are significantly larger as compared to the case of alloy 2098 and 2195. Alloy 2199 contains higher Li and lower Cu content as compared to 2098 and 2195 and thus forms Al_3Li precipitate in significantly larger amount resulting in larger associated peaks. Interestingly, sample aged for 16 hours showed a shift in peak B towards higher temperature as compared to BM and peak C was slightly smaller as compared WN. It indicates that Al_3Li precipitation occurred with average size of precipitate larger than in BM and very low level of T1 precipitation occurred during 16 hours of aging. It shows that precipitation kinetics in alloy 2199 are extremely sluggish as compared alloy 2098 and 2195. Presence of peak

B and C even after aging of 100 hours shows that there is enough solute available in solid solution of WN for precipitation of Al_3Li and T1. Similar attributes were observed in hardness results of FSW of alloy 2199. Overall, shift of peak B and peak C towards higher temperature for samples from WN as compared to BM shows that FSW resulted in delayed precipitation and larger average size of precipitates in WN.

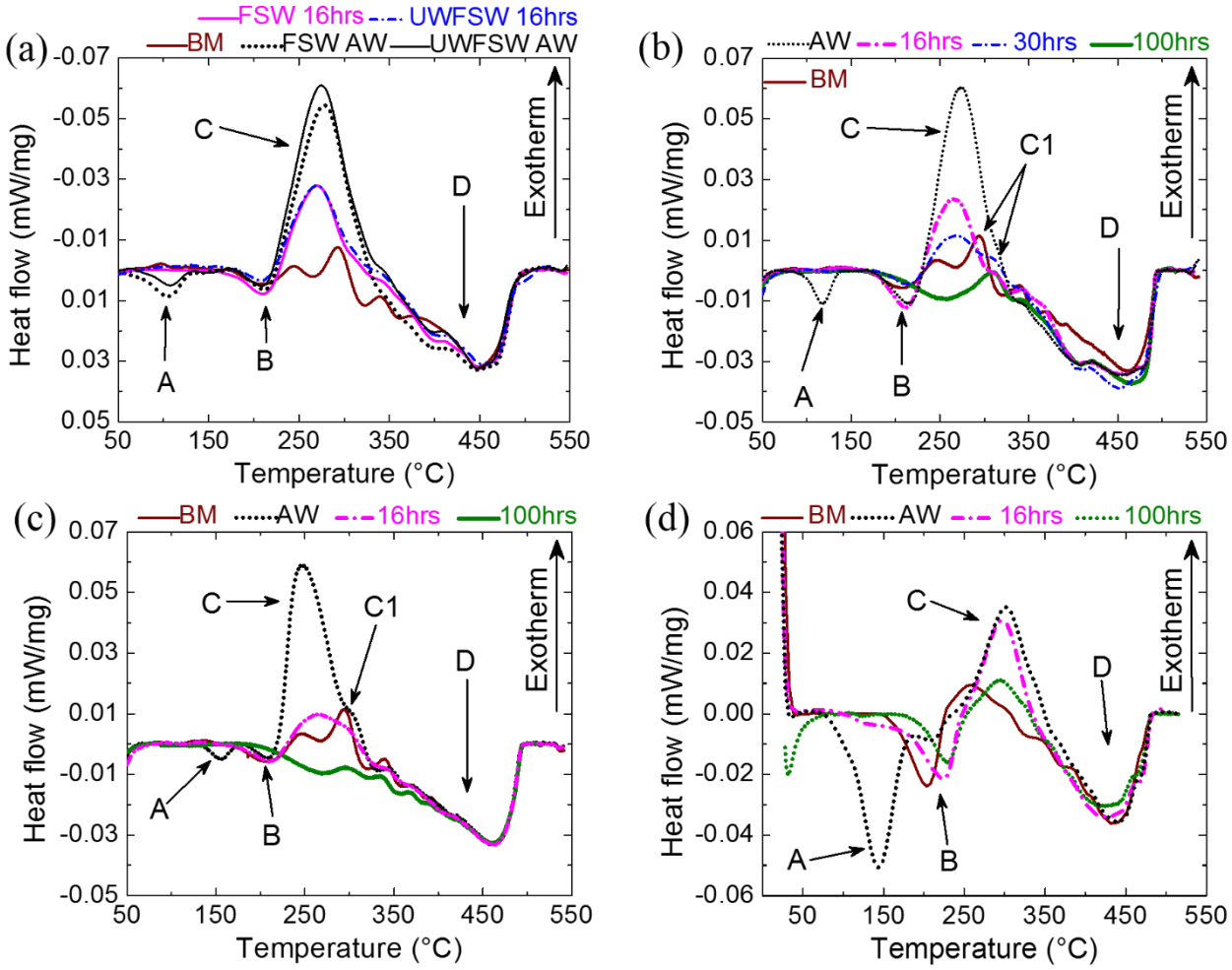

Figure 4.5 DSC results of samples taken from (a) WN of FSW and UWFSW of 2098 in AW and 16 hours aged condition compared to 2098 BM, (b) WN of FSW of 2195 aged for various number of hours compared to 2195 BM, (c) HAZ of FSW of 2195 aged for various number of hours compared to 2195 BM, and (d) WN of FSW of 2199 aged for various number of hours compared to 2199 BM.

Presence of heterogeneous nucleation sites such vacancies and dislocations are known to enhance the kinetics of precipitation in Al-Cu-Li alloys [7]. Dislocations reduces the strain energy associated with the precipitate matrix interface of T1 precipitate and promotes nucleation and growth [7]. Low dislocation density in recrystallized WN [15]reduces the kinetics of nucleation and growth of T1 precipitate. Also, addition of Ag promotes T1 precipitation [13]. Ag segregation reduces the misfit energy between matrix and precipitate interface [13]. Ag also promotes the nucleation and growth of T1 in presence of Mg by retarding formation of GP zones [13]. Thus, absence of dislocations delays the aging kinetics in WN of 2195 and 2199 alloys, whereas absence of both dislocations and Ag further delays the precipitation of T1 precipitates.

TEM studies were conducted to evaluate the type of precipitates formed as a result of FSW and subsequent aging treatments. TEM images of BM of 2195 and 2199 are shown in Figure 4.6. Bright field images of BM of 2195 and 2199 shows the presence of T1 precipitates, the main strengthening phase in third generation Al-Cu-Li alloys. Selected area diffraction pattern (SADP) taken along [110] zone axis as shown in Figure 4.6b and d shows the presence of T1 in both 2195 and 2199 alloy. SADP also shows the presence of Al_3Li precipitate in both the alloys. It should be noted that higher intensity of Al_3Li spot in 2199 shows higher amount of Al_3Li in 2199 whereas according to intensity of SADP shows it was low in 2195 alloy. Similarly, from diffraction patterns, BF images, and DSC results it was clear that T1 density was higher in 2195 as compared to 2199 alloy. The average length of T1 precipitate in 2195 BM was around 120-150 nm, whereas it was around 80-100 nm in 2199 BM.

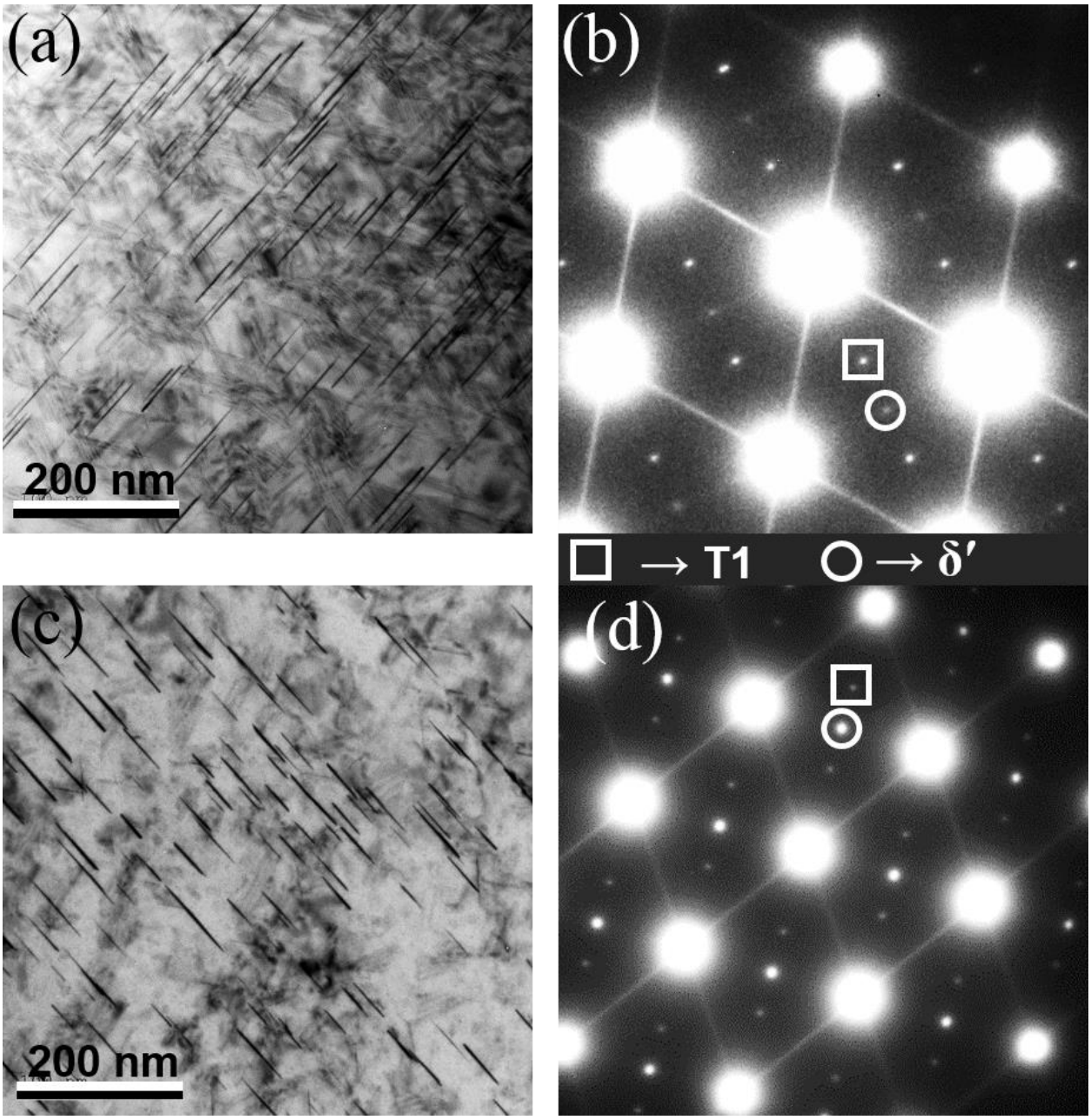

Figure 4.6 TEM image of (a) 2195 BM in BF mode, (b) SADP of area shown in (a), (c) 2199 BM in BF mode, and (d) SADP of area shown in (c).

Figure 4.7a and b show the BF TEM images of sample from UWFSW and FSW of 2199 respectively, in AW condition. It is clearly evident that WN of both UWFSW and FSW contained coarse grain boundary and grain interior precipitates. Also, overall dislocation density in WN of UWFSW of 2199 was observed to higher compared to relatively low dislocation

density grains in case of FSW. It is due to lower peak temperature and higher cooling rate during UWFSW. Heterogeneous nucleation sites such as dislocations favors precipitation of T1 phase and thus resulted in slightly higher hardness in WN of UWFSW after aging for 16 hours as compared to the case of FSW.

WN of FSW of 2199 did not show any improvement in hardness after aging of 16 hours. TEM studies revealed that dislocation density was quite low in WN of FSW (Figure 4.7b). After aging for 16 hours, very few T1 precipitates were observed at the sub-grain boundaries and dislocation structures as shown in Figure 4.7c and d (Note the overexposed intensity of matrix spots and very faint streaks corresponding to T1 precipitates in SADP in Figure 4.7d). Figure 4.7c and d also reveals that small amount of Al_3Li precipitates were formed during aging of 16 hours. This characteristic of very low level of response to aging for 16 hours was also evident in hardness and DSC results and thus can be concluded that 16 hours of aging is not sufficient for strength recovery in FSWed 2199 alloy.

Figure 4.8 show the TEM images of sample taken from WN of FSW of 2199 aged for 100 hours at 160°C. It is clearly evident from BF images and SADP that after 100 hours of aging, WN showed high density of T1 and δ′ precipitates. As seen in Figure 4.8c, the length of T1 precipitate was in 150-200 nm range. Precipitate free zone (PFZ) and precipitation of T1 on grain boundary was also observed (Figure 4.8e) as grain boundary acts a heterogeneous and favorable nucleation site by reducing the strain energy between T1 phase and matrix. Coarse grain boundary precipitates with size ranging in 0.5-1 μm were also observed (Figure 4.8f). These precipitates dissolve during welding and re-precipitates during cooling cycle of weld. PFZ around these coarse precipitates was also observed (Figure 4.8f).

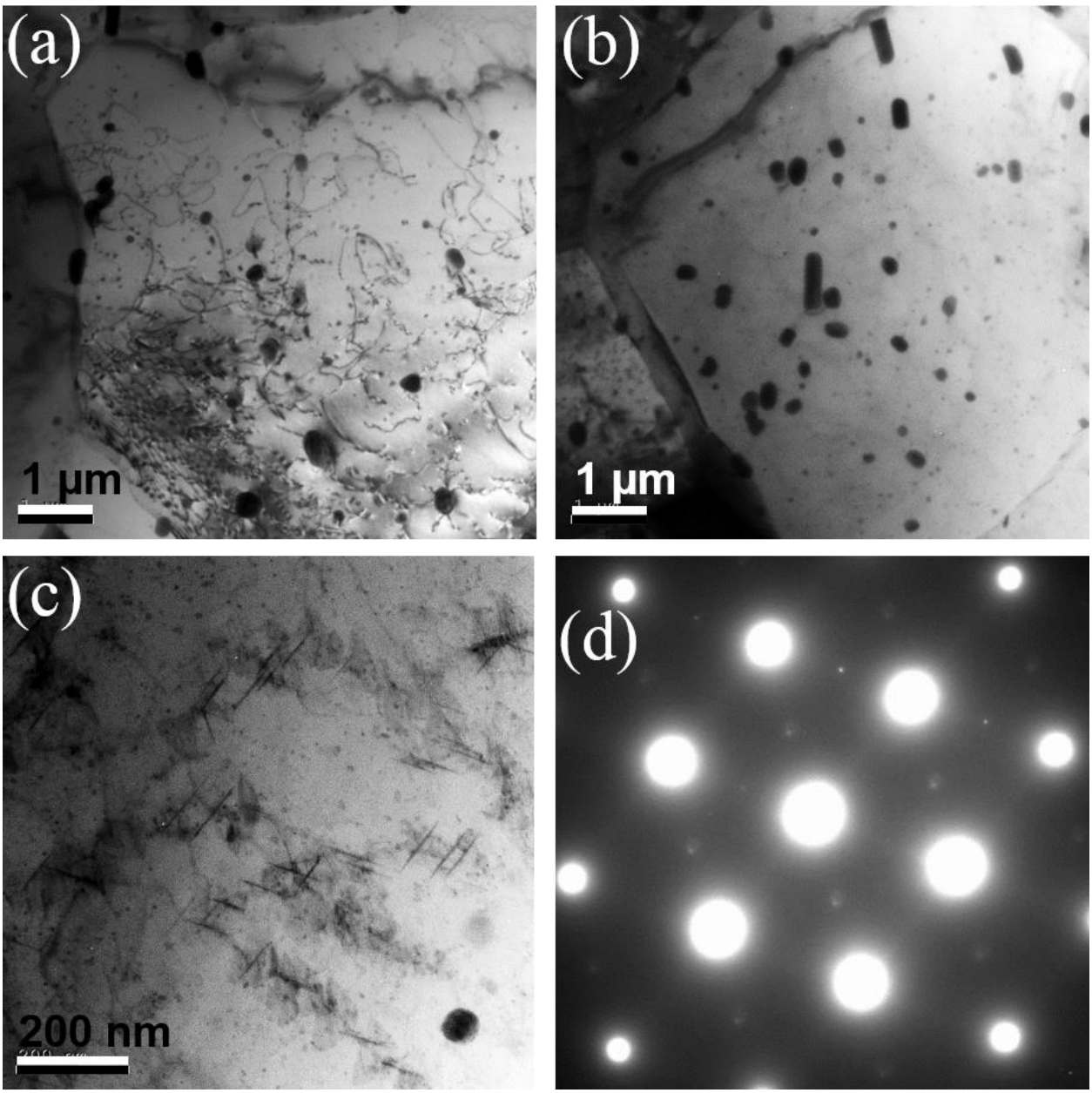

Figure 4.7 TEM images of (a) WN of UWFSW of 2199 in AW condition, (b) WN of FSW of 2199 in AW condition, (c) WN of FSW of 2199 in aged for 16 hours, and (d) SADP of area shown in (c).

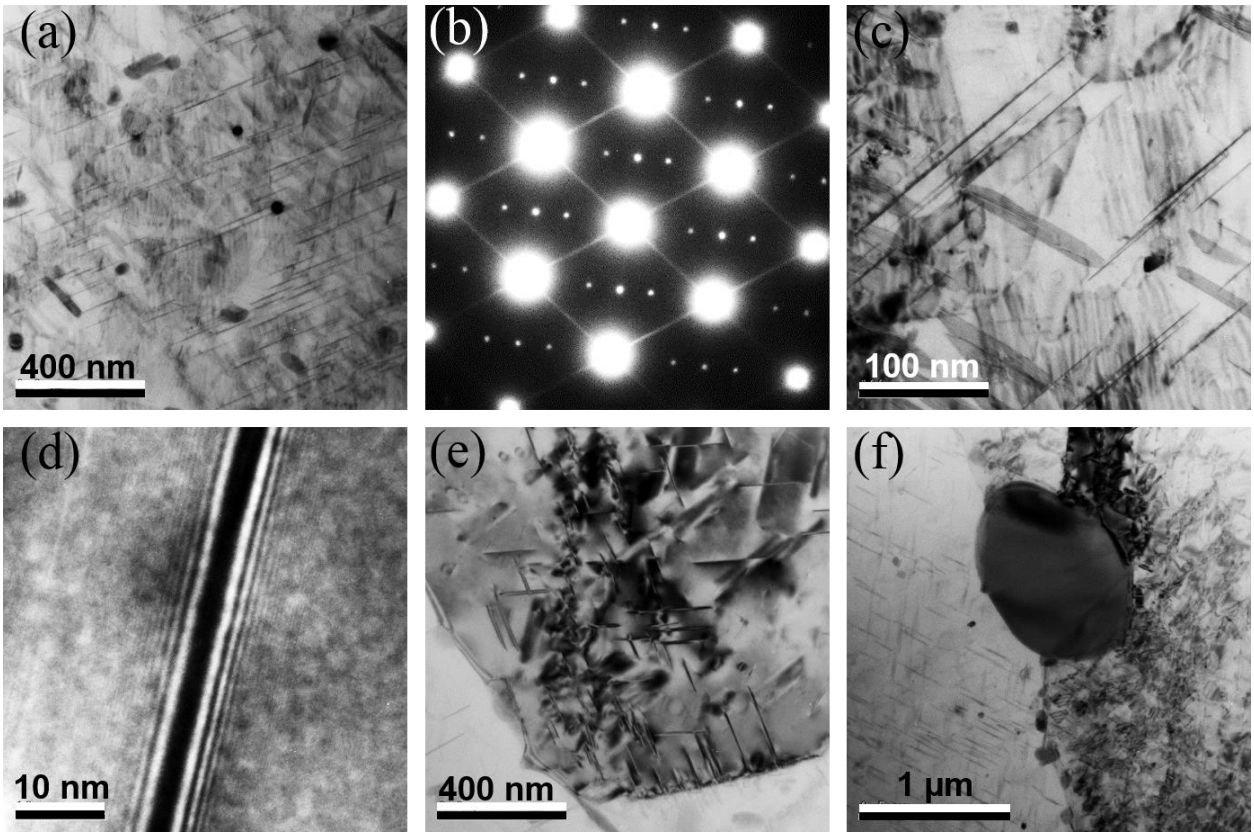

Figure 4.8 TEM images of (a) (c) (d) (e) (f) WN of FSW of 2199 after 100 hours of aging, and (b) SADP of area shown in (a).

Figure 4.9a shows the BF TEM image of WN of FSW of 2195 in AW condition. Clearly, the microstructure is similar to the case of 2199; low dislocation density, re-precipitated coarse precipitates in grain interior and grain boundary. Figure 4.9b-f show TEM images of WN of FSW of 2195 aged for 100 hours. Similar to the case of 2199, high density of T1 precipitates was observed. Though density of Al_3Li precipitates was very low which is due to low Li and higher Cu content in 2195 alloy. PFZ and coarse grain boundary precipitates were also observed.

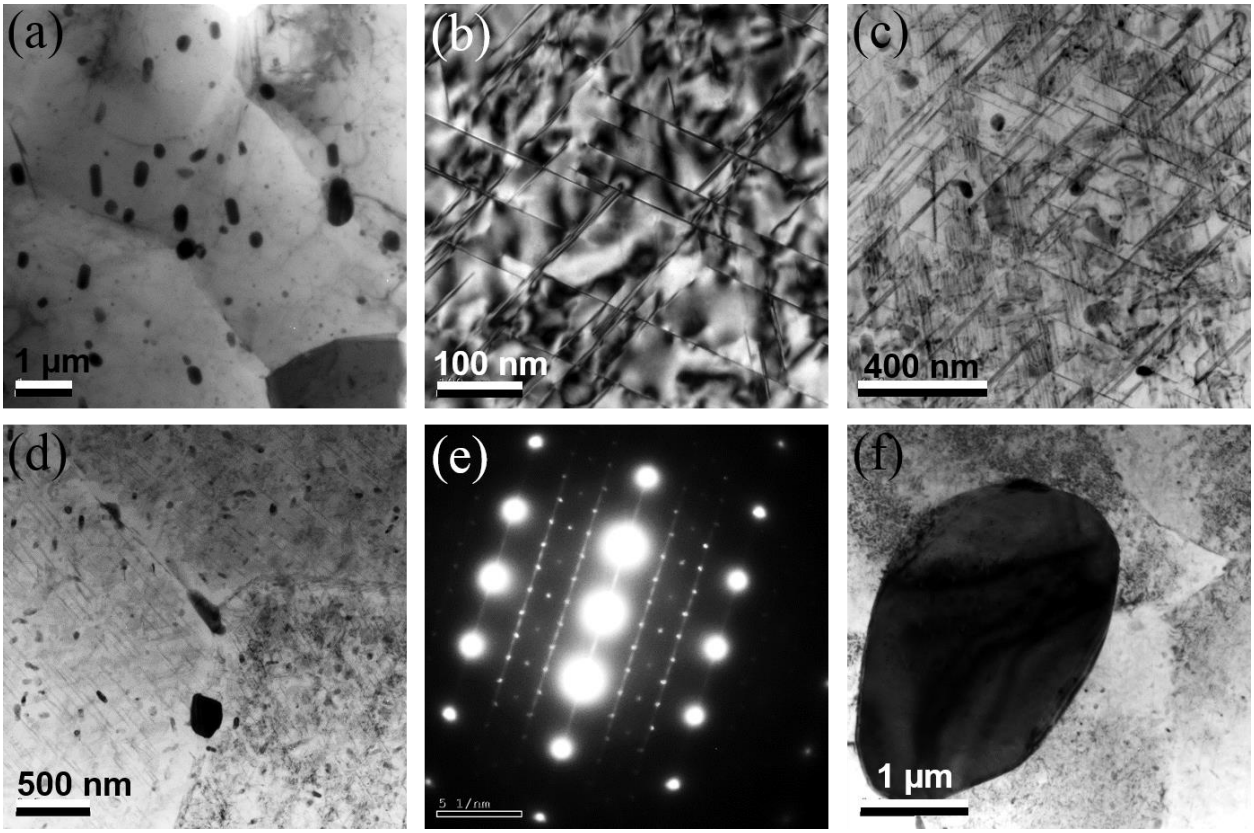

Figure 4.9 TEM image of (a) WN of FSW of 2195 in AW condition, (b) (c) (d) (f) WN of FSW of 2195 aged for 100 hours, and (e) SADP of one of the grains shown in (d).

In AW condition, HAZ of FSW 2199 showed low hardness similar to the WN hardness. Figure 4.10 shows that the reduction in hardness in HAZ is due to full dissolution of Al_3Li precipitate and partial dissolution of T1 precipitates. It is clear from SADP shown in Figure 4.10b. Also, BF images shows that density of T1 precipitates was also low in HAZ.

HAZ of FSW of 2199 after artificial aging for 100 hours resulted in high density of T1 and δ′ precipitates as shown in Figure 4.11. Although high density of precipitates was observed, but hardness in HAZ was still below the BM hardness. This is due to the solute loss to the grain boundary precipitates and coarsening of precipitates during FSW and aging treatment. Coarse grain boundary precipitates and PFZ as shown in Figure 4.11a were observed throughout the HAZ sample.

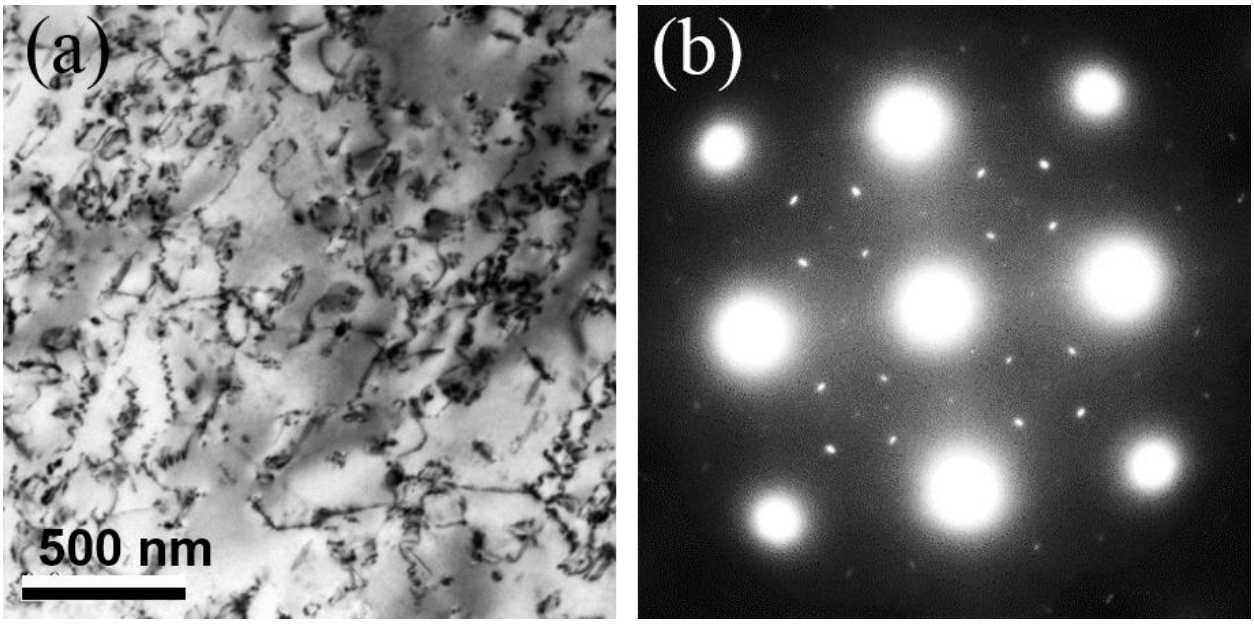

Figure 4.10 TEM image of (a) HAZ of FSW of 2199 in AW condition, and (b) SADP of area shown in (a).

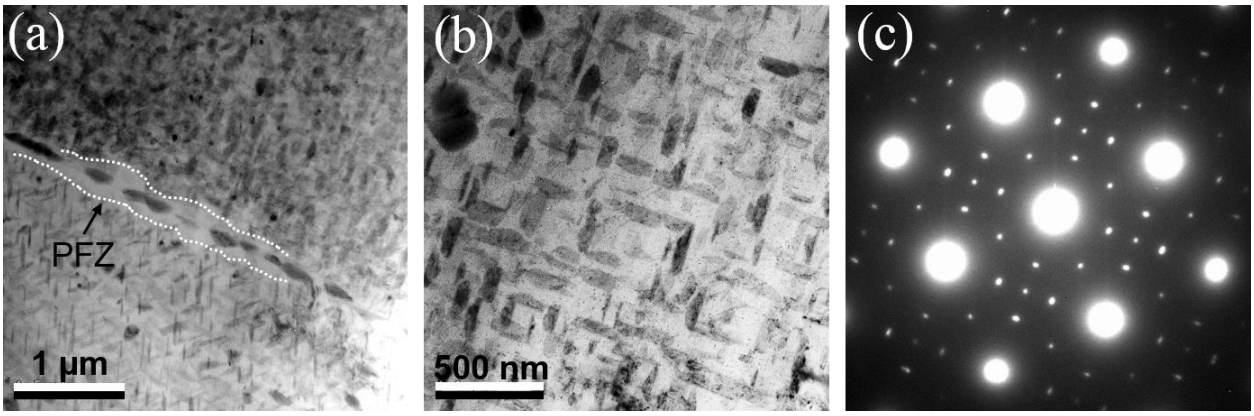

Figure 4.11 TEM image of (a) (b) HAZ of FSW of 2199 aged for 100 hours, and (c) SADP of area shown in (b).

HAZ of FSW of 2195 also showed partial dissolution and coarsening of precipitates in AW condition as shown in Figure 4.12. T1 precipitates aligned along the sub-grain boundary were observed (Figure 4.12d). PFZ around the coarse phases was also observed (Figure 4.12c).

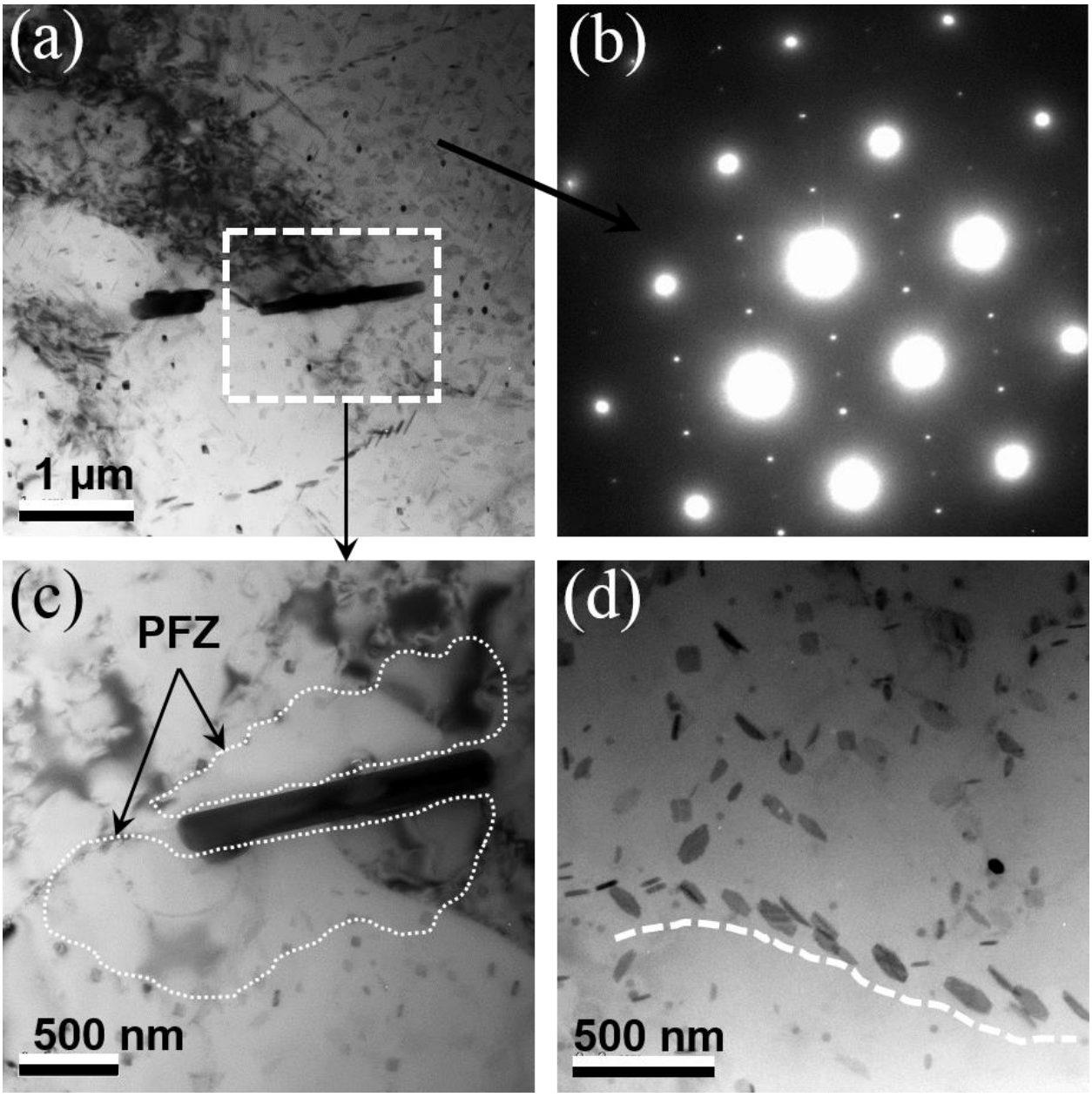

Figure 4.12 TEM image of (a) (c) (d) HAZ of FSW of 2195 in AW condition, (b) SADP of an area shown in (a).

Similar to the HAZ of FSW of 2199 aged for 100 hours, HAZ of FSW of 2195 also showed high density of precipitates (Figure 4.13). Also, PFZ and coarse grain boundary precipitates were observed which were responsible for knockdown in hardness in HAZ.

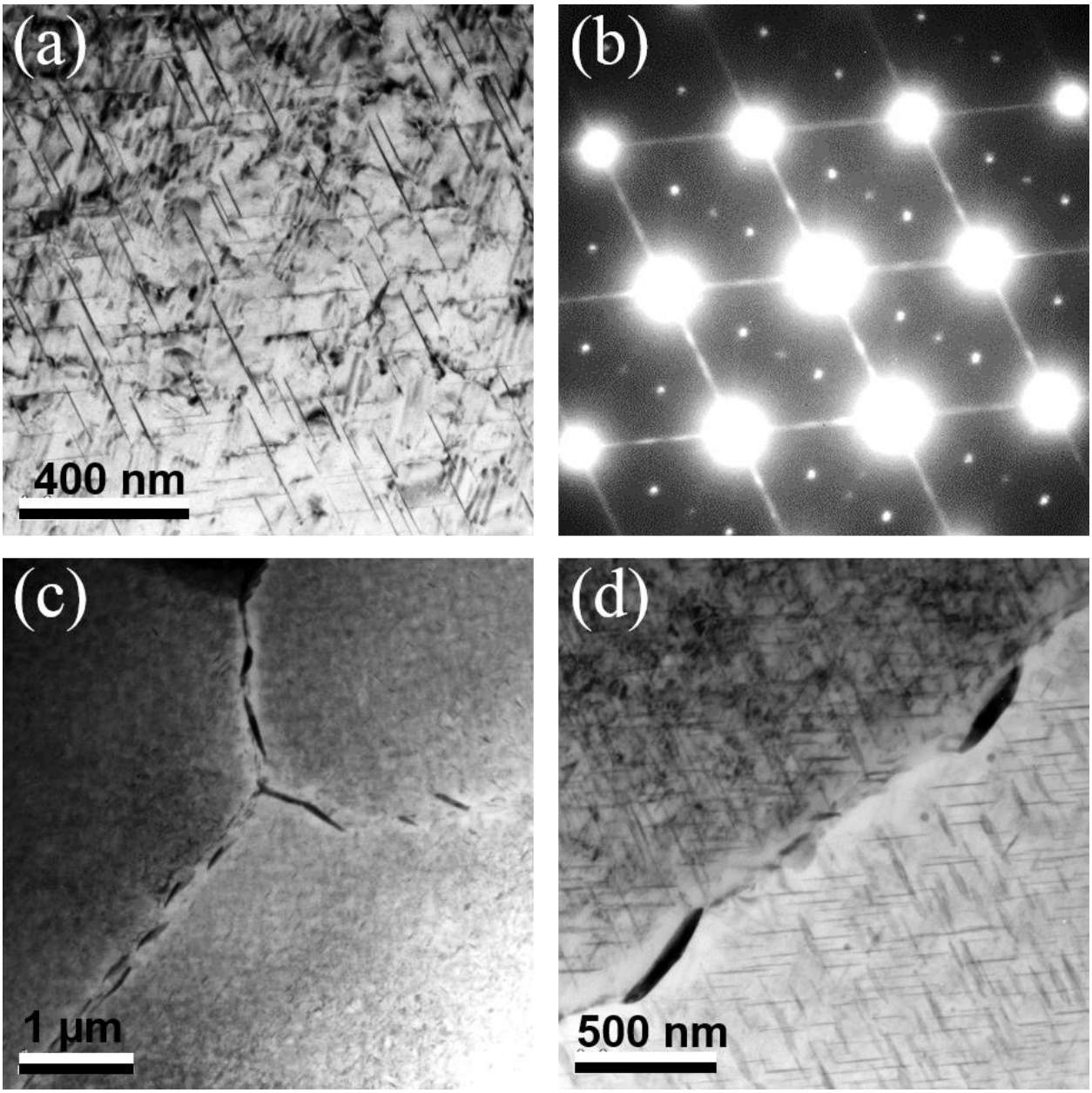

Figure 4.13 TEM image of (a) (c) (d) HAZ of FSW of 2195 aged for 100 hours, (b) SADP of an area shown in (a).

4.5 Conclusion

1. As compared to FSW, UWFSW reduced the extent of strength loss in HAZ and TMAZ in as welded and aged condition, but very small effect on strength in WN was observed.
2. Similar hardness and DSC results of alloy 2195 and 2098 showed that small variation in

Cu content did not affect the post FSW properties.

3. Weld nugget of 2195 showed very limited strength improvement after aging at 160°C for 16 hours. This is due to delayed aging kinetics of T1 precipitate due to the reduced dislocation density after recrystallization in weld nugget.
4. Whereas, weld nugget of 2199 showed no response to first aging treatment for 16 hours. Ag is known to enhance the nucleation and growth of T1 precipitate in Al-Cu-Li alloys. Absence of both Ag and dislocation density in 2199 was ascertained as the key reason for extremely delayed response to the aging treatment.
5. Coarse grain boundary precipitates were responsible for knock down in strength in HAZ after aging.

Acknowledgments

The authors gratefully acknowledge the financial support provided by the Center for Friction Stir Processing, which is a National Science Foundation I/UCRC supported by Grant No. 1157754. The authors also acknowledge the UNT Center for Advanced Research and Technology (CART) for microscopy facilities.

4.6 References

[1] E.J. Lavernia, N.J. Grant, Aluminium-lithium alloys, J. Mater. Sci. 22 (1987) 1521-1529.

[2] N.E. Prasad, A. Gokhale, R. Wanhill, Aluminum-Lithium Alloys: Processing, Properties, and Applications, Butterworth-Heinemann, 2013.

[3] A. Kostrivas, J. Lippold, Weldability of Li-bearing aluminium alloys, International materials reviews. 44 (1999) 217-237.

[4] E. Starke, J. Staley, Application of modern aluminum alloys to aircraft, Prog. Aerospace Sci. 32 (1996) 131-172.

[5] T. Dursun, C. Soutis, Recent developments in advanced aircraft aluminium alloys, Mater Des. 56 (2014) 862-871.

[6] I. Fridlyander, A. Dobromyslov, E. Tkachenko, O. Senatorova, Advanced high-strength aluminum-base materials, Metal science and heat treatment. 47 (2005) 269-275.

[7] W. Cassada, G. Shiflet, E. Starke, The effect of plastic deformation on Al2CuLi (T 1) precipitation, Metallurgical Transactions A. 22 (1991) 299-306.

[8] H.H. Jo, K. Hirano, Precipitation Processes in Al-Cu-Li Alloy Studied by DSC, 13 (1987) 377-382.

[9] B. Noble, G. Thompson, Precipitation characteristics of aluminium-lithium alloys, Metal Science Journal. 5 (1971) 114-120.

[10] B. Noble, G. Thompson, T 1 (Al2CuLi) Precipitation in Aluminium–Copper–Lithium Alloys, Metal Science Journal. 6 (1972) 167-174.

[11] R.J. Rioja, J. Liu, The evolution of Al-Li base products for aerospace and space applications, Metallurgical and Materials Transactions A. 43 (2012) 3325-3337.

[12] N.E. Prasad, A. Gokhale, R. Wanhill, Aluminum-Lithium Alloys: Processing, Properties,

and Applications, Butterworth-Heinemann, 2013.

[13] B.-. Huang, Z.-. Zheng, Independent and combined roles of trace Mg and Ag additions in properties precipitation process and precipitation kinetics of Al–Cu–Li–(Mg)–(Ag)–Zr–Ti alloys, Acta Materialia. 46 (1998) 4381-4393.

[14] W. Thomas, E. Nicholas, J. Needham, M. Murch, P. Templesmith, C. Dawes, International patent application no. (1991).

[15] R.S. Mishra, Z. Ma, Friction stir welding and processing, Materials Science and Engineering: R: Reports. 50 (2005) 1-78.

[16] R.S. Mishra, M.W. Mahoney, Friction Stir Welding and Processing, ASM International, 2007.

[17] R.S. Mishra, P.S. De, N. Kumar, Friction Stir Welding and Processing: Science and Engineering, Springer, 2014.

[18] R.S. Mishra, P.S. De, N. Kumar, Fundamentals of the Friction Stir Process, Springer, 2014.

[19] A.K. Shukla, Friction stir welding of thin-sheet, age-hardenable aluminum alloys: A study of process/structure/property relationships, ProQuest Dissertations and Theses. (2007).

[20] M. Starink, Analysis of aluminium based alloys by calorimetry: quantitative analysis of reactions and reaction kinetics, International Materials Reviews. 49 (2004) 191-226.

[21] X. Li, M. Starink, DSC study on phase transitions and their correlation with properties of overaged Al-Zn-Mg-Cu alloys, Journal of materials engineering and performance. 21 (2012) 977-984.

[22] J. Buha, R.N. Lumley, A.G. Crosky, Secondary ageing in an aluminium alloy 7050, Materials Science and Engineering: A. 492 (2008) 1-10.

[23] M.J. Starink, S.C. Wang, A model for the yield strength of overaged Al–Zn–Mg–Cu alloys,

Acta Materialia. 51 (2003) 5131-5150.

[24] M. Starink, Effect of compositional variations on characteristics of coarse intermetallic particles in overaged 7000 aluminium alloys, Materials science and technology. 17 (2001) 1324-1328.

[25] C.B. Fuller, M.W. Mahoney, M. Calabrese, L. Micona, Evolution of microstructure and mechanical properties in naturally aged 7050 and 7075 Al friction stir welds, Materials Science and Engineering: A. 527 (2010) 2233-2240.

CHAPTER 5

PAPER IV: EFFECT OF WELDING PARAMETERS AND THERMAL MANAGEMENT ON MICROSTRUCTURE AND PROPERTY EVOLUTION IN FRICTION STIR WELDED 2050-T3 ALLOY

5.1 Abstract

Friction stir welding of an underaged Al-Cu-Li alloy 2050 was conducted to study the effect of welding parameters on microstructure and mechanical properties of weld. The effect of thermal management using different backing was also investigated. Microhardness, tensile testing, differential scanning calorimetry, and transmission electron microscopy were used to characterize the microstructure and properties. Among the parameters used, localized joint strength of welds varied from 50% to 75% of peak aged base material strength. Strength recovery in weld nuggets after post weld heat treatment was higher for welds made at higher traverse speeds and with higher heat input. Use of different backing plates to manipulate cooling rate during welding was important to obtain the best results. Grain boundary precipitation, coarsening, and absence of strengthening precipitates were responsible for low strength recovery in low temperature and slow traverse speed welds.

Keywords: Friction stir welding, Al-Cu-Li alloys, differential scanning calorimetry, precipitation.

5.2 Introduction

Al-Cu-Li alloys are again gaining interest from the aerospace industry due to the combination of light weight and high strength offered by this particular alloy category [1,2]. Alloy 2195 developed in the United States in 1992 is regarded as one of the commercially successful Al-Cu-Li alloys, as it found applications in external super-lightweight tank of the

space shuttle by replacing the denser incumbent 2219 alloy [3].

Newly developed Al-Cu-Li alloys such as 2050 and 2198 contains lower amounts of Li (< 1.4%) to restrict the formation of δ′ (Al_3Li) precipitate, which deteriorates fracture toughness of the alloy [2,4,5]. AA2050 was recently developed in medium to thick gages with an aim to replace 7050-T7451 in commercial aircraft structure application [2]. AA2050 has been shown to offer lower density, higher corrosion resistance, higher modulus, higher yield strength and better fatigue life compared to incumbent 7050 alloy [2].

Al-Cu-Li alloys with chemistry similar to 2050 alloy derive their strength mainly from precipitation of thin platelets of T_1 (Al_2CuLi) phase that form during artificial aging at 150-200°C [3,6,7]. Al-Cu based θ′ (Al_2Cu) can also form in much lower quantity [8]. Nucleation and growth rates of T_1 phase are known to be favored by the presence of dislocation structures [6,9,10]. T_1 precipitation can be further enhanced by adding Mg and Ag together [11-13]. Silver alone has no significant impact on the precipitation of the T_1 phase [11]. Mn and Zr are added to precipitate dispersoid to restrain recrystallization during thermo-mechanical processing [8].

AA2050 is intended for aerospace structural applications [2] where welding of different parts is a critical step. In the last decade, friction stir welding (FSW) has evolved and has been established as the desired joining technique for joining precipitation strengthened aluminum alloys [14-19]. Conventionally, FSW of aluminum alloys leads to the formation of distinct microstructural zones. The zones are: recrystallized weld nugget (WN), thermo-mechanical affected zone (TMAZ) containing highly deformed grains, and heat affected zone (HAZ) [14-17,19]. Final properties and microstructure of FSWed (read as friction stir welded) precipitation strengthened aluminum alloys are greatly influenced by the choice of welding parameters [14,16,17,20]. Typically, FSW of aluminum alloys results in temperature generation in the range

of 400-550°C in WN [14,16,17]. For peak aged alloys, high temperature reached during welding in the WN leads to dissolution of precipitates and re-precipitation is also possible during cooling, depending on the choice of welding parameters and the use of any external cooling [20]. Microstructurally, TMAZ is a transition zone between WN and HAZ. TMAZ could experience a combination of precipitate dissolution, re-precipitation, and/or coarsening, depending on parameters [16,17,20]. HAZ experiences a temperature spike range between 250-350°C [21,22], which results in extensive coarsening of precipitates [23]. The soaring interest in Al-Li alloys [24] has led to numerous studies on FSW of different Al-Li alloys [25-33]. The majority of the studies were conducted on Al-Li alloy in thin gages (<6.35 mm) in peak aged (T8) condition [31-33].

In case of FSW of under-aged alloys, although dissolution of precipitates does not occur, as there are no precipitates in the matrix; but precipitation and coarsening during heating and cooling cycles of welding is possible. Generally, heat generated during FSW results in formation of solid solution. The cooling cycle is important to retaining solutes in the solid solution. A high level of solute retention could lead to homogenous precipitation during post weld aging of the weld [20]. Hence, understanding and managing the heat content during FSW of precipitation strengthened aluminum alloys is critical [20,34]. Despite increasing popularity of the alloy system and the feasibility of the joining process, very few studies have focused on FSW thick-plate of Al-Cu-Li in under-aged condition [27]. Furthermore, for the application of recently developed alloys (examples 2050 and 2198), what is needed is an understanding of the effect of process parameters and thermal management during welding on microstructure and mechanical property of FSWed under-aged Al-Cu-Li alloy in thick gage.

The aim of this study is to present the effect of FSW parameters and external cooling

medium on microstructural and mechanical property evolution in FSW of under-aged 2050 alloy in thick gage. In this paper, we report the response of weld to post weld heat treatment (PWHT) for various welding parameters. Localized microstructural analysis was carried out to increase understanding. Techniques such as hardness testing, tensile testing, differential scanning calorimetry (DSC), and transmission electron microscopy (TEM) were used to probe structure property-relationships.

5.3 Materials and Methods

5.3.1 Friction Stir Welding

The alloy used in this study is a third generation Al-Cu-Li alloy AA2050 in under-aged condition (hereinafter called T3 condition). The chemical composition limits of the main alloying elements of the alloy are listed in Table 5.1. FSW of 20 mm thick 2050-T3 alloy was performed using a tool which consisted of a scroll shoulder and truncated cone pin with threads and three flats. The pin length, pin tip diameter, pin root diameter, and shoulder diameter were 15 mm, 8 mm, 13 mm, and 29 mm, respectively. Six welds were made using the parameters listed in Table 5.2. Precipitation strengthened aluminum alloys are affected by the thermal experience during FSW, which suggests that thermal management during welding could have an impact on the final properties of weldments. Therefore, either AL-6XN steel (thermal conductivity = 11.8 W/mK) or a combination of an aluminum alloy (thermal conductivity ≈ 190 W/mK) and steel (hereinafter called Al+steel backing) was used as a backing plate to manipulate the thermal experience during welding. The peak temperature reached inside the center of tool pin for each weld was recorded and is listed in Table 5.2.

Table 5.1 Chemical composition limits of main alloying elements in AA2050 [26,27]. Please note that limits of minor impurity elements which may exist are not listed here.

Element	Cu	Li	Mg	Ag	Mn	Zr	Zn	Ti
Wt. %	3.2-3.9	0.7-1.3	0.2-0.6	0.2-0.7	0.2-0.5	0.06-0.14	0.25	0.1

Table 5.2. FSW parameters, different backing, and peak pin temperature reached during welding of 2050 alloy.

Weld ID	Tool rotation (RPM)	Welding speed (IPM)	Backing plate	Peak pin temperature (°C)
29A	420	12	Al+steel	547
30A	420	12	AL-6XN	539
29B	280	8	Al+steel	525
30B	280	8	AL-6XN	523
29C	200	4	Al+steel	496
30C	200	4	AL-6XN	506

5.3.2 Mechanical Property Evaluation

Microhardness measurements and ASTM-E8 standard tensile testing were conducted to evaluate mechanical properties of the welds. Samples were subjected to PWHT in a forced air oven at 160°C for 16 hours. Samples were tested in both as-welded and post weld heat treated conditions. To evaluate the local response, 15 mm thick welds were sectioned into 3 layers with a thickness of ≈5 mm each, as shown in Figure 5.1a, using electric discharge machining for mechanical property determination. The three sectioned parts of weld were named as: top 5 mm as L1, next 5 mm (middle of weld) as L2, and bottom 5 mm as L3 (see Figure 5.1a). Vickers microhardness measurement across the weld cross section was conducted using a Wilson Tukon 1202 hardness tester. Hardness measurements were taken at the middle thickness of each

sectioned layer (L1, L2, and L3) as shown in the schematic in Figure 5.1a. Transverse tensile testing samples, as shown in Figure 5.1b, from each layer with a thickness of ≈ 4.8-5.0 mm were prepared according to ASTM-E8 (sub-size) standard in such a way that thickness of L1 (L2 or L3) served as the thickness of gage of tensile sample.

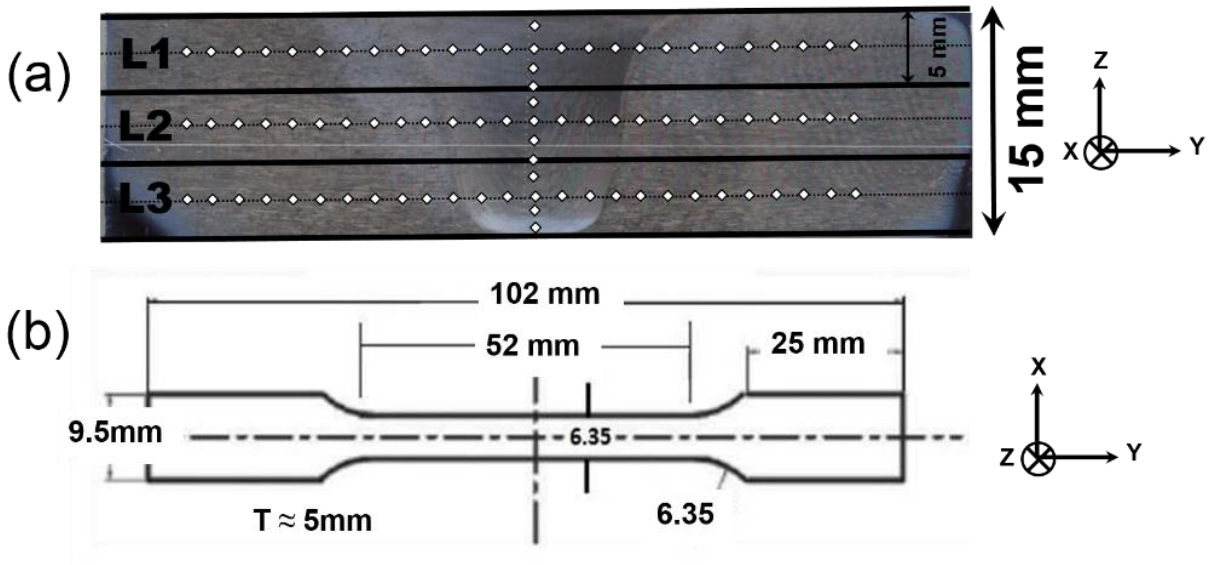

Figure 5.1 Schematic representation of (a) sectioning of weld into 3 layers for microhardness (white dots) and tensile testing and (b) shape and dimensions of tensile sample.

Thermal and Microstructural Evaluation

DSC measurements were performed on selected samples chosen based on the results of microhardness and tensile testing results. A Netzsch 204 F1 Phoenix® was used to perform DSC with a heating or cooling rate of 10°C per minute for all the samples. Samples were disk shaped with 4 mm diameter. All the samples were polished to keep the weight of sample around 30mg.

TEM was performed on samples from the selected location. Samples for TEM were mechanically polished to a thickness of ≈90 μm. Electron transparent 3 mm diameter discs were made using the Gatan ion polishing system. TEM was carried out using FEI Technai™ operating at 200 kV.

5.4 Results and Discussion

5.4.1 Temperature Evolution During FSW

The temperature at the center of the tool pin was recorded for every weld and is presented in Table 5.2. A clear trend of dependence of peak temperature on the tool rotation rate (RPM) can be noticed. Peak temperature increased from 496°C for 29C (200 RPM) to 547°C for 29A (420 RPM). Meanwhile, although two types of backing plate were used to manipulate the thermal cycle during welding, no significant effect on peak temperature was observed. The different type of backing (heat sink) is believed to impact heating and cooling rates more than the peak temperature [34]. During FSW, the major fraction of heat is generated by the shoulder of the tool [15-17]. Temperature along weld depth decreases [21-23] as the surface area of the tool that generates heat by plasticizing the material also decreases. Heating and cooling rates are also known to decrease along the weld depth [23]. The thermal cycle developed during thermo-mechanical processing of a precipitation strengthened aluminum alloy can affect the final properties, and hence will be discussed in subsequent sections in conjunction with other properties.

5.4.2 Microhardness Measurements

Microhardness profile for all six welds at different locations are shown in Figure 5.2. Hardness in as-welded (AW) condition was measured for 29A and 30C after 6-8 weeks of stabilization (natural aging) at room temperature. Hardness for AW samples was similar for all welds. Hardness profile was flat and varied around 115-125 HV (Figure 5.2i). These results are largely due to the starting temper of alloy being underaged, which upon FSW and subsequent natural aging resulted in a similar condition i.e., an underaged state. Typically such observation is seen in FSW of under-aged precipitation strengthened aluminum alloys [34] and is not focused

on in this study.

After PWHT, it is evident from hardness plots that the drop in hardness in nugget increased from top to the bottom of weld for all samples irrespective of parameters. Hardness of the 29A-PWHT sample dropped from 145 HV at the top to 111 HV at the bottom of the weld (Figure 5.2j). This trend was observed for all samples with varying levels of drop in hardness. Typically, it is seen in every case of FSW of precipitation strengthened aluminum alloys and is attributed to the relatively lower temperature at the bottom compared to the top of the weld [25,26,33,34]. Lower peak temperature and lower cooling rate at the bottom of the weld could initiate precipitation of precipitates during cooling of the weld. Coarsening of these precipitates during PWHT would inhibit homogenous precipitation and would result in lower hardness at the bottom of the weld. The fluctuation in hardness measurements is believed to be due to the local heterogeneity of the microstructure observed in thick plates. Also, spikes in hardness measurements along the depth of weld in 29A and 30A are due to the heterogeneity of the microstructure associated with the formation of onion rings [35].

Welds 29A and 30A, which were made with same parameters but different backing, showed different levels of hardness recovery after PWHT (Figure 5.2a and Figure 5.2d). Hardness in the nugget region of 29A-L1 fluctuated around 138-150 HV, whereas 30A-L1 was in the 128-140 HV range. Similarly, hardness in nugget region of 29A-L3 was around 120 HV and for 30A-L3 was 110 HV. This clearly indicates that using Al+steel backing in 29A resulted in higher hardness recovery in the nugget. Temperature in the nugget of 29A (547°C) and 30A (539°C) was high enough for full dissolution. In weld 29A, Al+steel backing supplied a higher cooling rate which would have restrained precipitation during cooling. The resultant solute content in solid solution would be higher in 29A compared to 30A and precipitated higher

volume fraction of finer particles and increased hardness after PWHT.

Hardness profiles of 29B and 30B after PWHT were not as contrasting as that of 29A and 30A. The higher hardness recovery due to the higher cooling rate offered by Al+steel backing was reduced in this scenario. Hardness for 29B was just slightly higher than 30B (Figure 5.2b and Figure 5.2e). Welds 29B and 30B were made with 280 RPM and 8 IPM as welding parameters, and peak temperatures were also low compared to 29A and 30A (see Table 5.2). So, conceivably, lower peak temperature and slower welding speed in case of weld 29B and 30B neutralized the effect of the Al+steel backing that was significant in weld 29A.

Hardness measurements of weld 29C and 30C indicated that the use of Al+steel backing was not beneficial, which was contrary to indications from earlier results. The drop in hardness in 29C (with Al+steel backing) was higher than 30C (with AL-6XN backing). Hardness in the nugget region of 29C-L1 was around 120-125 HV, whereas it was 130-135 HV for 30C-L1. Similarly, 29-L3 nugget region showed hardness of 96 HV, where it was fluctuating between 100-110 HV for 30C-L3. Note that the hardness in the nugget of the 29C-L3-PWHT sample was consistently lower than AW hardness. Peak temperature for weld 29C at the center of the weld was 496°C and would have been even lower at the bottom of the weld (L3). Possibly low temperature at the bottom of the weld (29C-L3) was further brought down by extra heat extraction provided by Al+steel backing. The lower temperatures in 29C-L3 might have resulted in precipitation and coarsening during welding, which led to further coarsening after PWHT. In the case of 30C, where heat input was the same as that of the 29C weld, AL-6XN was used as backing and has roughly 15 times lower thermal conductivity than aluminum. So, AL-6XN helped to build up heat during welding 30C. Heat rejection by AL-6XN backing resulted in higher peak temperature (506°C) in the 30C weld. This led to lesser coarsening which resulted in

better hardness in 30C-L3 as compared to 29C-L3. These speculations were made by correlating FSW parameters, temperature data, and hardness measurement results. Further analysis using DSC and TEM were carried out to establish the reasoning.

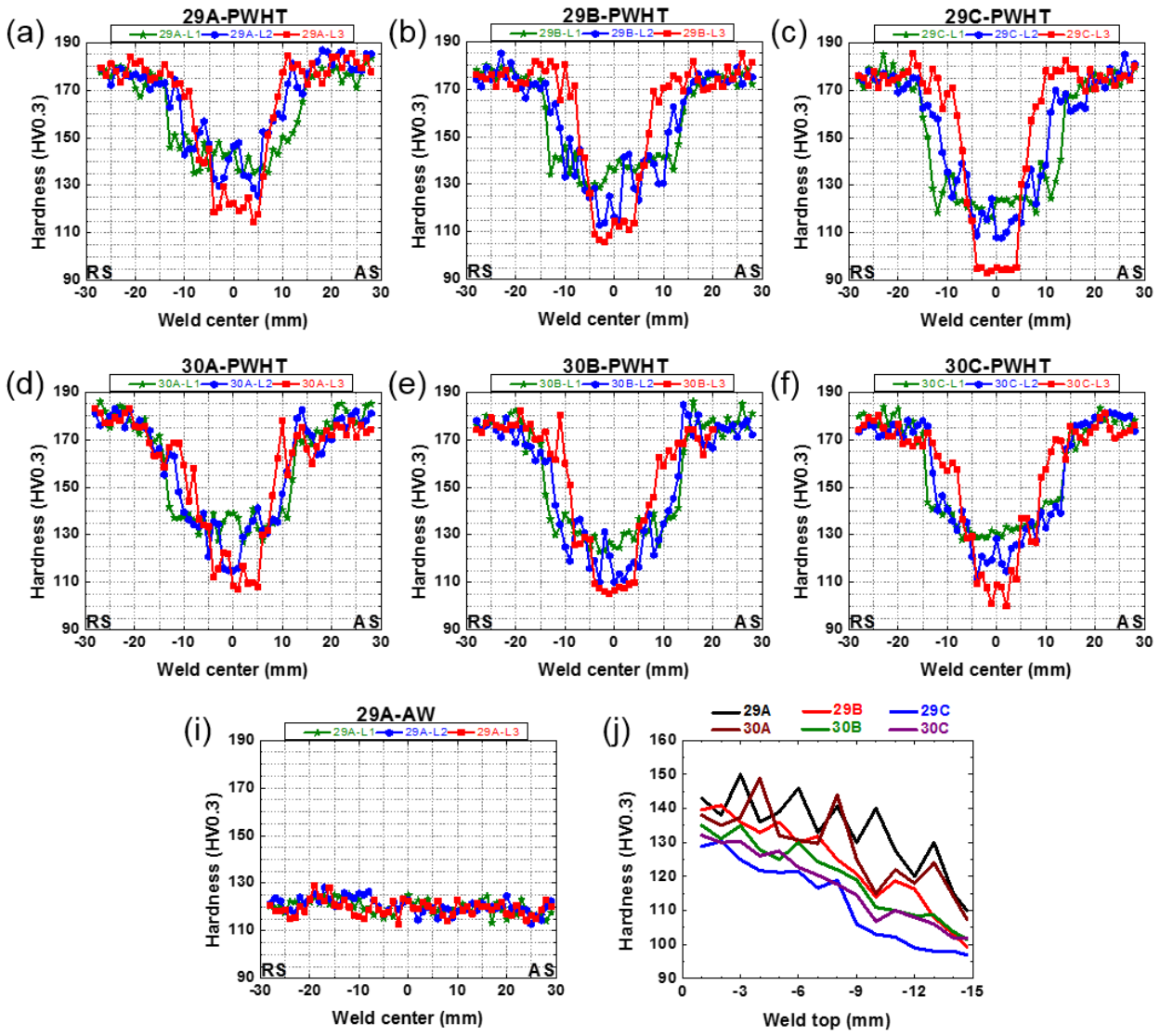

Figure 5.2 Microhardness distribution (a) in 29A-PWHT, (b) in 29B-PWHT, (c) in 29C-PWHT, (d) in 30A-PWHT, (e) in 30B-PWHT, (f) in 30C-PWHT,(i) in 29A-AW, and (j) along the depth for all six welds in PWHT condition.

5.4.3 Tensile Testing

Tensile testing of sliced joints was performed to evaluate the joint strength of all the

welds. Yield strength (YS), ultimate tensile strength (UTS), and elongation to failure of base material 2050 in underaged and artificially aged conditions are presented in Table 5.3. The results of tensile testing of all the samples are shown in Figure 5.3a and Figure 5.3b. Yield strength of all welds in AW condition was in the 250-275 MPa range. Strength of all the samples after PWHT showed a trend similar to the hardness results. The strength level dropped along the depth of the weld in every case. As expected, after PWHT, UTS results also followed similar trends for all samples. Among the welds, YS dropped from 336 MPa for 29A-L1 to 222 MPa for 30C-L3. YS for 29C-L3, which showed lower hardness than 30C-L3, was 225 MPa. This could be a result of the composite behavior of the 5mm thick tensile sample whereas hardness is a localized response. Elongation to failure (Figure 5.3b) of all the samples ranged in 6-9% after PWHT. Joint efficiency (JE) of each sample was calculated to evaluate overall strength recovery in each sample with respect to base material. JE, presented in Figure 5.3c, was calculated for YS and UTS results for each sample. JE of 75% (based on YS) for 29A-L1 and 49% (based on YS) for 30C-L3.

Table 5.3 Mechanical properties of base material 2050 in underaged and artificially aged (160°C for 16 hours) condition.

Sample	**Y.S. (MPa)**	**U.T.S. (MPa)**	**Total elongation (%)**
2050-T3 (T)	252.2±9	389.8±13.8	15.2±1.4
2050-T8 (T)	453.3±0.9	520.4±2.1	7.6±1

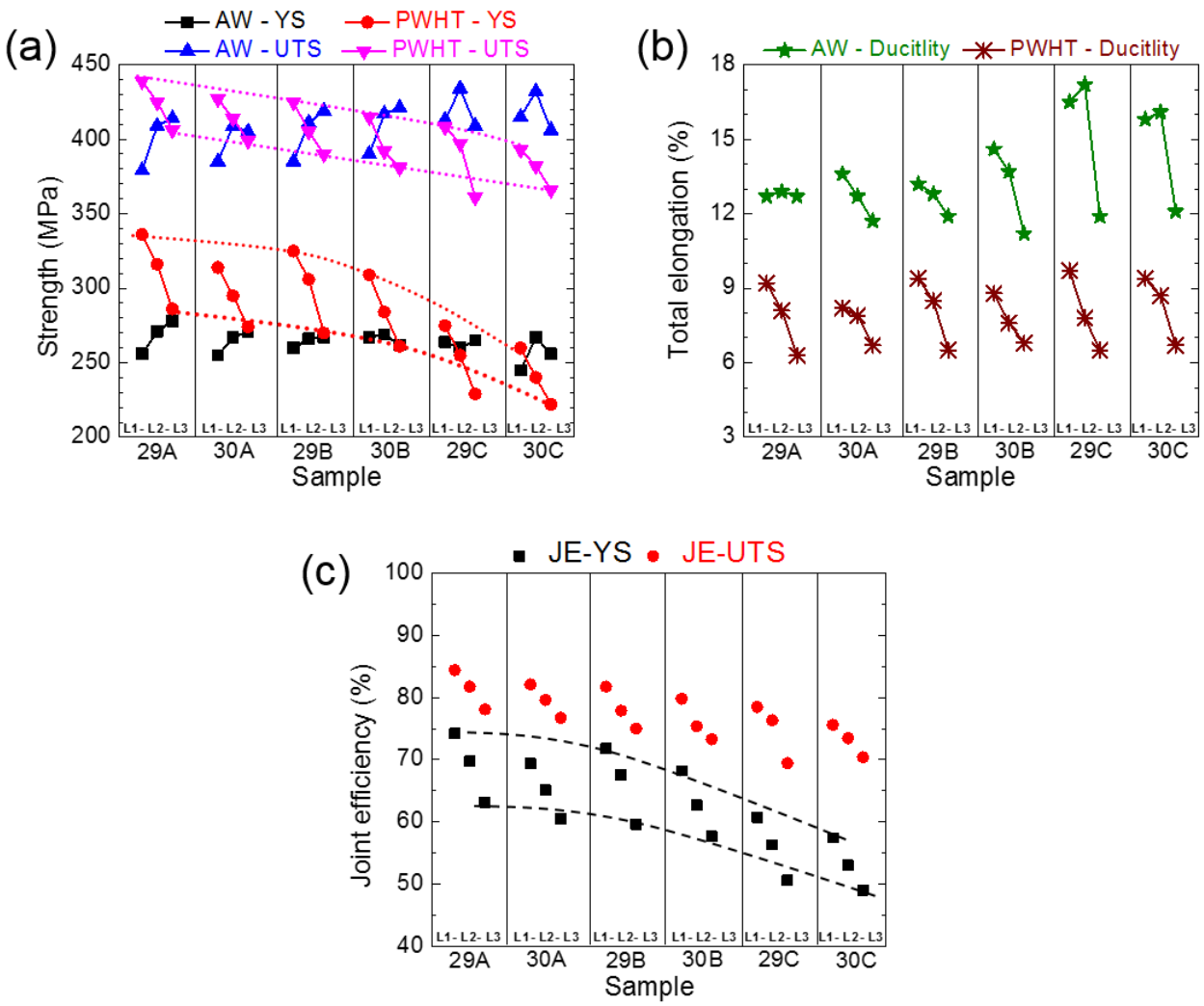

Figure 5.3 Plots of (a) YS and UTS of all the samples in AW and PWHT conditions, (b) total elongation showed all the samples, and (c) JE of all the samples with respect to artificially aged base material base material properties.

5.4.4 Precipitation and its Kinetics

DSC is considered a reliable and powerful tool to study solid state reactions, such as precipitation and dissolution of second phases, in precipitation strengthened aluminum alloys [36]. DSC experiments were performed on samples taken from selected locations in different welds. Samples 29A-AW-L1, 29A-AW-L3, 30C-AW-L1, and 30C-AW-L3 were studied to evaluate the effect of welding parameters and weld depth on precipitation kinetics in FSWed

2050 alloy. Samples from 2050 base material in underaged (BM-T3) and artificially aged conditions (BM-T8) were also chosen to benchmark the precipitation kinetics in 2050 alloy. Weld 29C produced peculiar mechanical properties and thus DSC of 29C-AW-L3 was also conducted. DSC curves of all samples but BM-T8 show two small endothermic peaks around 140°C and 220°C (Figure 5.4). The endotherm at 140°C is signature of dissolution of solute clusters formed due to natural aging of samples [37,38]. The peak at 220°C is formed as a result of dissolution of the small amount of δ′ (Al_3Li) formed during natural aging [37,38]. Both endotherms are consistently present for all the samples that went through similar natural aging, thus will not be discussed further. Major exothermic peak (peak A in Figure 5.4) observed in the range of 240-310°C for various samples is due to precipitation of T_1 (Al_2CuLi) precipitate. It was further confirmed by the absence of the same peak in BM-T8 as the sample was already peak aged and would not show significant T_1 precipitation. Note that T_1 precipitation exotherm in the case of BM-T3 is sharper, larger, and occurred at much lower temperature than others. Delayed T_1 exotherm formation for all samples from weld nugget shows that aging of T_1 precipitate in the nugget is sluggish and is favored to form at higher temperature or longer time. T_1 precipitation is known to be expedited by the presence of dislocations [6,9]. Very low dislocation density in recrystallized nugget resulted in delayed precipitation kinetics. T_1 precipitation peak shifted from 240°C for BM-T3 to 267°C, 298°C, and 312°C for 29A-AW-L1, 30C-AW-L3, and 29C-AW-L3 respectively. Also of note is that the amplitude of precipitation event (peak A) is considerably smaller for samples from weld nugget compared to BM-T3. Among samples from nugget (29A-AW-L1, 30C-AW-L3, and 29C-AW-L3), the amplitude of peak A decreased in accordance with trends observed in mechanical properties. Smaller precipitation peak also indicates that the amount of available solute in solid solution to precipitate out is lesser compared to BM-T3.

An endothermic event taking place in temperature range 370-460°C is due to dissolution of precipitates. Another small exothermic peak (labelled as peak B) is due to thickening of platelets of T_1 precipitate [37]. It is further confirmed by its presence in BM-T8 curve as coarsening of already present precipitate will occur in this case. This curve convoluted along with T_1 precipitation peak for samples from the weld nugget. Thus, prolonged aging kinetics of precipitates, smaller precipitation peak, and overlapping precipitation and coarsening peak for samples from the weld nugget suggest that coarsening of precipitates during PWHT could have occurred. Furthermore, a very similar dissolution event (peak C) for all the samples indicates that similar quantities of solutes had precipitated out in each case during PWHT.

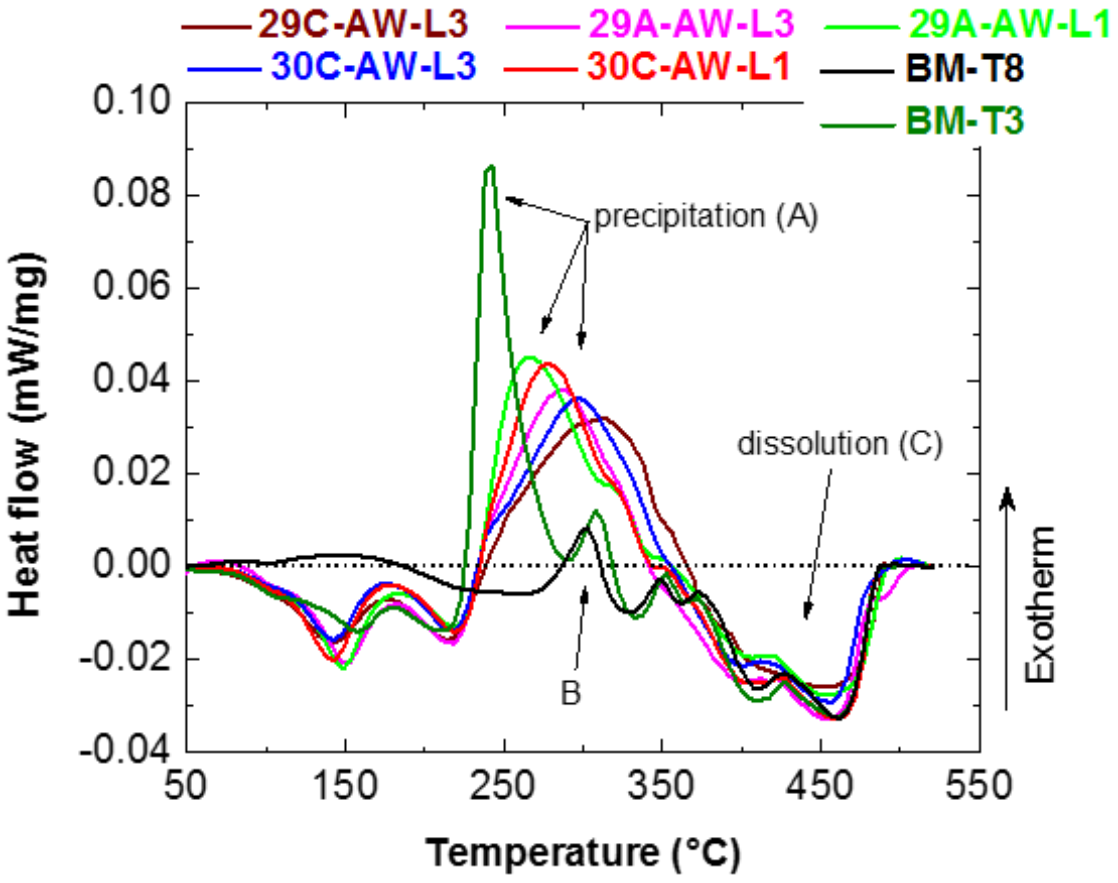

Figure 5.4 DSC heat flow curves for various samples from base material and nugget of different welds.

5.4.5 Microstructural Evaluation

TEM was conducted for selected samples taken from BM-T8, 29A-PWHT-L1, 29C-PWHT-L3, and 30C-PWHT-L3. High density of T_1, the predominant strengthening precipitate in 2050 alloy, was present as platelets in the base material in an artificially aged condition (Figure 5.5a) [8]. T_1, which precipitates on {111} planes of aluminum matrix, can be identified as streaks along <111> directions and spot at 1/3<220> in the selected area diffraction pattern (SADP) taken along [110] (Figure 5.5b) [8]. 29A-PWHT-L1 sample, which showed highest strength recovery, also showed (Figure 5.5c and Figure 5.5d) high density of T_1 precipitates similar to BM-T8. This explains the high level of strength recovery for 29A sample. Grain boundary (GB) and sub-grain boundary (SGB) precipitates (Figure 5.5d), of the scale of ≈1μm, were also observed in 29A sample. That very few of these precipitates were observed in BM-T8 sample suggests that coarsening of precipitates occurred due to solute loss during the cooling cycle of welding. Less than full strength recovery in 29A-PWHT-L1 can be attributed to the presence of coarse GB precipitates.

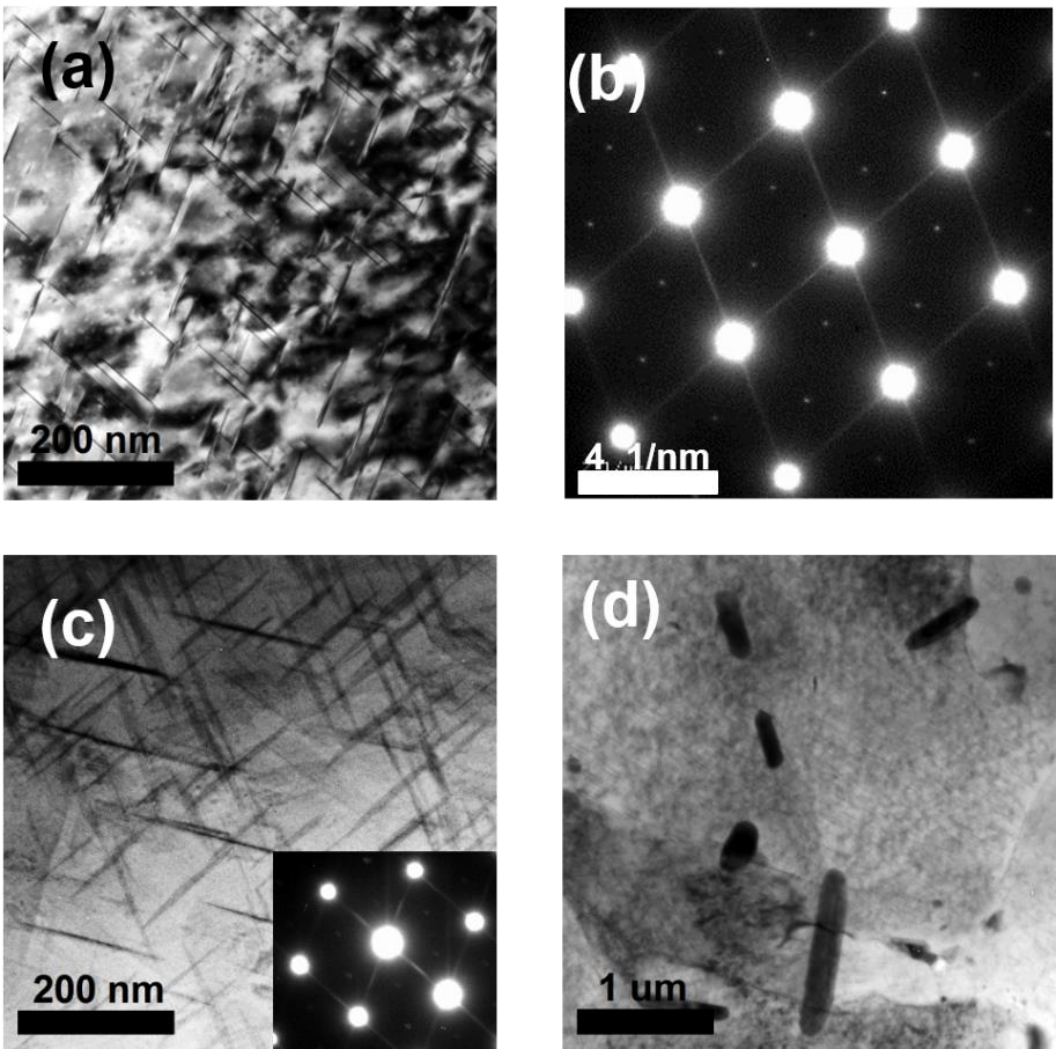

Figure 5.5 TEM (a) BF image of BM-T8 near [110], (b) SADP of (a) along [110], (c) BF image of 29A-PWHT-L1 with corresponding SADP in inset, and (d) BF image of 29A-PWHT-L1 showing T_1 and grain boundary precipitation.

Figure 5.6a shows bright field (BF) image of 30C-PWHT-L3. No T_1 precipitates were observed in the analyzed sample. Moreover, SADP (Figure 5.6b) also did not reveal the presence of T_1 precipitates. Note the overexposed intensity of SADP spots. Extensively coarsened GB, SGB, and matrix precipitates were observed. Dislocation structures in the grain were also decorated with coarse precipitates. The sample showed very low dislocation density. TEM analysis of 29C-PWHT-L3 sample also showed similar results with extensive coarsening of

precipitates.

Combined analysis of mechanical property results, DSC, and TEM explains that coarsening of precipitates due to slow heating cycle, low peak temperature, and low cooling rate produced low level strength recovery in 29C and 30C welds. Welds 29A and 30A experienced higher peak temperature and higher cooling rates and resulted in lesser coarsening of precipitates. Use of Al+steel backing was beneficial in the case of high peak temperature and faster traverse speed welds, whereas it degraded the properties for the low peak temperature and slower traverse speed welds.

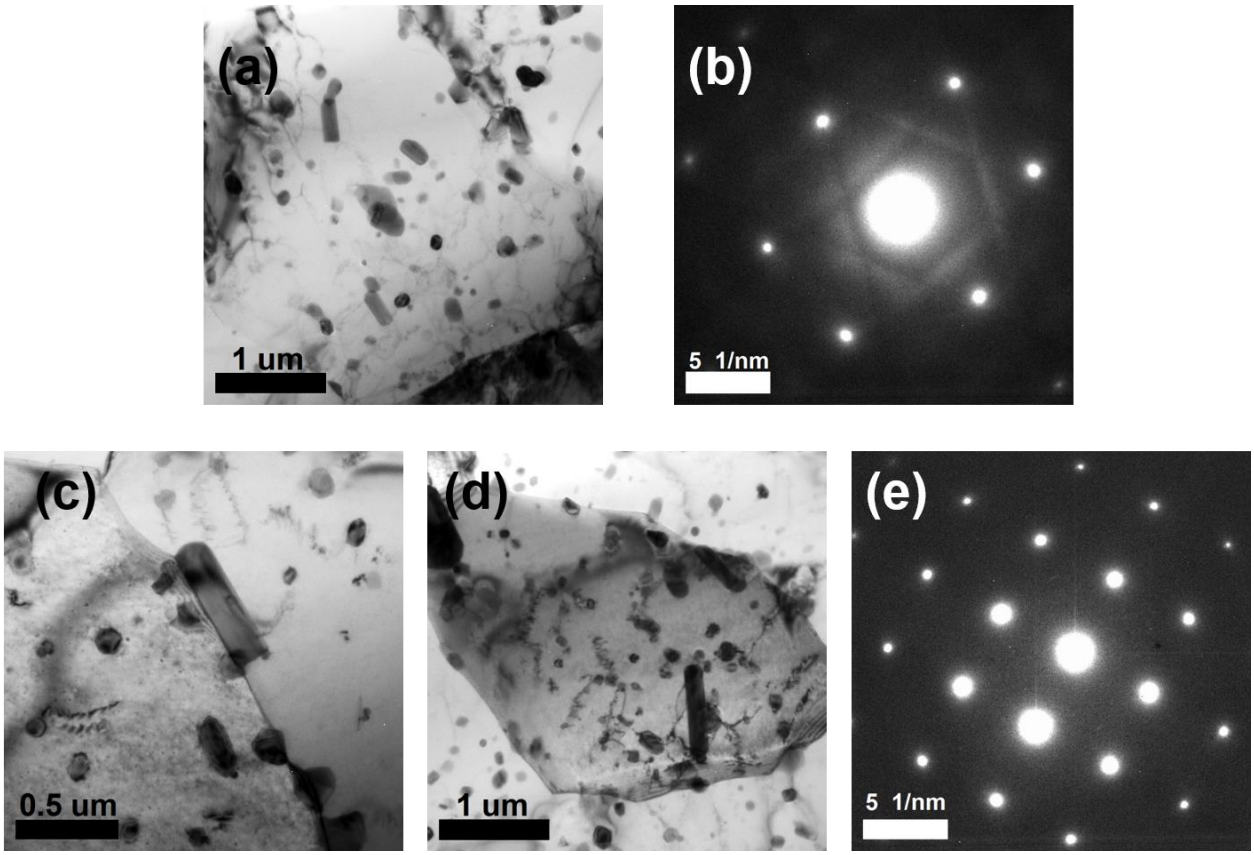

Figure 5.6 TEM (a) BF image of 30C-PWHT-L3, (b) SADP of (a), (c) and (d) BF images of 29C-PWHT-L3 showing grain boundary and matrix precipitation and its coarsening (note very low dislocation density in the entire micrographs), and (e) SADP of grain in (d)

along [001].

5.5 Conclusion

In this paper we studied the effect of welding parameters and thermal management using external cooling medium on the resultant microstructure and mechanical properties of FSWed 2050 alloy in thick gage, leading to the following conclusions.

1. Choice of welding parameters and thermal management during and after FSW of precipitation strengthened aluminum alloys can greatly influence the final properties and microstructure.
2. Joint efficiency as high as 75% (YS based) was achieved for 29A-L1 after PWHT.
3. Higher strength recovery in welds 29A and 30A made with high peak temperature and faster welding speeds resulted from higher cooling rates. Cooling rates were enhanced by the use of Al+steel backing.
4. T_1 precipitation is known to be favored by the presence of dislocations. Low dislocation density in recrystallized weld nugget resulted in delayed aging kinetics and hence lower strength recovery was observed.
5. 29C and 30C were low temperature and welds and offered low cooling rates, as welding speeds were low. GB precipitation and coarsening occurred during cooling cycle of weld. Further coarsening during PWHT and absence of strengthening precipitate were identified as the main causes for low strength recovery in these welds.

Acknowledgments

The authors gratefully acknowledge the financial support provided by the Center for Friction Stir Processing, which is a National Science Foundation I/UCRC supported by Grant No. 1157754.

5.6 References

[1] Rioja RJ, Liu J. The evolution of Al-Li base products for aerospace and space applications. Metallurgical and Materials Transactions A 2012;43:3325-37.

[2] Lequeu P, Smith KP, Daniélou A. Aluminum-Copper-Lithium Alloy 2050 Developed for Medium to Thick Plate Journal of Materials Engineering and Performance 2009; 2010;19:841-847.

[3] Chen PS, Kuruvilla AK, Malone TW, Stanton WP. The Effects of Artificial Aging on the Microstructure and Fracture Toughness of Al-Cu-Li Alloy 2195 Journal of Materials Engineering and Performance 1998;7:682-690.

[4] Suresh S, Vasudevan A, Tosten M, Howell P. Microscopic and macroscopic aspects of fracture in lithium-containing aluminum alloys. Acta Metallurgica 1987;35:25-46.

[5] Gregson P, Flower H. Microstructural control of toughness in aluminium-lithium alloys. Acta metallurgica 1985;33:527-37.

[6] Cassada W, Shiflet G, Starke E. The effect of plastic deformation on Al2CuLi (T 1) precipitation. Metallurgical Transactions A 1991;22:299-306.

[7] Huang B, Zheng Z. Effects of Li Content on Precipitation in Al-Cu-(Li)-Mg-Ag-Zr Alloys. Scr Mater 1998;38:357-62.

[8] Wang S, Starink M. Precipitates and intermetallic phases in precipitation hardening Al–Cu–Mg–(Li) based alloys. International Materials Reviews 2005;50:193-215.

[9] Gable B, Zhu A, Csontos A, Starke E. The role of plastic deformation on the competitive microstructural evolution and mechanical properties of a novel Al–Li–Cu–X alloy. Journal of Light Metals 2001;1:1-14.

[10] Ringer S, Muddle B, Polmear I. Effects of cold work on precipitation in Al-Cu-Mg-(Ag)

and Al-Cu-Li-(Mg-Ag) alloys. Metallurgical and Materials Transactions A 1995;26:1659-71.

[11] Huang B-, Zheng Z-. Independent and combined roles of trace Mg and Ag additions in properties precipitation process and precipitation kinetics of Al–Cu–Li–(Mg)–(Ag)–Zr–Ti alloys. Acta Materialia 1998;46:4381-93.

[12] Itoh G, Cui Q, Kanno M. Effects of a small addition of magnesium and silver on the precipitation of T1 phase in an Al-4%Cu-1.1%Li-0.2%Zr alloy. Materials Science and Engineering: A 1996;211:128-37.

[13] Khan A, Robinson J. Effect of silver on precipitation response of Al–Li–Cu–Mg alloys. Materials Science and Technology 2008;24:1369-77.

[14] Çam G, Mistikoglu S. Recent developments in friction stir welding of Al-alloys. Journal of Materials Engineering and Performance 2014;23:1936-53.

[15] Mishra R. Friction stir welding and processing. Metall Mat Trans A Phys Metall Mat Sci 2001;41:2507-21.

[16] Mishra RS, Ma Z. Friction stir welding and processing. Materials Science and Engineering: R: Reports 2005;50:1-78.

[17] Mishra RS, Mahoney MW. Friction Stir Welding and Processing. : ASM International, 2007.

[18] Thomas W, Nicholas E, Needham J, Murch M, Templesmith P, Dawes C. International patent application no 1991.

[19] Threadgill P, Leonard A, Shercliff H, Withers P. Friction stir welding of aluminium alloys. International Materials Reviews 2009;54:49-93.

[20] De PS, Mishra RS. Friction stir welding of precipitation strengthened aluminium alloys: scope and challenges Science and Technology of Welding and Joining 2011;16:343-347.

[21] Khandkar M, Khan JA, Reynolds AP. Prediction of temperature distribution and thermal history during friction stir welding: input torque based model. Science and Technology of Welding & Joining 2003;8:165-74.

[22] Nandan R, Roy G, Debroy T. Numerical simulation of three-dimensional heat transfer and plastic flow during friction stir welding. Metallurgical and materials transactions A 2006;37:1247-59.

[23] Xu W, Liu J, Luan G, Dong C. Temperature evolution, microstructure and mechanical properties of friction stir welded thick 2219-O aluminum alloy joints. Mater Des 2009;30:1886-93.

[24] Dursun T, Soutis C. Recent developments in advanced aircraft aluminium alloys. Mater Des 2014;56:862-71.

[25] Avettand-Fenoel M, Taillard R. Heterogeneity of the Nugget Microstructure in a Thick 2050 Al Friction-Stirred Weld. Metallurgical and Materials Transactions A 2015;46:300-14.

[26] De Geuser F, Malard B, Deschamps A. Microstructure mapping of a friction stir welded AA2050 Al–Li–Cu in the T8 state. Philosophical Magazine 2014;94:1451-62.

[27] Dhondt M, Aubert I, Saintier N, Olive J. Mechanical behavior of periodical microstructure induced by friction stir welding on Al–Cu–Li 2050 alloy. Materials Science and Engineering: A 2015;644:69-75.

[28] Fonda R, Bingert J. Precipitation and grain refinement in a 2195 Al friction stir weld. Metallurgical and materials transactions A 2006;37:3593-604.

[29] Pouget G, Reynolds AP. Residual stress and microstructure effects on fatigue crack growth in AA2050 friction stir welds. Int J Fatigue 2008;30:463-72.

[30] Schneider J, Nunes Jr A, Chen P, Steele G. TEM study of the FSW nugget in AA2195-T81.

J Mater Sci 2005;40:4341-5.

[31] Shukla A, Baeslack III W. Study of process/structure/property relationships in friction stir welded thin sheet Al–Cu–Li alloy. Science and Technology of Welding & Joining 2009;14:376-87.

[32] Shukla AK, Baeslack III WA. Study of microstructural evolution in friction-stir welded thin-sheet Al–Cu–Li alloy using transmission-electron microscopy. Scr Mater 2007;56:513-6.

[33] Steuwer A, Dumont M, Altenkirch J, Birosca S, Deschamps A, Prangnell PB et al. A combined approach to microstructure mapping of an Al–Li AA2199 friction stir weld. Acta Materialia 2011;59:3002-11.

[34] Upadhyay P, Reynolds A. Effect of backing plate thermal property on friction stir welding of 25-mm-thick AA6061. Metallurgical and Materials Transactions A 2014;45:2091-100.

[35] Sutton MA, Yang B, Reynolds AP, Yan J. Banded microstructure in 2024-T351 and 2524-T351 aluminum friction stir welds: Part II. Mechanical characterization. Materials Science and Engineering: A 2004;364:66-74.

[36] Starink M. Analysis of aluminium based alloys by calorimetry: quantitative analysis of reactions and reaction kinetics. International Materials Reviews 2004;49:191-226.

[37] Dorin T, Deschamps A, De Geuser F, Lefebvre W, Sigli C. Quantitative description of the T1 formation kinetics in an Al–Cu–Li alloy using differential scanning calorimetry, small-angle X-ray scattering and transmission electron microscopy. Philosophical Magazine 2014;94:1012-30.

[38] Malard B, De Geuser F, Deschamps A. Microstructure distribution in an AA2050 T34 friction stir weld and its evolution during post-welding heat treatment. Acta Materialia

2015;101:90-100.

CHAPTER 6

PAPER V: STRENGTH RECOVERY IN FRICTION STIR WELDED 7050-T7451 ALLOY DURING VARIOUS POST WELD HEAT TREATMENTS

6.1 Abstract

Friction stir welding of 7050-T7451 alloy was conducted using tool rotation rate of 600 revolutions per minute and traverse speeds of 127 and 762 millimeters per minute. High traverse speed resulted in high cooling rates, high solute retention in solid solution, and high retained dislocation density. Retained dislocation density assisted precipitation in all the heat treatment conditions and resulted in high hardness in weld nugget. Low temperature aging at 85°C reduced coarsening during heat treatment and resulted in high density of fine precipitates in weld nugget. Differential scanning calorimetry and electron microscopy results evidenced that strength recovery in low temperature aging was due to strengthening precipitates. For two different welds, tensile joint strength of 95% and 100% of the parent material strength was achieved after 85°C aging treatment. De-localization of strain along the gauge length due to higher strength recovery in low temperature aging resulted in higher elongation to failure.

Keywords: Friction stir welding, 7XXX alloys, differential scanning calorimetry, low temperature aging.

6.2 Introduction

High strength aluminum alloys such as 7XXX and 2XXX series alloys are primary alloys used in aircraft body and have numerous applications in the aerospace industry [1]. Joining of alloys of 7XXX series using conventional fusion welding techniques is difficult and rather undesirable, as dendritic microstructure and porosities formed during fusion welding can undermine the structural integrity of weldments [2,3]. Friction stir welding (FSW), invented in

1991 [4], is a solid state joining method that inherently eliminates drawbacks of fusion welding of high strength aluminum alloys [2,3,5]. FSW has emerged as the primary joining process of aluminum alloys in the aerospace industry [1-3,5]. FSW of precipitation strengthened aluminum alloys results in formation of distinct microstructural zones such as weld nugget (WN), thermo-mechanically affected zone (TMAZ), and heat-affected zone (HAZ). Generally, temperatures in WN of FSW of aluminum alloys range from 400-550°C [2,3,5]. WN consists of recrystallized grain structure. TMAZ, which experiences both heat and deformation, largely consists of deformed parent grains with high dislocation density. HAZ, where temperature is in 250-350°C range, is identified as the minima in hardness away from WN due to the coarsening of pre-existing parent material precipitates caused by thermal cycle during welding [2,3,5].

7XXX series is a category of high strength precipitation strengthened aluminum alloys with Zn, Mg, and Cu as the main alloying elements. Typical precipitation sequence in a 7XXX alloy is essentially [6-8]:

Super saturated solid solution (SSSS) → GP zones → η′ → η ($MgZn_2$)

The metastable η′ precipitate is a coherent phase (interfacial energy = 0.06 J/m^2) [9] which forms homogenously and GP zones act as precursors to it [10]. Precipitate η′ is the main strengthening phase in 7XXX alloys [11,12]. At high temperature or long aging hours η′ transforms into incoherent and stable η phase (interfacial energy = 0.7 J/m^2) [9,13]. However, strength contribution of η phase is less than that of η′ phase [9,13].

A plenitude of studies exists on FSW of 7XXX alloys [6,7,9,10,13-20]. The majority of these studies focused on evolution of microstructure and strength after FSW in as-welded and certain standard (T6 or T7) post-weld heat treatment (PWHT) conditions. Sullivan and Robson [6] studied the microstructural evolution after a standard T7 PWHT of friction stir welded

(FSWed) thick gauge 7449 alloy welded in underaged condition. They concluded that extensive coarsening during cooling of weld and after PWHT resulted in loss of strength in HAZ. Su et al. [20] explored in detail the microstructural variations in various metallurgical zones of FSWed 7050-T651 alloy. They observed coarse precipitates in WN and HAZ and a five-time increase in width of precipitate free zone (PFZ) after FSW. Similarly, Jata et al. [16] also reported a 5-times increase in size of precipitates and PFZ in HAZ of FSWed 7050-T7451 PWHT at 121°C for 24 hours. Reynolds et al. [17] studied the correlation between a wide range of FSW parameters and hardness evolution in WN and HAZ of FSWed 7050 alloy in as-welded and PWHT conditions. Their results demonstrated that for all the tested parameters, hardness in HAZ showed negative response to PWHT. Fuller et al. [10] studied strength recovery during long term natural aging of FSWed 7050-T7651 and 7075-T651 alloys. They observed that unlike PWHT, HAZ shows positive response to natural aging. It is well-established that FSW of any 7XXX alloy in overaged (or peak aged) condition results in coarsening of pre-existing precipitates in HAZ, which reduces the strength of HAZ [10,15]. Industrial PWHT temperatures (120-160°C) are usually selected in ranges where growth rates of strengthening precipitates are high enough to obtain the desired combination of properties and reasonable cost (or time) of production. At such high temperatures kinetics favors growth and coarsening of strengthening precipitates. PWHT at lower temperature can reduce coarsening rate and lead to high nucleation density as compared to high temperature aging. Aging at low temperatures has been reported to produce enhanced parent material properties as compared to standard high temperature aging [11,21]. Slow cooling rates associated with FSW result in re-precipitation of precipitates in WN during cooling of weld. Similar to the situation in HAZ, coarsening of precipitates in WN, especially in case of thick sections, during PWHT at high temperatures can significantly impact weld strength. Achieving

high cooling rates by using auxiliary cooling methods and aging at low temperature can reduce the extent of coarsening during PWHT of the weld.

While detailed experiments on characterizing FSW of 7XXX alloys exist, efforts to improve strength in HAZ and the entire weld cross section are yet to be made. In this work, we studied the response of FSWed 7050 alloy subjected to various PWHT. Our aim was to study the effect of low temperature aging on strength and microstructure evolution in WN and HAZ of FSWed 7050 alloy.

6.3 Materials and Methods

The composition of aluminum alloy 7050-T7451 used in this study is listed in Table 6.1. MTI RM-1 Friction stir welding machine was used to make two welds. The welding tool consisted of 3.1 mm long step-spiral conical pin of 6.4 mm diameter tapering down to 4.5 mm and a shoulder of diameter 12 mm. Welding direction was normal to rolling direction for both welds. Tool rotation rate of 600 revolutions per minute (RPM) was the same for both welds. Tool traverse speeds for Weld1 (W1) and Weld2 (W2) were 127 millimeters per minute (mmPM) and 762 mmPM, respectively. The two traverse speeds are extremes in optimum parameters window. While 127 mmPM is generally considered ‘slow’ for FSW of aluminum alloys, 762 mmPM is ‘fast’ and may not be suitable for thicker sections. Extremes of parameters were chosen to study the effect of extremely low and high heating or cooling rates on formation of HAZ. A copper backing plate and pressurized air cooling behind the tool to enhance the cooling rate to reduce the extent of heat affected zone (HAZ) was used for both welds. The temperature profile during welding was recorded for both welds using a thermocouple inserted in the tool pin. Temperature at a location 0.6 mm below the shoulder and 0.6 mm below the weld nugget was also measured for both welds.

Table 6.1 Composition limits of key alloying elements for 7050 aluminum alloy.

Element	Zn	Mg	Cu	Zr	Mn	Ti	Si	Fe
wt.%	5.7-6.7	1.9-2.6	2.0-2.6	0.08-0.15	0.10	0.06	0.12	0.15

Mechanical property evaluation was conducted for both welds in as-welded and various post weld heat treated (PWHT) conditions. Vickers micro-hardness across the weld cross section was conducted using Wilson Tukon 1202 hardness tester. Transverse tensile testing samples with a thickness of around 3.1 mm and gauge length 32 mm were prepared according to ASTM-E8 (sub-size) standard. A minimum of 3 samples were tested for each condition.

Transmission electron microscopy (TEM) was carried out on a FEI Technai™ operating at 200kV. Electron transparent 3 mm diameter discs from selected locations were prepared using Gatan ion polishing system. Netzsch 204 F1 Phoenix® was used to perform differential scanning calorimetry (DSC) on various samples from both welds. Heating rate for all DSC measurements was 10°C per minute.

6.4 Results and Discussion

6.4.1 FSW and Temperature Measurements

Macroscopic investigation of welded cross section revealed that both welds were defect-free. Figure 6.1 shows the distinct microstructural zones formed as a result of FSW of W2 and the location of the thermocouple placed in the HAZ. Understandably, the high traverse speed used in W2 compared to W1 resulted in much finer grain size in the WN.

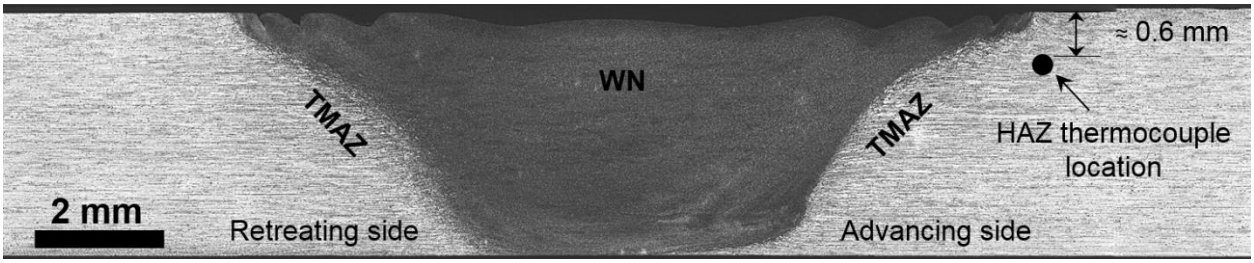

Figure 6.1 Optical macrograph showing weld cross section of W2 and HAZ thermocouple location.

Temperature evolution within the WN and HAZ during FSW of precipitation strengthened aluminum alloys impacts the final properties of the weldment [2,3,5]. Figure 6.2 shows all temperature profiles recorded at three different locations for both welds. Figure 6.2a shows tool temperature from the beginning of tool plunge to the end of welding for both welds. The inset plot in Figure 6.2a focuses on tool temperature evolution during tool traverse for both welds. Tool temperature during welding for both welds was stable around 405°C, except at the beginning part of the weld where W2 tool temperature was 10°C higher as compared to W1. For all experiments, the section of weld that experienced stable temperature was used. Figure 6.2a also indicates that peak tool temperature during FSW of aluminum alloys depends on tool rotation rate and is not affected by traverse speed. Temperature evolution at a location in HAZ and 0.6 mm below the nugget during welding was also recorded for both welds and is represented in Figure 6.2b. Figure 6.2b reveals clearly that higher tool traverse speed in W2 produced lower peak temperature in HAZ of W2 (283°C) compared to that of W1 (325°C). Figure 6.2b also shows that temperature at a location 0.6 mm below the WN was approximately the same as that of HAZ temperature for both welds. Figure 6.2c depicts heating and cooling rates experienced by the HAZ location in both welds. Understandably, both heating and cooling rates were manifold higher for W2 compared to W1. Cooling rate of 165°C per second was observed in HAZ of W2. It is apprehensible from Figure 6.2 that the extent of HAZ would be

less in W2 compared to that of W1.

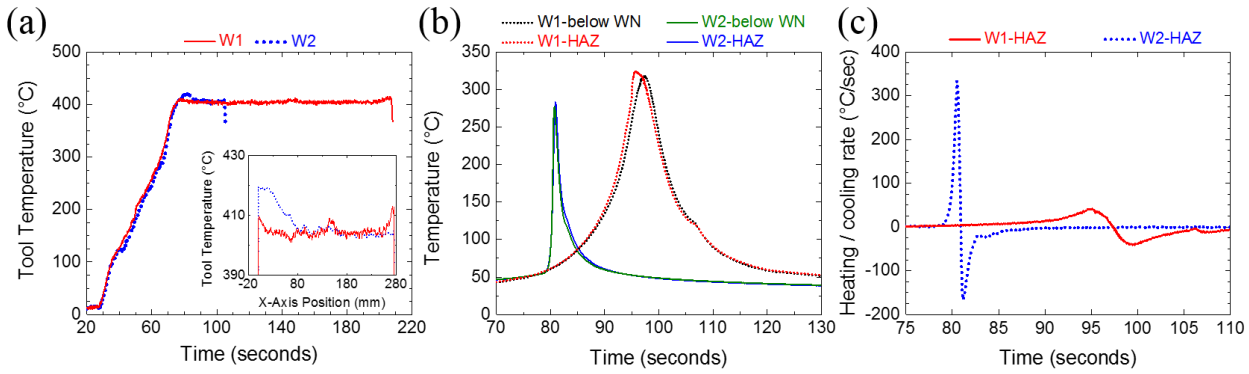

Figure 6.2. (a) Tool temperature recorded during welding for both welds, (b) temperature profiles observed at location in HAZ and below the WN in both welds, and (c) heating and cooling rate in HAZ during welding for both welds.

Vickers Microhardness Measurements

Vickers microhardness measurements for both welds in various post-weld conditions were taken at top (1 mm from top surface), middle (2 mm from top surface), and bottom (3 mm from top surface) for all samples. Figure 6.3a and Figure 6.3b show hardness results of both welds after 6 days of natural aging (AW condition). W1 hardness shows a minimum hardness of 127 HV in HAZ, and it varies from 135 HV to 145 HV in WN. Within the WN of W1, hardness decreases along the depth that is typically observed in FSW of peak aged 2XXX and 7XXX alloys [16]. W2 showed a nearly flat hardness profile in HAZ and WN where it wavered between 137-145 HV (Figure 6.3b). Coarsening of precipitates in HAZ is well-known to result in deterioration in mechanical properties. Higher HAZ hardness in W2 compared to W1 is a consequence of lower temperature in HAZ of W2. Also, due to higher traverse speed, HAZ of W2 experienced high temperature for lesser time compared to that of HAZ of W1 and would have resulted in a lesser coarsening in HAZ of W2. Hardness along the depth of the weld in WN of W2 in AW condition did not show any typically observed trend, and it fluctuated around 140

HV. Samples from both welds were subjected to a typical T6 heat treatment for 7XXX alloys during which samples were held for 24 hours at 121°C in a forced air oven. Hardness results for both welds after T6 heat treatment were explicitly different from each other, as shown in Figure 6.3c and Figure 6.3d. Hardness at the top of WN of W1 improved by around 10 HV and remained nearly the same for the middle of WN; whereas it decreased by nearly 10 HV in the bottom part of WN of W1. In the case of W2, hardness in the entire WN improved. Hardness in the top of WN increased by 30-35 HV from AW condition. Hardness in the bottom of WN increased by 5-10 HV. HAZ of W1 after T6 heat treatment showed a further decrease in hardness at all three measurement locations as compared to AW condition. In the HAZ of W2, hardness improved in top and middle locations and decreased by 3-4 HV at the bottom. Such results in HAZ of W2 after T6 heat treatment are due to very high traverse speed used in W2. Figure 6.3 shows clearly that even very high cooling rates of 160°C/sec in HAZ of W2 could prevent the formation of HAZ. The residence time for temperature higher than 150°C in HAZ of W2 was merely 1.8 seconds (Figure 6.2b). Thus the conclusion is that formation of HAZ during FSW of 7XXX alloy is inevitable.

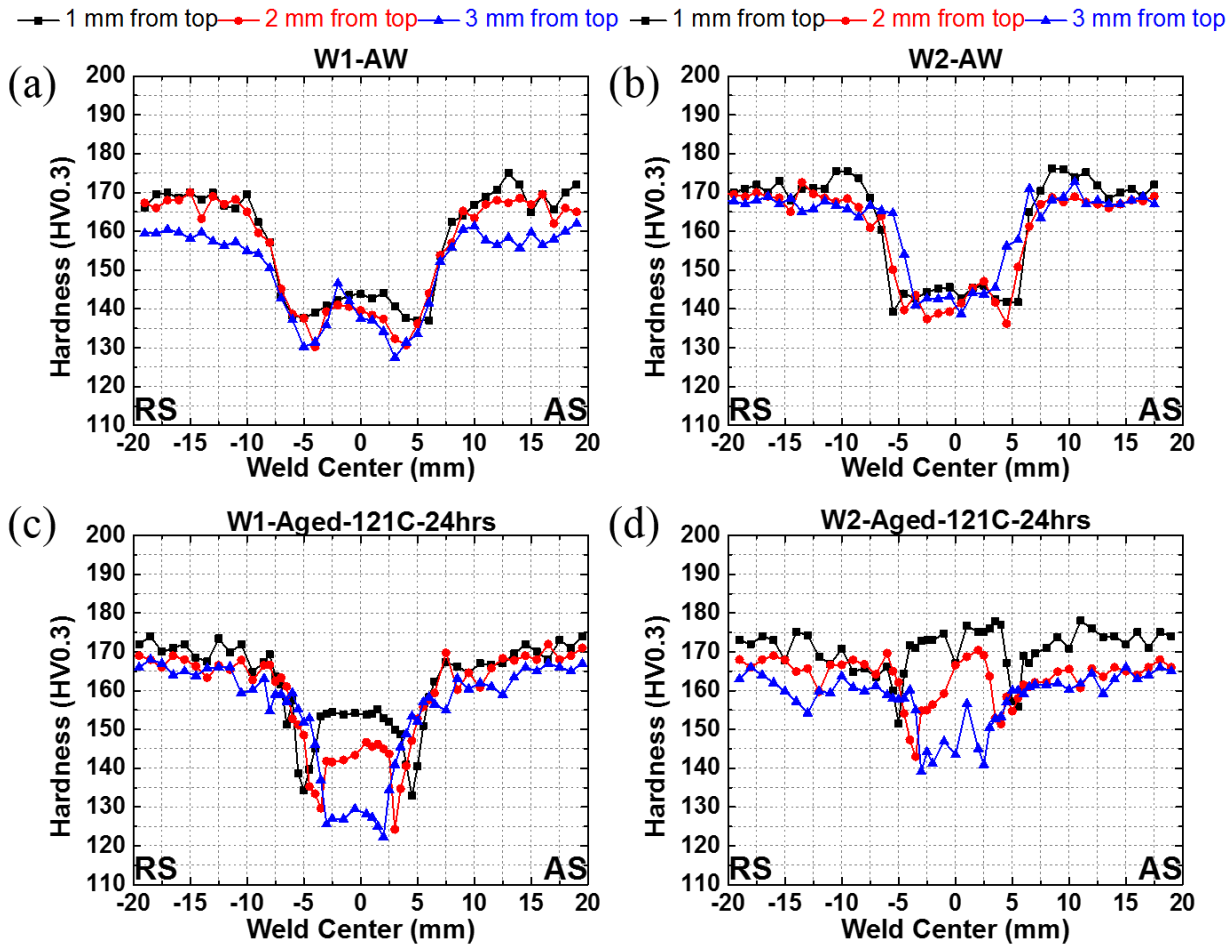

Figure 6.3 Vickers microhardness measurements taken at three different locations in (a) W1 sample in AW condition, (b) W2 sample in AW condition, (c) W1 sample aged for 24 hours at 121°C, and (d) W2 sample aged for 24 hours at 121°C.

As discussed in the Introduction, aging at low temperatures as compared to standard PWHT can suppress the rate of coarsening of pre-existing precipitates and enhance nucleation density. Hence, samples from both welds were subjected to aging at 85°C for 244 hours. Temperature for low temperature aging was chosen based on the fact that GPII zones in 7XXX alloys form at temperatures above 70°C [12]. GP zones are not thermally stable at higher temperatures. So 85°C was chosen for low temperature aging to achieve strengthening due to transformation of GP zones to precipitates unlike natural aging, where the majority of the

strength is due to GP zones formation. Time for aging at 85°C was calculated by using classic Arrhenius law for diffusion described by the equation:

$$D = D_0 \exp(-Q/RT)$$

where D_0 is the pre-exponential factor and Q is the activation barrier for diffusion. Time was calculated by equating the diffusional distance for Mg atoms at 85°C to diffusion at 121°C for 24 hours. The values for pre-exponential factor and activation barrier were taken from elsewhere [13].

Figure 6.4a and Figure 6.4b show hardness results obtained after samples from both welds were subjected to 85°C heat treatment for 244 hours. Hardness results after low temperature aging at 85°C show improved strength in both HAZ and WN for both welds. Owing to its high traverse speed, improvement in hardness in W2 was much higher as compared to that of W1. Hardness at top of WN of W1 increased 20 HV as compared to AW condition; whereas hardness at top of WN of W2 increased by 40 HV. Unlike T6 treated samples, low temperature aging did not produce deterioration of hardness in HAZ of W1. HAZ hardness improved by 10 HV in bottom and 18 HV in top of W1 after 85°C aging treatment. Hardness in HAZ of W2 also improved significantly by top of W2 approaching base material hardness (165-170 HV) of 7050-T7451. Samples from both welds were left at room temperature for natural aging for another low temperature analysis. Figure 6.4c and Figure 6.4d show hardness results of samples of W1 and W2 after natural aging of approximately 5500 hours. Recovery of hardness due to natural aging with time in friction stir welded (FSWed) 7050 alloy has been studied by Fuller and his co-workers [10]. Precipitation of a high volume fraction of GP zones and a smaller volume fraction of η′ precipitates in WN and HAZ during natural aging was ascertained for strength recovery in FSWed 7050 alloy. Hardness in both welds after 5500 hours of natural aging showed trends

similar to results from 85°C aging experiment. Hardness improved in both WN and HAZ of both welds after natural aging. Interestingly, the difference in hardness between top and bottom of the weld for both W1 and W2 was much less compared to results from other aging treatments.

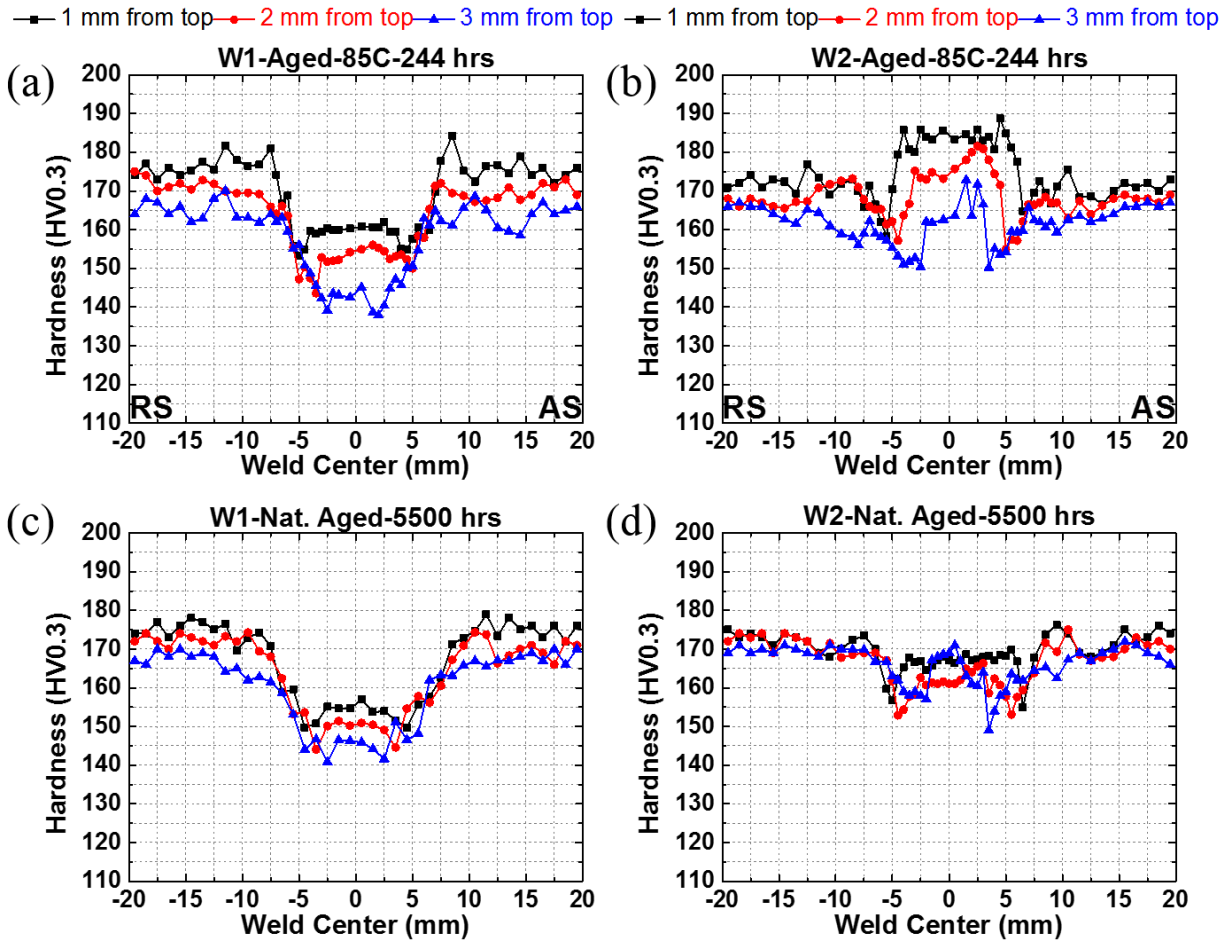

Figure 6.4 Vickers microhardness measurements taken at three different locations in (a) W1 sample aged for 244 hours at 85°C, (b) W2 sample aged for 244 hours at 85°C, (c) W1 sample naturally aged for 5500 hours, and (d) W2 sample naturally aged for 5500 hours.

Uniaxial Tensile Testing

Uniaxial tensile testing results of samples from both welds in all conditions are shown in Table 6.2. Yield strength (YS), ultimate tensile strength (UTS), and elongation to failure were calculated for each condition. Joint efficiency (JE) based on YS and UTS was also calculated for

specimens in each condition. AW samples were tested after natural aging of approximately 72 hours. In all test conditions, joint strength of both welds showed trends similar to hardness results. High cooling rates in WN and HAZ (Figure 6.2c) of W2 due to higher traverse speed reduced mechanical property degradation in all specimens tested in various post weld conditions. In AW condition, JE of W2 (84% of BM YS) was 9-10% higher compared to that of W1 (75% of BM YS). Both T6 heat treatment at 121°C and low temperature aging at 85°C resulted in improved strength level of both welds. W2 weld showed 100% JE after being subjected to low temperature aging as compared to 91% YS based JE for W1in case of W1. Naturally aged specimens also showed improvement in strength for both welds. Elongation to failure of FSWed joints of 7XXX alloys is usually lower as compared to BM ductility. This is due to severe strain localization occurring in the gauge length of tensile sample during tension test. Strain localization is the response of composite microstructure within gauge length consisting of WN, TMAZ, HAZ, and BM to the tension test. During tensile test, deformation quickly localizes to the weakest region and is then followed by necking of that region. Such deformation leads to overall low values of elongation to failure in case of tensile testing of FSWed specimens. Low temperature aging at 85°C decreased the difference in hardness of weakest zone and BM and improved elongation to failure as compared to AW and T6 heat treatment condition as shown in Table 6.2.

Table 6.2 Tensile testing results of specimens of both the welds in various post weld conditions.

Sample	YS (MPa)	UTS (MPa)	Total elongation (%)	JE (%)	
				YS	UTS
BM	476±8	541±8	11.5±2.1	-	-
W1-AW	359±4	461±2	7.1±0.5	75	85

W2-AW	404±3	515±3	6.4±0.4	84	95
W1-121°C-24 hours	400±1	470±1	6.2±0.7	84	87
W2-121°C-24 hours	459±1	525±1	7.1±0.1	96	97
W1-85°C -244 hours	436±1	516±2	8.3±0.7	91	95
W2-85°C -244 hours	477±1	542±2	8.7±0.1	100	100
W1-NA-5600 hours	417±9	516±8	6.9±0.5	88	95
W2-NA-5600 hours	456±9	538±8	6.4±0.7	97	100

6.4.2 DSC Analysis

DSC has been used extensively to study the precipitation behavior of precipitation strengthened aluminum alloys [8]. Amplitude of a peak and area under a peak in a DSC plot relates to propensity of precipitation and its volume fraction [8,10,22,23]. For the same alloy composition and heating rate during DSC experiment, peak temperature can be related to precipitate size and stability [10,23]. DSC experiments were conducted to study the effect of FSW and aging treatments on precipitation and dissolution of various phases in both welds. Figure 6.5a shows DSC results for samples from WN and HAZ of both welds. For comparison, DSC result of BM sample is also shown in Figure 6.5a-c. In Figure 6.5a, Peak A is due to dissolution of GP zones, B corresponds to the dissolution of η′ precipitate, exothermic peak C is due to formation of η precipitate, and peak D spanning approximately from 330°C to 430°C is the dissolution effect of η [23]. E is a convoluted peak referred to the formation and dissolution of high temperature phases such as S and T phase [23]. Sharp peak F is due to melting of S phase [23]. All WN and HAZ samples referred to in Figure 6.5a were tested with fewer than 72 hours of natural aging and hence a very small signature (peak A) of GP zone dissolution was observed.

In Figure 6.5a, a larger peak C for WN of W1 compared to that of W2 shows that dissolution of precipitates during welding was more efficient in W1 as compared to W2 and can be attributed to the higher heat content in W1 due to slower traverse speed. Similarly, peak C for HAZ of W1 is larger due to the higher heat content experienced by W1 during welding (Figure 6.2b). For samples from a particular weld (W1 or W2), smaller peak C and larger peak D for HAZ sample as compared to peaks in WN sample, point to the coarsening of η precipitate in HAZ. Further confirmation is evidenced by the unaltered nature of peaks (E and F) corresponding to high temperature phases for samples from HAZ, which proves that there was insignificant solute migration to coarse T or S phases; whereas in case of samples from WN, peaks E and F were de-convoluted. This suggests that large strain and temperature (405°C) during FSW altered the microstructure to promote the formation of high volume fraction of η precipitate and small amount of high temperature phases. Peak C for sample from HAZ of W2 is smaller compared to that of HAZ of W1. In accordance with temperature data and hardness results, the extent of coarsening of η precipitate proved to be very less in W2 as compared to W1.

Figure 6.5b shows the DSC results of samples taken from WN of W1 in different post weld conditions. Sample in AW condition and naturally aged (NA) for 5000 hours showed GP zone dissolution peak (A) which was absent in samples aged at 85°C and 121°C. η′ precipitate dissolution (peak B) observed in samples aged at 85°C and 121°C confirms that strength recovery obtained in case of samples aged at 85°C was due to the formation of strengthening precipitates. η′ precipitate dissolution peak shifted to lower temperature in case of sample aged at 85°C as compared to one aged at 121°C. Such shift indicates that average η′ precipitate size in sample aged at 85°C was smaller compared to that of BM and sample aged at 121°C. Precipitation of η phase (peak C) was observed in all conditions. Interestingly, for samples aged

at 85°C and 121°C, peak C decomposed into two distinct peaks labelled as C1 and C2. Figure 6.5b shows clearly that peak C in case of BM sample more resembled peak C2. BM sample was in overaged (T7451 temper) condition. During the DSC experiment of BM sample, the very small amount of precipitation of η phase will be due to the concurrent dissolution of η′ precipitate (peak B). Therefore, we deduced that the majority of peak C (or C2) for BM sample is due to coarsening of pre-existing η precipitates in overaged BM. C1 is due to the homogenous precipitation of η phase in matrix and C2 is coarsening of high stability η precipitates on defects such as dislocations and grain boundaries. The presence of peak C2 in samples aged at 85°C and 121°C clearly shows that significant coarsening of η precipitates happened during post weld aging. DSC result of sample aged at 121°C showed a broader C2 peak whereas in case of sample aged at 85°C, C2 was merging with C1. All this indicates that the extent of coarsening was higher during aging at 121°C as compared to 85°C.

Figure 6.5c shows the DSC results of samples from HAZ of W1 in various post weld conditions. Clearly, HAZ samples did not reveal any splitting of peak C. However, hardness measurements showed knockdown in strength in HAZ region of samples aged at 121°C, which is known to be due to coarsening of precipitates. Since temperature in HAZ of W1 was not sufficiently high to dissolve all pre-existing precipitates, very few solutes are available for formation of new precipitates. It is also confirmed from the small amplitude of η′ dissolution event (peak B) in HAZ as compared to WN samples (Figure 6.5a). No separation of events in peak C in any of the HAZ samples is because unlike WN, HAZ does not go through dissolution; and the extent of both precipitation and growth or coarsening in HAZ is much smaller as compared to samples from WN. Also, high heating rates (600°C per hour) during DSC experiments cannot reveal such events occurring with very low intensity.

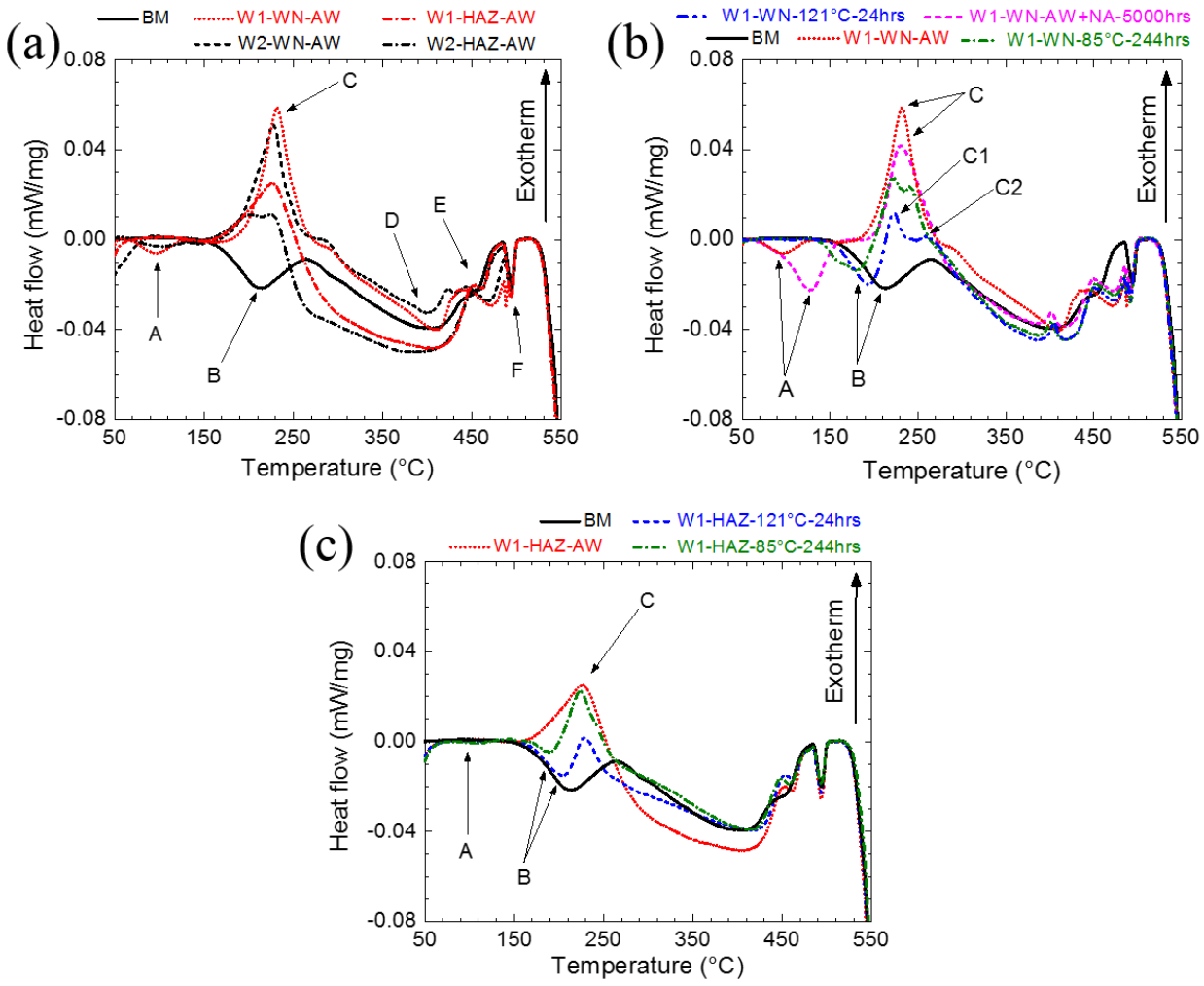

Figure 6.5 DSC results of (a) samples from WN and HAZ of both the welds in AW condition, (b) samples from WN of W1 in different aging conditions, and (c) samples from HAZ of W1 in different aging conditions compared to BM.

TEM Analysis

7XXX aluminum alloys have a complex precipitation behavior and sequence. Industrially, various thermomechanical and multi-step aging treatments are used to achieve a combination of strength and other mechanical properties. The main strengthening precipitates on defect structures and grain boundaries in 7050-T7451 alloy are η′ ($Mg(Zn, Cu)_2$) formed within the matrix and η ($MgZn_2$) formed in grain interior [11,12,17,24]. In BM, homogeneously

distributed precipitates of size less than 50 nm were observed in the grain interior (Figure 6.6a). In addition, coarse grain boundary (GB) precipitates as compared to matrix precipitates were also observed (Figure 6.6b). Also, PFZ with a width 20-30 nm was observed along the grain boundaries. Selected area diffraction pattern (SADP) shown in Figure 6.6c confirms the presence of η′, η, and GP zones.

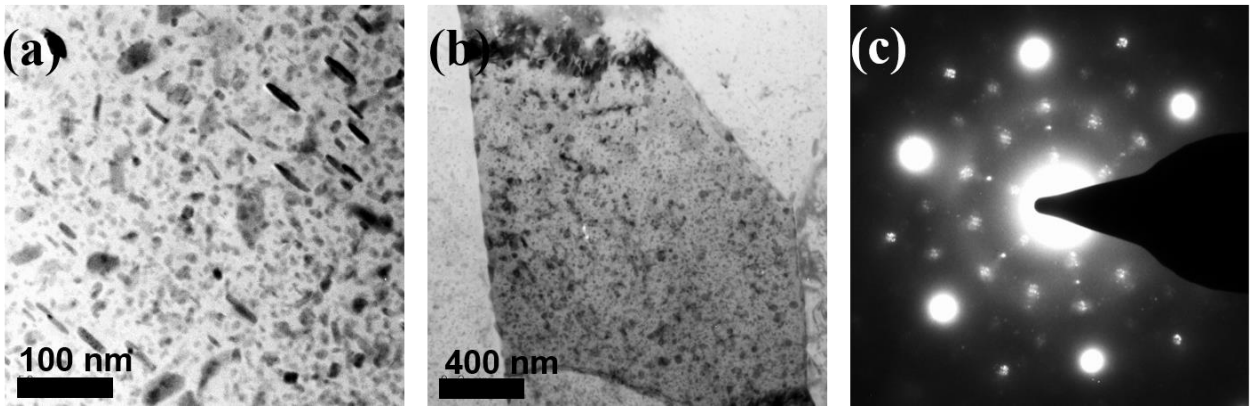

Figure 6.6(a) and (b) show bright field TEM microgragh of a sample from BM 7050-T7451 and (c) shows the SADP of area in (a) along [111].

Figure 6.7a-d show TEM images from samples of WN of both the welds in AW condition. During FSW, although high temperature and strain dissolve the existing precipitates to form a SSSS in the WN, cooling rate behind the tool can greatly influence the post weld microstructure. In W1, where cooling rates were low, WN microstructure in AW condition consisted of coarse precipitates on GB, subgrain boundary, and dislocation structures as shown in Figure 6.7a and Figure 6.7b. In case of W2, 6 times higher tool traverse speed compared to W1 generated high cooling rates. The result was a microstructure with significantly less re-precipitation during cooling of weld (Figure 6.7d). Very few GB precipitates were observed in WN of W2 in AW condition. In addition, Figure 6.7c and Figure 6.7d reveal that high cooling rates in W2 were sufficient to retain high dislocation density after a hot deformation process. High dislocation density and quenched-in vacancies can accelerate the formation of GP zones

and precipitates during PWHT; whereas slow cooling rates in W1 were insufficient to retain defect structures formed at high temperature and produced relatively dislocation-free grains (Figure 6.7a and Figure 6.7b).

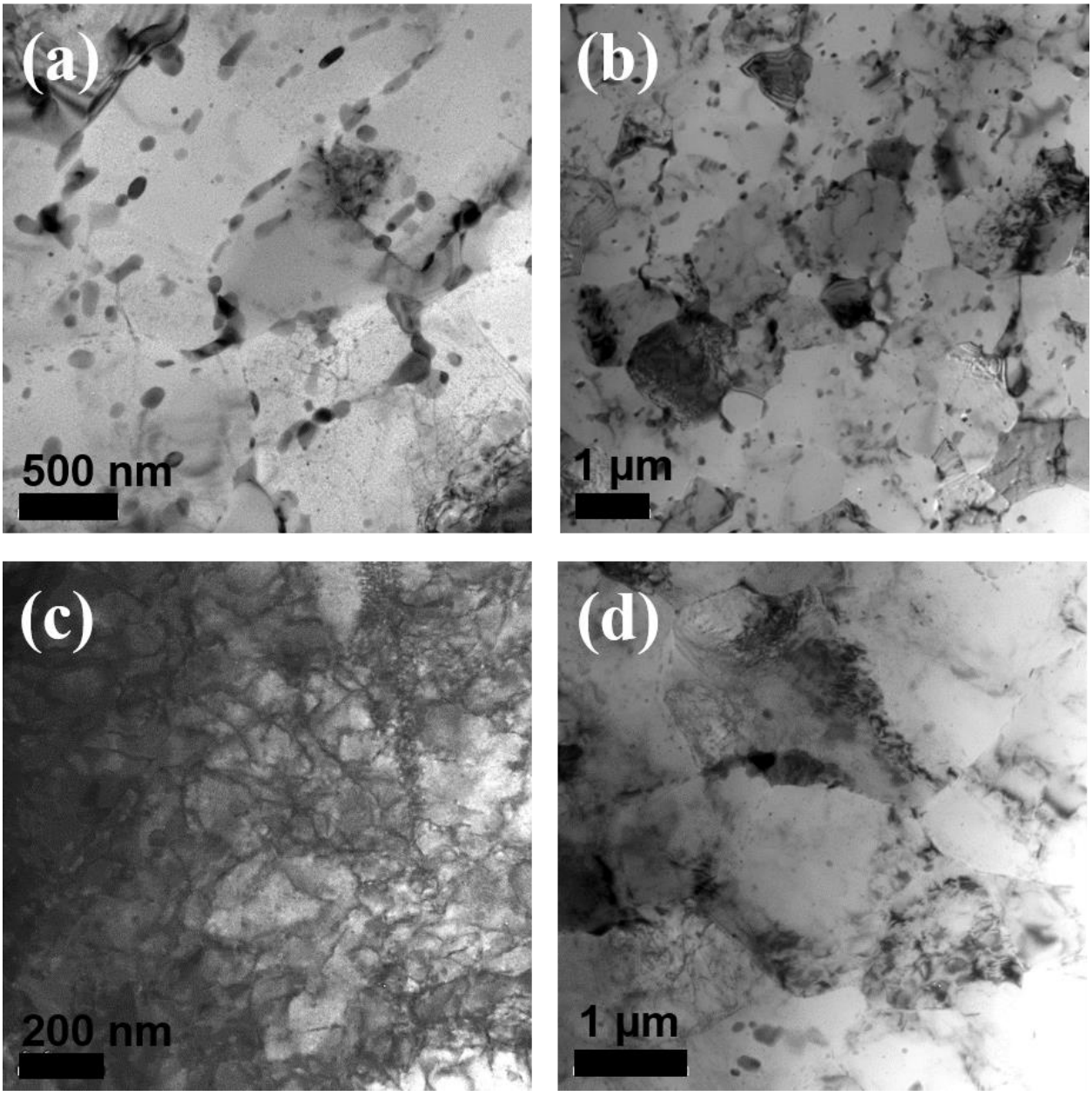

Figure 6.7(a) and (b) Bright field TEM micrograph of a sample from WN of W1 in AW condition, (c) and (d) TEM micrograph of a sample from WN of W2 in AW condition.

PWHT at 121°C for 24 hours resulted in contrasting hardness results in WN of both

welds. Results of TEM investigations of WN of both welds after T6 PWHT are shown in Figure 6.8. WN of W1 showed further coarsening of GB and matrix precipitates that re-precipitated during cooling of weld as evident from Figure 6.8a. As discussed earlier, growth or coarsening rates are expected to be large at high aging temperatures. At some locations away from GB, fine precipitates in grain interior of WN of W1 were also observed (Figure 6.8b). These precipitates were formed as a result of T6 PWHT. WN of W2, where strength improved to the level of BM, showed lesser coarsening of GB precipitates (Figure 6.8c). Also, homogeneously distributed precipitates were observed in grain interior as shown in Figure 6.8d.

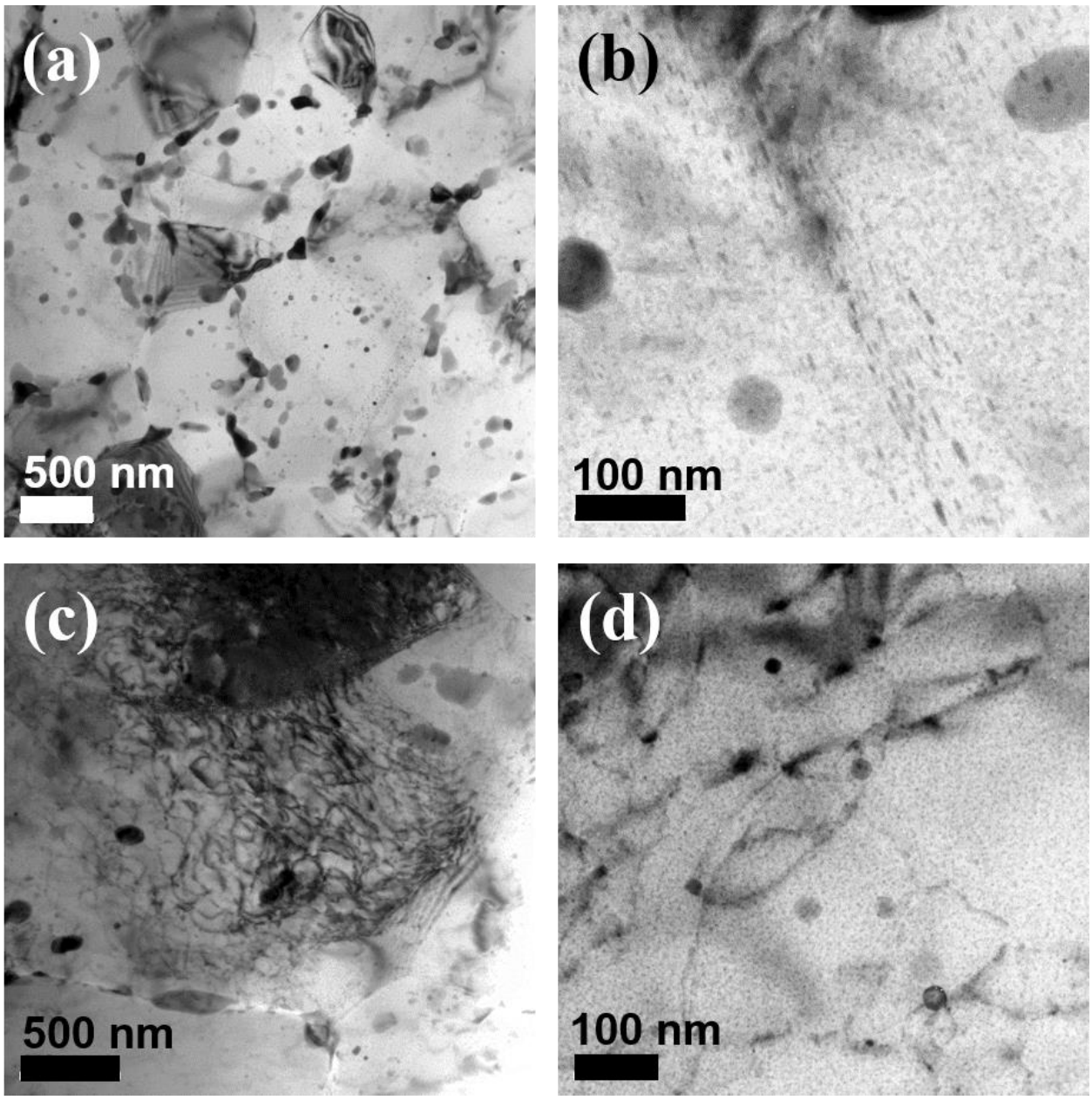

Figure 6.8(a) and (b) TEM micrographs of a sample from WN of W1 aged for 24 hours at 121°C, (c) and (d) TEM micrographs of a sample from WN of W2 aged for 24 hours at 121°C.

Figure 6.9 shows TEM images of WN of W1 aged at 85°C for 244 hours. Dense and homogeneously distributed precipitates of size less than 8 nm were formed in the matrix of WN of W1 aged at 85°C for 244 hours (Figure 6.9b). Size of coarse GB precipitates and PFZ was significantly reduced as compared to T6 PWHT condition (Figure 6.9a). SADP (Figure 6.9c) of

area shown in Figure 6.9b confirmed that the precipitates were η′, η, and dispersoid Al_3Zr [25,26]. Similarly, extremely fine-scale precipitation of η′ and η precipitates was observed in W2 aged at lower temperature (Figure 6.10).

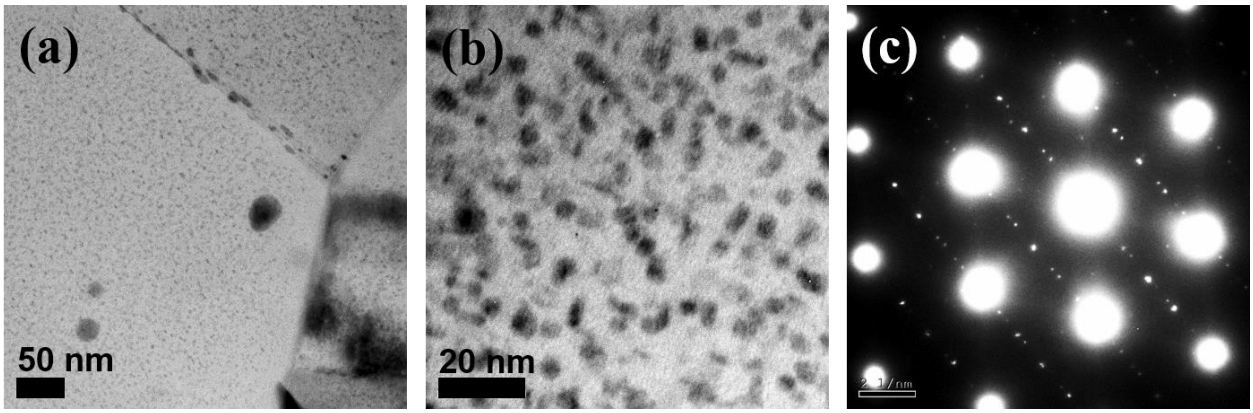

Figure 6.9(a) and (b) TEM micrographs of a sample from WN of W1 aged for 244 hours at 85°C, (c) SADP of area shown in (b) along [110].

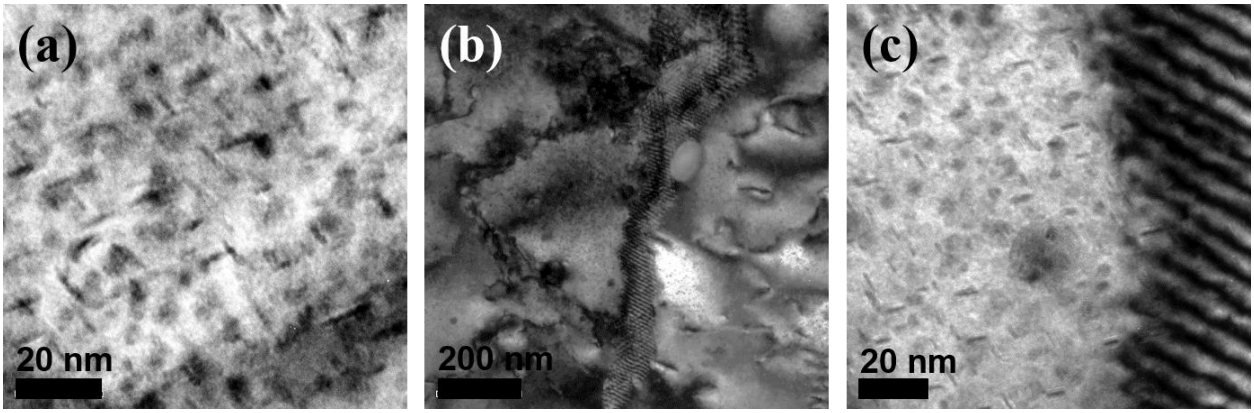

Figure 6.10 TEM micrographs of a sample from WN of W2 aged for 244 hours at 85°C.

Apart from typical microstructural zones produced in FSW, peak temperature and cooling rate are critical to final microstructure and properties of the weldment. FSW results in complete supersaturated solid solution in WN. After welding, if the cooling rates are low such as in W1, solutes may migrate to grain boundaries (or other defect structures) and form coarse matrix and GB precipitates. Post-weld aging of such microstructure at conventionally used high temperatures (120-160°C) results in extensive coarsening of precipitates. HAZ forms where the

peak temperature during FSW is in the range of highest coarsening rate. HAZ experiences even more widespread coarsening of pre-existing precipitates during post-weld aging at high temperatures. Aging at lower temperatures (or natural aging) and higher cooling rates during welding, such as in case of W2, significantly reduces the coarsening of pre-existing precipitates and promotes nucleation of new precipitates. Aging at lower temperatures also improves overall ductility of the weldment as the strain localization reduces with a uniformity in hardness distribution across the weld cross section. As realized from hardness, tensile, and DSC results, room temperature aging does improve the strength of weldment eventually to the level of BM strength, but most of the strength recovery is due to the formation of GP zones (Figure 6.5). Fuller et al. [10] also observed that the majority of the strength recovery in FSWed 7050 and 7075 alloy after natural aging of 8-9 years was due to formation of GP zones. At room temperature, GP zones transform into metastable η′ precipitates after extremely long aging hours; whereas strength recovery in case of aging at 85°C was due to the formation of η′ precipitates.

6.5 Conclusion

A systematic experimental approach using mechanical testing, DSC analysis, and electron microscopy was conducted to study strength recovery during low temperature aging of FSWed 7050-T7451 alloy. The study leads to the following conclusions:

1. Presence of HAZ in W2 (traverse speed 762 mmPM), where cooling rates were over 160°C/sec, proves that formation of HAZ in FSW of 7050-T7451 alloy cannot be avoided.
2. Standard T6 PWHT at 121°C for 24 hours results in further loss of strength in HAZ due to continuation of coarsening of pre-existing precipitates.
3. Low temperature aging at 85° leads to significant strength improvement in HAZ and WN as compared to standard T6 PWHT. Hardness in WN of weld made with traverse speed of 762

mmPM was higher than BM hardness. High retained dislocation density and solutes in solid solution due to high cooling rate during welding were reasoned for higher hardness.

4. DSC analysis and TEM investigations lead to the conclusion that strength recovery during low temperature aging was due to precipitation of strengthening phase η′ unlike GP zone-based strength recovery during natural aging.
5. Homogeneous distribution of both η′ and η precipitates of size less than 8 nm was observed in both welds after 85°C PWHT.
6. Joint strength of 100% of BM strength was achieved in weld made with 762 mmPM traverse speed and subjected to 85°C PWHT. However, 95% joint efficiency was recorded for weld made with rather conservative traverse speed of 127 mmPM.

Acknowledgments

This work was supported by Center for Friction Stir Processing (CFSP) at University of North Texas, United States. The authors acknowledge the UNT Center for Advanced Research and Technology (CART) for microscopy facilities.

6.6 References

[1] T. Dursun, C. Soutis, Recent developments in advanced aircraft aluminium alloys, Mater Des. 56 (2014) 862-871.

[2] R.S. Mishra, Z. Ma, Friction stir welding and processing, Materials Science and Engineering: R: Reports. 50 (2005) 1-78.

[3] R.S. Mishra, P.S. De, N. Kumar, Friction Stir Welding and Processing: Science and Engineering, Springer, 2014.

[4] W. Thomas, E. Nicholas, J. Needham, M. Murch, P. Templesmith, C. Dawes, International patent application no. (1991).

[5] R.S. Mishra, M.W. Mahoney, Friction Stir Welding and Processing, ASM International, 2007.

[6] A. Sullivan, J. Robson, Microstructural properties of friction stir welded and post-weld heat-treated 7449 aluminium alloy thick plate, Materials Science and Engineering: A. 478 (2008) 351-360.

[7] J. Su, T.W. Nelson, C.J. Sterling, Microstructure evolution during FSW/FSP of high strength aluminum alloys, Materials Science and Engineering: A. 405 (2005) 277-286.

[8] M. Starink, Analysis of aluminium based alloys by calorimetry: quantitative analysis of reactions and reaction kinetics, International Materials Reviews. 49 (2004) 191-226.

[9] N. Kamp, A. Sullivan, J. Robson, Modelling of friction stir welding of 7xxx aluminium alloys, Materials Science and Engineering: A. 466 (2007) 246-255.

[10] C.B. Fuller, M.W. Mahoney, M. Calabrese, L. Micona, Evolution of microstructure and mechanical properties in naturally aged 7050 and 7075 Al friction stir welds, Materials Science and Engineering: A. 527 (2010) 2233-2240.

[11] J. Buha, R.N. Lumley, A.G. Crosky, Secondary ageing in an aluminium alloy 7050, Materials Science and Engineering: A. 492 (2008) 1-10.

[12] L.K. Berg, J. Gjønnes, V. Hansen, X.Z. Li, M. Knutson-Wedel, G. Waterloo, D. Schryvers, L.R. Wallenberg, GP-zones in Al–Zn–Mg alloys and their role in artificial aging, Acta Materialia. 49 (2001) 3443-3451.

[13] N. Kamp, A. Sullivan, R. Tomasi, J. Robson, Modelling of heterogeneous precipitate distribution evolution during friction stir welding process, Acta materialia. 54 (2006) 2003-2014.

[14] R. Brown, W. Tang, A.P. Reynolds, Multi-pass friction stir welding in alloy 7050-T7451: effects on weld response variables and on weld properties, Materials Science and Engineering: A. 513 (2009) 115-121.

[15] M. Dumont, A. Steuwer, A. Deschamps, M. Peel, P. Withers, Microstructure mapping in friction stir welds of 7449 aluminium alloy using SAXS, Acta materialia. 54 (2006) 4793-4801.

[16] K. Jata, K. Sankaran, J. Ruschau, Friction-stir welding effects on microstructure and fatigue of aluminum alloy 7050-T7451, Metallurgical and materials transactions A. 31 (2000) 2181-2192.

[17] A.P. Reynolds, W. Tang, Z. Khandkar, J.A. Khan, K. Lindner, Relationships between weld parameters, hardness distribution and temperature history in alloy 7050 friction stir welds, Science and Technology of Welding and Joining. 10 (2005) 190-199.

[18] C. Rhodes, M. Mahoney, W. Bingel, M. Calabrese, Fine-grain evolution in friction-stir processed 7050 aluminum, Scr. Mater. 48 (2003) 1451-1455.

[19] F. Rui-Dong, S. Zeng-Qiang, S. Rui-Cheng, L. Ying, L. Hui-jie, L. Lei, Improvement of

weld temperature distribution and mechanical properties of 7050 aluminum alloy butt joints by submerged friction stir welding, Mater Des. 32 (2011) 4825-4831.

[20] J. Su, T. Nelson, R. Mishra, M. Mahoney, Microstructural investigation of friction stir welded 7050-T651 aluminium, Acta materialia. 51 (2003) 713-729.

[21] R. Lumley, I. Polmear, A. Morton, Interrupted aging and secondary precipitation in aluminium alloys, Materials science and Technology. 19 (2003) 1483-1490.

[22] M. Starink, Effect of compositional variations on characteristics of coarse intermetallic particles in overaged 7000 aluminium alloys, Materials science and technology. 17 (2001) 1324-1328.

[23] X. Li, M. Starink, DSC study on phase transitions and their correlation with properties of overaged Al-Zn-Mg-Cu alloys, Journal of materials engineering and performance. 21 (2012) 977-984.

[24] A. Deschamps, F. Livet, Y. Brechet, Influence of predeformation on ageing in an Al–Zn–Mg alloy—I. Microstructure evolution and mechanical properties, Acta Materialia. 47 (1998) 281-292.

[25] A. Deschamps, Y. Brechet, Nature and distribution of quench-induced precipitation in an Al-Zn-Mg-Cu alloy, Scr. Mater. 39 (1998) 1517-1522.

[26] W. Yang, S. Ji, M. Wang, Z. Li, Precipitation behaviour of Al–Zn–Mg–Cu alloy and diffraction analysis from η′ precipitates in four variants, J. Alloys Compounds. 610 (2014) 623-629.

CHAPTER 7

OVERALL CONCLUSION AND FUTURE DIRECTIONS

7.1 Conclusion

The major difference between the production of 2XXX and 7XXX aluminum alloys, apart from stress relieving processes, is the deformation introduced to 2XXX alloys after quenching from solution heat treatment [1]. This difference is recognized by the temper designation associated with the alloy. Generally, 2XXX alloys are produced and used in T3 or T8 (rarely in T6) tempers whereas 7XXX alloys usually find application in T6 or T7 tempers [1]. 2XXX alloys are known to benefit from deformation prior to artificial aging [1-3]. Presence of dislocations enhances the nucleation and growth of main strengthening precipitates (T1, θ′, and S) in 2XXX alloys (Figure 7.2) [1-3]. Unlike 2XXX alloys, 7XXX alloys are not subjected to deformation prior to aging as the main strengthening phase (η′) does not benefit from presence of defect structures. In fact, stable and less potent strengthening phase (η) in 7XXX alloys favorably nucleates on dislocations and grain boundaries [4]. Thus introduction of deformation in 7XXX alloys may lead to decrease in peak strength.

Friction stir welding (FSW) is a high temperature process in which deformation of material takes place at a temperature in the range of 0.6-0.8 T_m (melting temperature of aluminum) in case of aluminum alloys [5-7]. Weld nugget (WN) undergo recrystallization and forms fine equiaxed grains with low dislocation density [5-7]. Aluminum has high rate of recovery due to its high stacking-fault energy and hence retained dislocation density after FSW in aluminum alloys is usually low [5-7]. Therefore, the resultant microstructure of WN is equivalent to T4 temper (Figure 7.1) as it goes through solution treatment during FSW and stabilization at room temperature after cooling. The degree of solutionization in WN depends on peak temperature and

cooling rate during welding and thus, are the controlling factors for efficiency of T4 temper of WN. Post weld heat treatment (PWHT) of WN results in T6 microstructure. T6 temper is peak strength microstructure in case of 7XXX alloys. Therefore, as shown in the results of FSW of 7050 alloy, peak strength can be achieved in FSWed 7XXX after PWHT. On the other side, T6 microstructure usually does not produce peak strength in 2XXX alloys (Figure 7.2). Hence, as observed in results of FSW of various Al-Cu-Li alloys, strength equivalent to base material (T8 temper) cannot be achieved in FSWed 2XXX alloys.

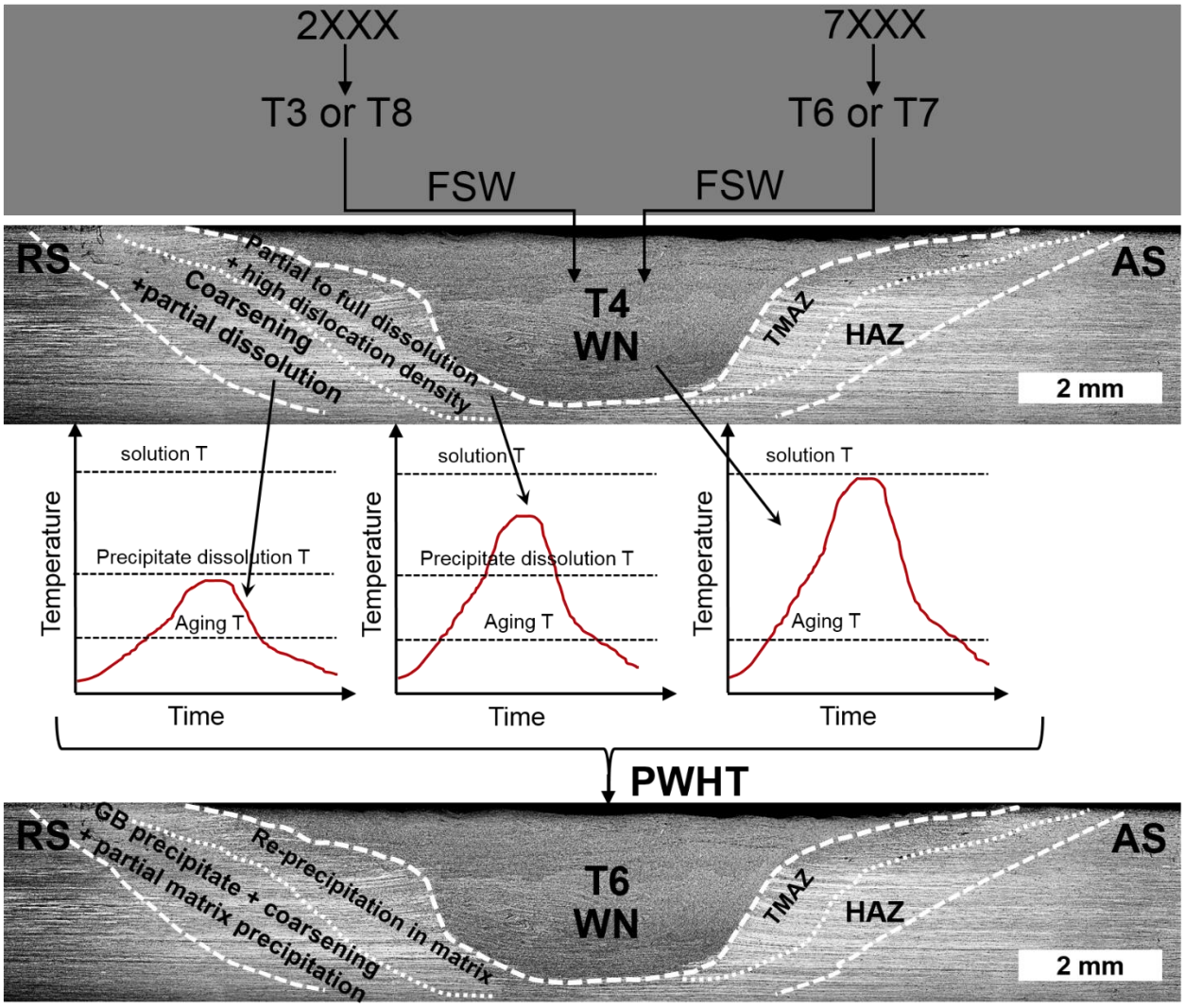

Figure 7.1 Schematic showing overall microstrucutral evolution in 2XXX and 7XXX alloys during FSW and after post weld heat treatment.

Thermo-mechanically affected zone (TMAZ) is the transition zone between WN and parent material [5-7]. It experiences plastic deformation and thus dislocation density is usually high [5-7]. Partial recrystallization may occur in some grains close to WN due to high temperature and strain. As shown in the schematic in Figure 7.1, the peak temperature in this zone is usually high enough for partial to full dissolution of precipitates [5-7]. Although the peak temperature is high enough to dissolve strengthening precipitates, but high temperature stable precipitates may not dissolve. Coarsening of such precipitates during cooling of weld results in loss of solute from solid solution. Presence of dislocations in this zone results in efficient re-precipitation of strengthening precipitates in case of 2XXX alloys during PWHT.

Heat affected zone (HAZ) forms in parent material away from WN where thermal cycle is in the coarsening regime of strengthening precipitates [5-7]. This zone only experiences thermal cycle [5-7] and as shown in the schematic in Figure 7.1, the temperature is usually well above aging temperature and below the solvus of precipitates. Partial dissolution and coarsening of strengthening precipitates and other phases takes place in this zone. During PWHT at standard temperature (industrially practiced), further coarsening of pre-existing precipitates occurs. Solute loss to grain boundary to form grain boundary precipitates and widened precipitate free zone (as compared to base material) are also observed in this zone [8]. Use of external cooling medium can reduce the extent of HAZ formation as observed in the results of underwater FSW of Al-Cu-Li alloy. As shown in the case of FSW of 7050 alloy, high welding speed also reduce the coarsening in HAZ and thus reduces the loss in strength in HAZ. In certain cases, aging at temperature much lower than standard temperature can also be used to improve the strength in HAZ and is discussed later in this chapter in greater detail.

Deformation prior to aging increase the aging kinetics in Al-Cu-Li alloys (or 2XXX

alloys) as shown in Figure 7.2. FSW results in a composite microstructure as shown in Figure 7.1. Although near peak strength in WN can be achieved by aging for longer hours, but it would result in extensive coarsening in HAZ leading to further knockdown in strength in HAZ. Longer aging hours also leads to over-aging in parent material and loss of ductility in the entire weldment. It is clear from Figure 7.2 that in third generation Al-Cu-Li alloys, the maximum strength achievable in WN (T4) using standard PWHT lies in the range of 75-85% of the peak strength of parent material T8 temper.

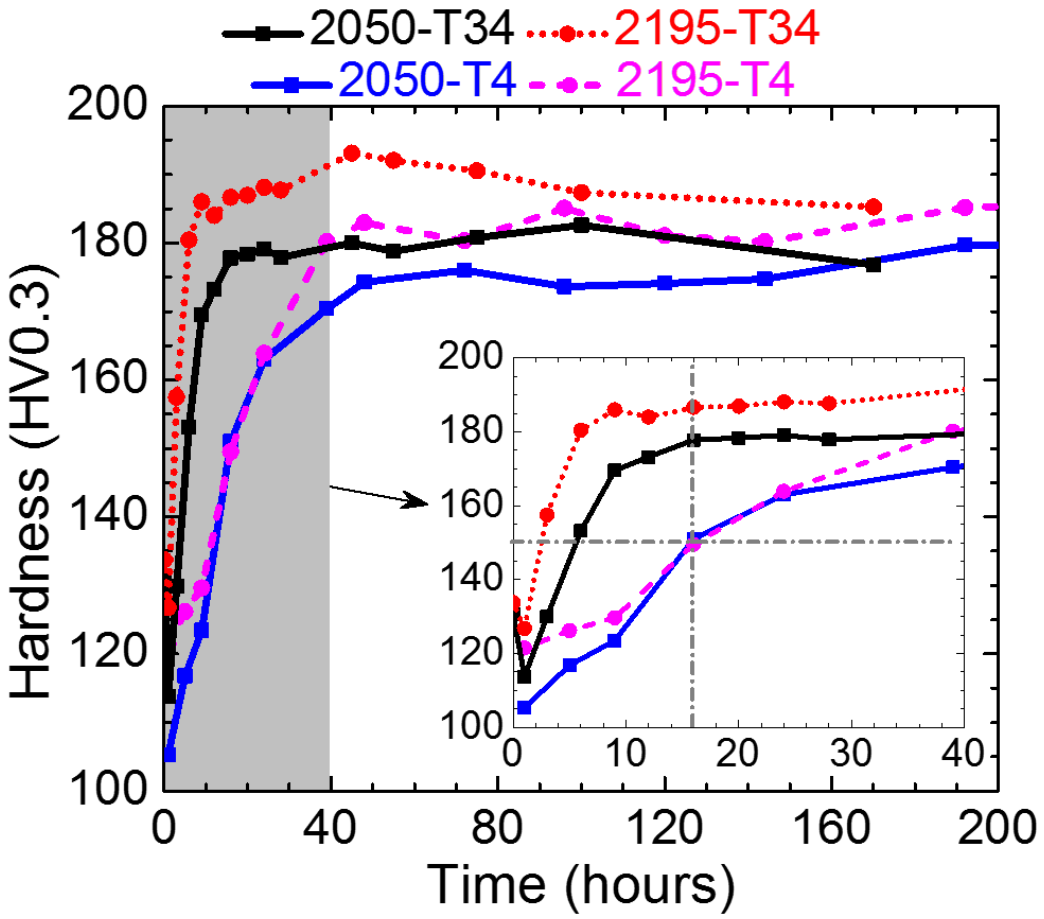

Figure 7.2 Hardness evolution in two third generation Al-Cu-Li alloys with intial microstructure as T3 and T4 temper. Note the effect of pre-deformation on aging kinetics in Al-Cu-Li alloys.

The difficulty of nucleating a precipitate is described with the coherency of its crystal

structure with the matrix structure. The mismatch between precipitate and matrix interface develops strain [9]. Incoherent and semi-coherent precipitates have high interfacial energy and thus have high energy barrier to nucleate [9]. Coherent precipitates nucleate easily and have low interfacial energy. For example, δ' (Al_3Li) is extremely coherent with matrix and forms during natural aging (low energy barrier) whereas T1 (Al_2CuLi) which is semi-coherent nucleates preferably on dislocations and sub-grain boundaries to reduce the lattice strain between precipitate and matrix. Interfacial energy of main strengthening precipitates in Al-Cu-Li and Al-Zn-Mg alloys are listed in Table 7.1. Coherent to semi-coherent η′ and semi-coherent η phase are the main phases observed in 7XXX alloys. As observed in case of FSW of 7050 alloy, aging at temperature lower than standard temperature (which is usually high) enhances the precipitation of η′ phase over η phase due to higher energy barrier for η phase. Similar FSW of 1424 alloy resulted in full recovery of strength due to dense precipitation of δ' (Al_3Li) which has extremely small nucleation barrier. T1 (Al_2CuLi) phase is semi-coherent and thus low temperature aging will be beneficial in case of FSW of Al-Cu-Li alloys as the energy barrier for nucleation at lower temperature will be even higher.

Table 7.1 Interfacial energy of key strengthening precipitates in Al-Cu-Li and Al-Zn-Mg alloys.

Precipitate	Alloy system	Coherency	Interfacial energy (mJ / m^2)
T1 (Al_2CuLi)	Al-Cu-Li (2XXX)	Semi-coherent	85-107 [10,11]
δ' (Al_3Li)	Al-Cu-Li (2XXX)	Coherent	10 [12]
η′ ($MgZn_2$)	Al-Zn-Mg (7XXX)	Coherent – Semi-coherent	60 [13]
η ($MgZn_2$)	Al-Zn-Mg (7XXX)	Semi-coherent	600-700 [13]

7.2 Future Directions

At the conclusion of this work, some future research paths are suggested to further enhance the weldability and performance of welded structures of complex precipitation strengthened aluminum alloys. A few suggestions are:

1. As observed in results of FSW of Al-Li and Al-Zn-Mg alloys, the heat input (peak temperature) requirement in FSW of both alloy system is different as the solution temperature is quite different. Hence, alloy system based design of FSW tool to improve the thermal management during FSW to enhance the final properties of the weldment.
2. Use of various auxiliary cooling methods such as, high conductivity backing plate, cooling behind the tool showed improved mechanical properties in the weld after PWHT. Thus, modeling based design of efficient auxiliary cooling methods can further push the envelope of properties achieved in FSW of precipitation strengthened aluminum alloys.
3. High speed welding results in low strength reduction in HAZ as seen in FSW of 7050 alloy, but tool wear, defect formation are the limiting factors in producing high speed FSW. A concentrated and intense heating source ahead of FSW tool can reduce the tool wear in high speed welds as the forces on tool will be less due to relatively soft material. Thus, FSW can be integrated with an intense laser source to heat and soften the material in front of the tool and hence process window of FSW can be expanded to produce even higher performance welds.
4. Alloys containing coherent and low interfacial energy precipitates resulted in higher strength recovery in HAZ and WN as compared to the case of alloy containing semi-coherent or incoherent precipitates. Therefore, development of alloys containing such precipitates can lead to HAZ-less friction stir weldable alloys.
5. In case of FSW of 7050 alloy, aging at a non-standard temperature resulted in high joint

efficiency of the weld. Thus, depending on the alloy system, single or multi-step aging treatments can be developed and employed specifically for welded joints to enhance the mechanical properties the weldment.

6. Low dislocation density was responsible for low strength recovery in welds of Al-Cu-Li alloys. Thus, introducing heterogeneous nucleation sites after FSW using methods such as laser peening and shot peening can be incorporated to enhance the nucleation density of semi-coherent precipitates.

References

[1] G.E. Totten, D.S. MacKenzie, Handbook of Aluminum: Vol. 1: Physical Metallurgy and Processes, CRC Press, 2003.

[2] W. Cassada, G. Shiflet, E. Starke, The effect of plastic deformation on Al2CuLi (T 1) precipitation, Metallurgical Transactions A. 22 (1991) 299-306.

[3] E. Starke, J. Staley, Application of modern aluminum alloys to aircraft, Prog. Aerospace Sci. 32 (1996) 131-172.

[4] A. Deschamps, F. Livet, Y. Brechet, Influence of predeformation on ageing in an Al–Zn–Mg alloy—I. Microstructure evolution and mechanical properties, Acta Materialia. 47 (1998) 281-292.

[5] R.S. Mishra, Z. Ma, Friction stir welding and processing, Materials Science and Engineering: R: Reports. 50 (2005) 1-78.

[6] R.S. Mishra, M.W. Mahoney, Friction Stir Welding and Processing, ASM International, 2007.

[7] R.S. Mishra, P.S. De, N. Kumar, Friction Stir Welding and Processing: Science and Engineering, Springer, 2014.

[8] J. Su, T. Nelson, R. Mishra, M. Mahoney, Microstructural investigation of friction stir

welded 7050-T651 aluminium, Acta materialia. 51 (2003) 713-729.

[9] R. Abbaschian, R. Reed-Hill, Physical Metallurgy Principles, Cengage Learning, 2008.

[10] T. Dorin, A. Deschamps, F. De Geuser, C. Sigli, Quantification and modelling of the microstructure/strength relationship by tailoring the morphological parameters of the T 1 phase in an Al–Cu–Li alloy, Acta Materialia. 75 (2014) 134-146.

[11] J. Nie, B. Muddle, Microstructural design of high-strength aluminum alloys, Journal of phase equilibria. 19 (1998) 543-551.

[12] A. Deschamps, C. Sigli, T. Mourey, F. De Geuser, W. Lefebvre, B. Davo, Experimental and modelling assessment of precipitation kinetics in an Al–Li–Mg alloy, Acta Materialia. 60 (2012) 1917-1928.

[13] N. Kamp, A. Sullivan, J. Robson, Modelling of friction stir welding of 7xxx aluminium alloys, Materials Science and Engineering: A. 466 (2007) 246-255.